Investigation of Nuclear Structure and Quasi-Discrete Features in ^{150,152}Sm via the (p,t) Reaction

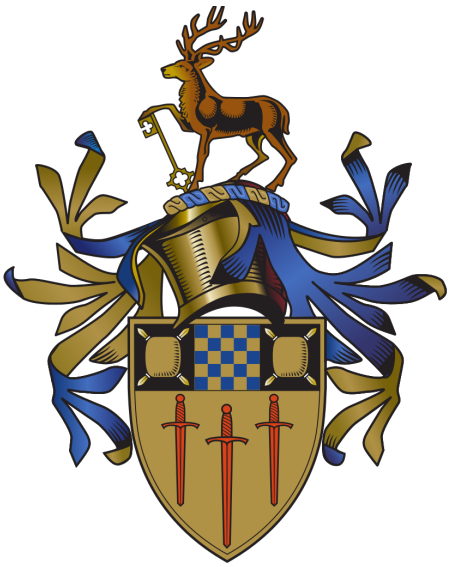

Peter James Charnall Humby

Submitted for the degree of Doctor of Philosophy

Department of Physics
Faculty of Engineering and Physical Sciences
University of Surrey

February 2017

Declaration of Originality

This thesis and the work to which it refers are the results of my own efforts. Any ideas, data, images or text resulting from the work of others (whether published or unpublished) are fully identified as such within the work and attributed to their originator in the text, bibliography or in footnotes. This thesis has not been submitted in whole or in part for any other academic degree or professional qualification. I agree that the University has the right to submit my work to the plagiarism detection service TurnitinUK for originality checks. Whether or not drafts have been so-assessed, the University reserves the right to require an electronic version of the final document (as submitted) for assessment as above.

Peter James Charnall Humby

Abstract

The (p,t) reaction was used to identify new levels and γ-ray transitions in ^{150,152}Sm utilising the particle-γ and particle-γ-γ coincidence techniques. The experiment was performed using the STARLiTeR array located at the Cyclotron Institute of Texas A&M University. The relative partial cross sections for the observed levels, angle averaged between 34 and 58 degrees, were measured. A narrow peak-like structure was observed between 2.3-3.0 MeV excitation energy, in between the region of strongly populated discrete states at low energy and the high energy continuum region. In ^{150}Sm, 39(4)% of the strength of the peak-like structure could be accounted for by the observed discrete states, which compares to a value of 93(15)% for ^{152}Sm. The orbital angular-momentum transfer was probed by comparison of the experimental angular distributions to those calculated using the DWBA theory. The experimental angular distributions for the population of the peak-like structures are very similar in the two reactions, and significantly different to both the angular distribution of the background under the structures, and to the distribution obtained from the nearby continuum region at higher excitation energy. Post irradiation, the half-lives of isomeric states in ^{152}Eu, populated in the ^{154}Sm(p,3n) reaction, were obtained by measuring the decrease in intensity of the γ rays emitted in the decay of these long lived levels. The half-life of the $J^{\pi} = 8^{-}$ isomer $^{152_{m2}}$Eu was measured to be 95.8(4) min, which is a factor of 2.5 reduction in uncertainty compared to the previous literature value of 96(1) min.

Acknowledgements

Firstly, I would like to thank Con and Paddy, my advisors. Paddy introduced me to nuclear physics research, for which I am very grateful. Con has been a fantastic advisor and provided tremendous amounts of advice and encouragement. I could not have been better supported and am extremely thankful. It was a pleasure to get to spend time at my writing retreat with Winston, Leo and Tiggi.

I have been very lucky to share my office with fantastic researchers during my time at Richmond. Anna, I greatly enjoyed working with you during my first year and appreciate the advice you have given me over the course of my PhD, especially during free pie Wednesdays at O'Charley's. Nathan, it was great to work with you again, thank you for making our trips to experiments and conferences so entertaining. I would also like to thank everybody in the Physics Department at the University of Richmond for making me feel so welcome.

I have been provided with the opportunity to travel to Hawaii, France, and many other places in-between, during my research and to meet some great people. Jason, Richard, Robert, Shuya, Mitch and everybody else at Livermore and Texas A&M, thank you for all of your help during my thesis experiments. This work would of course not have been possible without you.

Finally, I would like to thank my family and friends, for their ever-present support and guidance.

Contents

1 Introduction and Motivation **13**

1.1 Nuclear Structure in ^{150,152}Sm via two-neutron transfer reactions . . 14

1.2 Quasi-discrete features 15

2 Theory **17**

2.1 Nuclear Models 17

2.1.1 The Shell Model 17

2.1.2 Collectivity 19

2.1.3 The Nilsson Model 21

2.1.4 The Interacting Boson Model 22

2.2 Nuclear Reactions 23

2.2.1 Cross Sections 24

2.2.2 Direct and Compound Reactions 25

2.2.3 DWBA Theory 26

2.2.4 The (p,t) Reaction 30

2.2.5 γ-ray Transition Selection Rules 31

2.3 Detector Theory 32

2.3.1 Semiconductor Detectors 33

2.3.2 Interactions of Charged Particles with Matter 34
2.3.3 Interactions of γ Rays with Matter 36

3 Experimental Arrangement **40**

3.1 The STARLiTeR Array 40
3.2 STARS 41
3.2.1 STARS Energy Calibration 44
3.2.2 Particle Identification 45
3.2.3 Ray-trace 47
3.2.4 Off-Centred beam 49
3.3 LiTeR 49
3.3.1 LiTeR Energy Calibration 49
3.3.2 LiTeR Efficiency Calibration 51
3.3.3 Compton Suppression 53
3.4 Electronics 54
3.5 Particle-γ Coincidences 54

4 Results and Discussion **57**

4.1 Triton singles spectra and triton-γ matrices 57
4.2 Method for identifying discrete states 61
4.3 Individual Levels and γ-ray transitions 63
4.4 Levels and γ-ray transitions in ^{150}Sm 76
4.5 Levels and γ-ray transitions in ^{152}Sm 80
4.6 Angular Distributions 82
4.6.1 Discrete States 83
4.6.2 Peak-like Structures 84

4.7 Cross Sections 89
4.8 Peak-Like Structures 93
4.9 Isomeric Lifetimes in ^{152}Eu 102

5 Summary **108**

Appendices **111**

A Paper Published in Physical Review C: Improved measurement of the half-life of the $J^{\pi} = 8^{-}$ nuclear isomer $^{152_{m2}}$Eu **112**

B Paper Published in Physical Review C: Investigation of discrete states and quasi-discrete structures observed in ^{150}Sm and ^{152}Sm using the (p, t-γ) reaction **117**

C List of Publications **131**

List of Figures

2.1 The value of $R_{(\frac{4}{2})}$ plotted against neutron number for the samarium isotopes. 21

2.2 Nilsson diagram showing the region around N=82 22

2.3 Compton-scattered γ-ray energy as a function of scattering angle for initial γ-ray energies of 200 keV, 500 keV and 2000 keV 37

2.4 A polar plot of the cross section for Compton scattering for incident photon energies of 10 keV, 200 keV and 5000 keV. 38

3.1 A schematic diagram of the STARLiTeR array. 42

3.2 Photograph of the aluminium chamber containing the target wheel and STARS in the ΔE-E1-E2 configuration. 43

3.3 Energy spectrum of α-particles emitted from a ^{226}Ra source, measured using the ΔE detector. 45

3.4 ^{12}C(p,p') excitation energy spectrum produced using a natural carbon target. 46

3.5 Particle identification plot produced using the STARS telescope. . . 47

3.6 Ray-trace diagram from the STARS telescope. 48

3.7 The distribution of counts in the ΔE detector rings and sectors. . . 50

3.8 γ-ray energy spectrum produced using a ^{60}Co source. 51
3.9 The absolute photopeak efficiency of the LiTeR array plotted as a function of γ-ray energy. 52
3.10 Plot of the clover-BGO time differences, showing the events rejected as Compton scattering events. 53
3.11 Schematic diagram of the STARLiTeR electronics. 54
3.12 A plot of the time differences between the particle and γ-ray events, where the particle-γ coincidence gate is indicated. 55
3.13 A triton-γ coincidence matrix from the ^{152}Sm(p,t) reaction. 56

4.1 The triton singles spectra from the (a) ^{152}Sm(p,t) and (b) ^{154}Sm(p,t) reactions. The discrete states at low excitation energy and the high energy continuum region can be seen. The PLS is indicated by an asterisk. 59
4.2 Triton projections of the (t-γ) matrices from the ^{152,154}Sm(p,t) and ^{154,156,158}Gd(p,t) reactions. 60
4.3 Triton energy spectrum in coincidence with the 2702.9(13) keV transition from the level at 3037.8(9) keV in ^{150}Sm. 63
4.4 A plot of excitation energy against spin for levels directly populated in ^{150}Sm 65
4.5 A plot of excitation energy against spin for levels directly populated in ^{152}Sm 66
4.6 Triton energy spectra in coincidence with the 1290.9(3) and 2028.9(3) keV transitions from the level at 2362.6(2) keV in ^{150}Sm. 79

4.7 The experimental angular distributions for the levels in ^{150}Sm at (a) 334 keV, $J = 2$ (b) 740 keV, $J = 0$ (c) 1256 keV, $J = 0$ and (d) 1417 keV, $J = 2$ are compared to the DWBA calculations for the respective L transfer. 84
4.8 The experimental angular distribution for the level at 2320.5(2) keV is compared to the DWBA calculations for $L = 4$ and $L = 5$ transfer. 85
4.9 Triton singles spectrum from the ^{152}Sm(p,t) reaction where the area used to calculate the angular distribution of the PLS is shaded in blue. 87
4.10 The angular distributions of the PLS, the background under the PLS and the nearby continuum regions are compared for ^{150}Sm and ^{152}Sm. Calculated curves corresponding to $L = 2, 3$ and 4 transfer are also plotted. 88
4.11 The relative partial cross sections from the ^{152}Sm(p,t) reaction are compared to the triton projection of the triton-γ matrix. 90
4.12 The relative partial cross sections from the ^{154}Sm(p,t) reaction are compared to the triton projection of the triton-γ matrix. 92
4.13 The excitation energy of the PLS as a function of neutron number for the Sm and Gd isotopes. 93
4.14 Partial level scheme of ^{150}Sm showing levels directly populated in the region of the PLS indicated by the dashed lines. New levels and γ rays are plotted in red. 98
4.15 Same as Figure 4.14 but for ^{152}Sm. 99
4.16 Triton energy spectra from the ^{148,150,152,154}Sm(p,t) reactions. 100

4.17 The excitation energy of high-energy and low-energy bumps as a function of mass number. 101
4.18 Partial decay scheme of the long lived (>1 hour) isomeric states of ^{152}Eu. 103
4.19 The low energy region of the γ-ray energy spectrum obtained during the activation measurement and the γ-time matrix. 104
4.20 A plot of the intensity of the 90 keV γ ray from the decay of $^{152_{m2}}$Eu against time. 106
4.21 Measurements of the half-life of $^{152\mathrm{m1}}$Eu obtained by measuring the decrease in intensity of the 122, 334, 842 and 963 keV γ rays are compared to the previous measurements. 107

List of Tables

2.1 Optical model parameters used in the DWBA calculations 29

4.1 Levels and γ-ray transitions observed in ^{150}Sm 67

4.2 Levels and γ-ray transitions observed in ^{152}Sm 71

4.3 Comparison of the relative partial cross sections for discrete states in ^{150}Sm to those from the literature. 91

Chapter 1

Introduction and Motivation

From the discoveries of radioactivity by Becquerel in 1896 [1] and the atomic nucleus from the alpha-particle scattering experiments of Rutherford in 1906 [2], the field of nuclear physics emerged. Atomic nuclei consist of Z positively charged protons and N electrically neutral neutrons and exist on the scale of 10^{-15} m. The characteristic energies of nuclear physics vary from keV to MeV, placing the field in between atomic physics and particle physics in terms of both the length scales and energies involved. Nuclei exist on the quantum scale and so a typical nucleus with a few tens of protons and neutrons presents an extremely complicated quantum many-body problem. For this reason, much of our insight comes from simplified models of the nucleus and from observing systematic changes in the properties of nuclei with varying proton and neutron number.

The samarium (Z=62) nuclei lie in a region of rapid nuclear shape change from spherical to deformed with increasing neutron number [3]. This N=90 region has been the focus of intense theoretical and experimental study, see for example [4–9]. The region provides a challenging testing ground for models that attempt to

describe transitional and deformed nuclei. In the present work, the nuclei ^{150,152}Sm are investigated using the (p,t) reaction and the particle-γ coincidence technique, the motivation for which is outlined in the following sections.

1.1 Nuclear Structure in ^{150,152}Sm via two-neutron transfer reactions

In the early two-neutron transfer experiments by Maxwell *et al.* [10] and Bjerregaard *et al.* [11], large cross sections for the direct population of excited $J^\pi = 0^+$ states relative to the ground state were observed in the ^{150}Sm(t,p) and ^{152}Sm(p,t) reactions. This was interpreted in the same papers in terms of shape coexistence, inviting further interest in the region. Two-neutron transfer reactions, such as the (p,t) reaction, are able to probe states at low excitation energy formed from the removal of pairs of correlated valence neutrons, as well as levels at higher excitation energy formed by the removal of one or both neutrons from deep below the Fermi surface. In the nearby Gd (Z=64) nuclei the (p,d) reaction has been employed [12] in order to investigate low-spin states produced via the transfer of neutrons from both near the Fermi surface, and from deeper lying orbitals below the proposed N=64 gap [13–16].

Following the works of Maxwell and Bjerregarrd further Sm(p,t) experiments were performed [17–26], greatly increasing the amount of experimental data available for these nuclei. However, no γ rays were measured in coincidence with the tritons in these studies, making level assignments above approximately 2 MeV very difficult due to the rapidly increasing level density. In the present work, ^{150,152}Sm

are studied for the first time using triton-γ coincidences. The spin and parity of a level directly populated in the (p,t) reaction may be determined by comparison of the experimental angular distributions of the outgoing tritons to calculated distributions. In the study of the ^{156}Gd(p,t) reaction by Riezebos *et al.* [27] this method was used to measure integrated spectroscopic factors as a function of excitation energy for the population of J=0^+, 2^+, 4^+ and 6^+ levels. It can be seen in Figure 3 of that paper that there is a rapid increase in 2^+, 4^+ and 6^+ strength above approximately 2.2 MeV in excitation energy. However, there is an interesting lack of monopole strength at high excitation energy; the vast majority of the L=0 transfer strength is to the ground state. This lack of strength is difficult to explain [27], and provides motivation to probe the L-transfer distributions at this excitation energy in nearby nuclei, such as in the present work.

1.2 Quasi-discrete features

In 1981 Struble *et al.* [21] observed a large, broad enhancement of two neutron transfer strength in the ^{148,150,152,154}Sm(p,t) reactions. A narrower structure at lower excitation energy was also observed in the ^{152,154}Sm(p,t) reactions. In the recent studies by T. J. Ross *et al.* [28] and J. M. Allmond *et al.* [29] a similar narrow structure was observed in the ^{154,156,158}Gd(p,t) reactions between 2.2-3.2 MeV excitation energy. The structure occurs at an intermediate excitation energy, in between the region dominated by few, strongly populated discrete states at low excitation energy and the continuum 'background' at high excitation energy. Similar structures have been observed in the tin isotopes between 7-9 MeV excitation energy by Crawley *et al.* [30] in the ^{112,116,118,120,122,124}Sn(p,t) reactions. It was shown

by Nomura [31] that the energy systematics of these structures in the Sn isotopes are well described by a *valence-deep* excitation, i.e. the transfer of one neutron from near the Fermi surface and the other from a deep lying orbital below the major shell closure. A study of the (p,t) reaction across a wide range of nuclei from ^{66}Zn to ^{230}Th by Nakagawa *et al.* [32] showed that these structures corresponding to valence-deep excitations have been observed across a wide range of the nuclear chart. In many of these nuclei, including ^{148}Sm, a similar bump was seen at higher excitation energy and corresponds to the deep-deep excitation; i.e. transferring both neutrons from below the major shell closure. The triton-γ coincident technique employed in the present work is an excellent tool with which to study the narrow structure as it allows both the identification of discrete states in this region of high level density, and for the angular momentum transfer distributions to be probed.

Chapter 2

Theory

2.1 Nuclear Models

In this section the characteristics of some commonly encountered models of the nucleus relevant to the present work are described.

2.1.1 The Shell Model

A large amount of experimental evidence supports the existence of nuclear shell closures at magic numbers of 2, 8, 28, 50, 82 and 126 [33, 34]. For example, the deviation of proton and neutron separation energies from the predictions of the semi-empirical mass formula show a smooth increase with nucleon number except at the magic numbers, where sharp jumps occur. The shell model considers the individual nucleons to be moving independently in a central potential produced by the interaction with all the other nucleons. One might consider, for example, an infinite square potential well as a simple choice. However, this potential would require an infinite amount of energy to remove a particle from the well and a sharp

edge in the potential, both of which are not physical. In addition, it does not correctly reproduce the observed magic numbers. Another possible choice is the simple harmonic oscillator potential. However, this also produces incorrect magic numbers of 2, 8, 20, 40, 70, 112 and 168. A better, choice is the Woods-Saxon potential, given by

$$V(r) = \frac{-V_0}{1 + e^{(r-R)/a}} \tag{2.1}$$

where V_o is the depth of the potential well, R is the radius of the well and a describes the sharpness of the edge of the well. This potential is a more physical choice in that it does not require an infinite amount of energy to remove a nucleon and better represents the diffuse nature of the nuclear surface observed in electron scattering experiments. When combined with a spin-orbit correction, the Woods-Saxon potential reproduces the experimentally observed shell closures.

A key assumption of the shell model is that the nucleons are moving independently in the potential well. This is possible as although the density of the nucleus is high, many of the collisions are forbidden due to the Pauli principle.

The spin and parity of the ground state of an odd-A nucleus can be predicted by the shell model by considering only the valence nucleons. If only the single unpaired nucleon is considered, in the extreme independent-particle model, the spin and parity of the ground state is then determined by the orbital that the unpaired nucleon lies in. In even-even nuclei, where all the nucleons are paired, it is then clear that the ground state must be a 0^+ state. The shell model is particularly successful for stable and near-stable nuclei in the regions A<150 and 190<A<220 where it correctly predicts nearly all of the odd-A ground state spins and parities [34].

2.1.2 Collectivity

Vibrational Behaviour

As well as considering nuclear states in terms of individual orbitals, we may also consider the collective motion of the nucleus as a whole. Firstly, we may consider that the nucleus can vibrate about an equilibrium position by adding vibrational phonons to the system. A dipole (L=1) phonon would correspond to an oscillation in the centre of mass of the system, and therefore cannot result from the internal nuclear forces. If we were to add the next highest angular momentum phonon, a quadrupole (L=2) phonon , to the 0^+ ground state of an even-even nucleus it would result in a single excited 2^+ state. Indeed, a 2^+ state is observed as the first excited state in nearly all even-even nuclei, although not all of these states are vibrational in nature. Adding a second quadrupole phonon to the system would produced a triplet of states $(0^+, 2^+, 4^+)$ at twice the energy of the first excited 2^+ state. Therefore, in a vibrational nucleus we expect the ratio of the energies of the first excited 4^+ and 2^+ states, $R_{(\frac{4}{2})}$, to be equal to 2.

Deformation and Rotational Behaviour

In a non-spherical nucleus we may also consider rotational behaviour. We first define a deformation parameter for an ellipsoidal nucleus,

$$\beta = \frac{4}{3}\sqrt{\frac{\pi}{5}}\frac{\Delta R}{R_{av}}, \tag{2.2}$$

where ΔR is the difference in length between the semiminor and semimajor axis, and R_{av} is the average radius. $\beta > 0$ corresponds to a prolate (cigar shaped)

nucleus whereas $\beta < 0$ corresponds to an oblate (pancake shaped) nucleus. The intrinsic quadrupole moment of the nucleus, Q_0, is related to the deformation by

$$Q_0 = \frac{3}{\sqrt{5\pi}} R_{av}^2 Z\beta \left(1 + 0.16\beta\right) \tag{2.3}$$

By measuring the quadrupole moment a value of β may therefore be obtained, after correcting for the rotation of the nucleus in the laboratory frame of reference. For deformed nuclei in the region $150 < A < 190$, which includes the nuclei of interest in the present work, β is found to have values around 0.29 [34]. The rotational kinetic energy of a rigid rotor is given by

$$E_{rot} = \frac{\hbar^2}{2\mathcal{I}} \cdot I\left(I + 1\right) \tag{2.4}$$

where $\mathcal{I}$ is the moment of inertia and I is the total angular momentum of the nucleus. Using this equation the value of $R_{(\frac{4}{2})}$ is found to be $3.3\dot{3}$. Many nuclei in the $150 < A < 190$ region are found to have $R_{(\frac{4}{2})}$ close to this value. For example, for ^{154}Sm, $R_{(\frac{4}{2})} = 3.25$.

In Figure 2.1 $R_{(\frac{4}{2})}$ is plotted against neutron number for the even samarium isotopes, both stable and unstable, between N=70 and N=98. It can be seen from this figure that the effect of the N=82 shell closure is dramatic. A rapid rise in the value of $R_{(\frac{4}{2})}$ occurs between ^{150}Sm and ^{152}Sm, the nuclei populated in the present work in the (p,t) reaction.

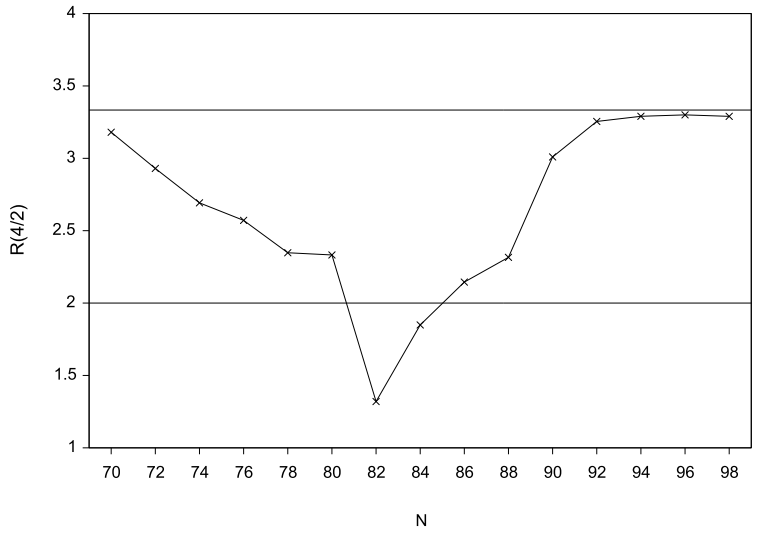

Figure 2.1: The ratio of the energy of the first excited 4^+ and 2^+ states, $R_{(\frac{4}{2})}$, plotted against neutron number for the samarium isotopes. The values for a spherical vibrator (2) and a rigid rotor ($3.3\dot{3}$) are indicated by the horizontal lines. Data is from the NNDC database [35].

2.1.3 The Nilsson Model

In order to accurately predict the spin, parity and energies of excited states, the shell model must be modified to take account of nuclear deformation. When the Schrödinger equation is solved with a non-spherical potential, the quantum numbers l and j, which can be used to label states in the spherical case, are no longer good quantum numbers. Now we must consider Ω, the value of j projected on the symmetry axis of the nucleus. For prolate deformation, orbits with a small value of Ω are, on average, closer to the bulk of the nuclear matter than orbits with a large value of Ω. Therefore, they are lowered in energy and the degeneracy in j is broken. Each orbital may now contain two nucleons, corresponding to $\pm\Omega$. Plotting the energy of these Nilsson orbitals as a function of deformation results in a plot known as the Nilsson diagram.

Nilsson orbitals are labelled using the notation $K[Nn_z\Lambda]$, where K is the projection of the total angular momentum onto the symmetry axis, N is the principal quantum number, n_z is the number of radial nodes in the z-direction and Λ is the component of orbital angular momentum along the z-axis. A Nilsson diagram for the N=82 region, from Reference [36], is shown in Figure 2.2.

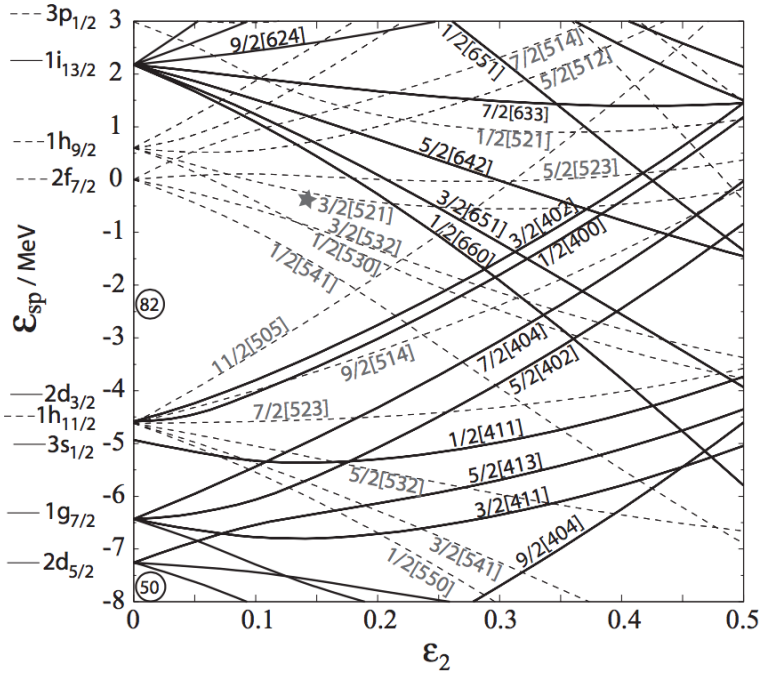

Figure 2.2: Nilsson diagram showing the region around N=82, from Reference [36].

2.1.4 The Interacting Boson Model

The Interacting Boson Model (IBM) [37] is based on mathematical groups and algebras. The IBA is particularly useful for the case of nuclei which are far from shell closures as for these nuclei microscopic shell-model calculations become difficult due to the very large number of degrees of freedom.

In the IBA, the valence nucleons are pairwise coupled to form bosons of spin 0

and $2\hbar$ (s and d bosons). Bosons of other angular momenta can also be included. The number of bosons for a given nucleus is fixed and in the IBA-1, where the proton and neutron bosons are treated equally [38], is equal to half the sum of the number of valence protons and neutrons. In the IBA it is useful to consider nuclei in terms of the symmetry groups which describe their properties; for example spherical, vibrational nuclei are described by the group U(5). The two other particularly interesting symmetry groups in the context of nuclei are SU(3) and O(6) which correspond to axially symmetric rotors and γ-soft rotors respectively, where the term γ-soft describes nuclei that may undergo vibrations perpendicular to the axis of symmetry.

2.2 Nuclear Reactions

In this section, some properties and classifications of nuclear reactions are outlined.

For the reaction $A + B \rightarrow C + D$ the notation $A(B, C)D$ is used, where A is the target nucleus, B is the beam particle, C is the outgoing particle and D is the residual nucleus. A, B, C and D may be either nuclei, nucleons, γ rays or other particles. The Q-value of a reaction indicates whether a reaction is energetically favourable or not and is given by

$$Q = (M_{init} - M_{fin})\, c^2 \tag{2.5}$$

where M_{init} and M_{fin} are the initial and final masses of the entire system respectively. During the reaction, the total energy and linear momentum of the system are conserved. If the energy of the incoming beam particle, the energy of the

outgoing particle and the reaction Q-value are known the excitation energy of the residual nucleus can be determined. From conservation of energy and linear momentum, it is clear that for $Q < 0$ there is an energy threshold below which the reaction cannot take place. For $Q > 0$ there is no energy threshold. However, if A and B are charged particles then the Coulomb barrier, V_c, must be overcome to initiate the reaction. The value of V_c, in the centre of mass frame, can be estimated using [39]

$$V_c = 1.44 \frac{Z_1 Z_2}{R_0 \left(A_1^{1/3} + A_2^{1/3} \right) (\text{fm})} (\text{MeV}) \tag{2.6}$$

where $A_{1,2}$ and $Z_{1,2}$ are the mass numbers and charge numbers of the two colliding particles respectively and $R_0 = 1.25$ fm. For the case of protons incident upon a ^{152}Sm target, the value of V_c is approximately 13.4 MeV.

2.2.1 Cross Sections

The probability of a specific nuclear reaction occurring is given by the cross-section for that reaction, σ, which is defined as

$$\sigma = \frac{I_b}{I_a N} \tag{2.7}$$

where I_a is the number of incoming beam particles per unit time, I_b is the number of reactions per unit time and N is the number of nuclei per unit area in the target. Therefore, σ has the dimension of an area and the commonly used unit is the barn (b), where 1b = 100 fm^2. Since a detector will be positioned at a certain θ and ϕ, the azimuthal and polar angles, with respect to the incident beam and will cover a finite solid angle, the differential cross-section is sometimes a more useful quantity.

This is defined as

$$\frac{d\sigma}{d\Omega} = \frac{\omega(\theta, \phi)}{4\pi I_a N} \tag{2.8}$$

where $\omega(\theta, \phi)$ is the angular distribution of the outgoing particles. The total cross section σ can be obtained from the differential cross section by integrating over all possible θ and ϕ.

2.2.2 Direct and Compound Reactions

Direct reactions are fast, peripheral reactions that involve only a few nucleons and that occur on a time scale comparable to, within an order or magnitude, the time taken for the projectile to pass by the target [39]. They proceed via a single-step process that may change only a single degree of freedom in the nucleus [40]. This degree of freedom can be a single unpaired nucleon in an odd-even nucleus. Since only a single degree of freedom can be changed, direct reactions tend to populate states that are similar to the ground state of the target nucleus. The cross sections are strongly dependent on the overlap of the wave functions of the initial and final states. The angular distribution of the outgoing particle is often strongly forward peaked and a function of the orbital angular momentum transfer.

In compound nuclear reactions, the incident beam particle interacts with a relatively large number of nucleons, distributing its energy throughout the target nucleus. This allows the population of states that have significantly different configurations compared with that of the ground state. The compound nucleus has a relatively long lifetime, compared to the time scale of direct reactions, as one of the nucleons must randomly gain enough energy to be ejected in order for the decay to proceed. Due to the randomness of the energy distribution in the com-

pound nucleus, i.e. the non-selectiveness of the final state, this type of reaction is more likely to populate levels at higher excitation energy due to the higher level density in this region. The angular distributions of the outgoing particles in compound reactions are broadly peaked, as opposed to the strongly forward-peaked distributions characteristic of direct reactions.

Due to the randomness of the population of final states, the decay of a compound nucleus can be assumed to be independent of the method of formation. This is known as Bohr's compound nucleus hypothesis and is an important assumption in the surrogate reaction technique [41–43]. In this technique, a reaction is chosen in order to produce the same compound nucleus as in a more difficult to perform reaction, for example, reactions that would require a short-lived radioactive target. The technique can be used to measure (n, γ) cross sections by measuring the γ-ray decays of a compound nucleus produced via a different reaction. For example, in the N=90 region, Scielzo *et al.* [44] compare ^{155,157}Gd(n, γ) cross sections evaluated using the surrogate reaction method to the directly measured cross sections.

2.2.3 DWBA Theory

The optical model, named for its similarity to the calculations for the scattering of light from a semi-transparent sphere, is an extremely useful and well-established model for calculating certain elastic-scattering observables such as the angular distributions of the outgoing particles. In this model, potentials are chosen to describe the state of the system before and after a collision. In the simplest approximation, incident plane waves are chosen. The Schrödinger equation is then solved for the chosen potentials, and the angular distribution of the outgoing

particles can be extracted.

For inelastic scattering, the potential must consist of real, $V(r)$, and imaginary, $W(r)$, components. The real component describes the elastic-scattering channel, whereas the imaginary components describe the inelastic scattering. A common choice for the real component, as in the shell model, is

$$V(r) = \frac{-V_0}{1 + e^{(r-R)/a}}, \tag{2.9}$$

where the parameters V_0, R and a are fitted to elastic scattering data. In practice, these parameters are chosen from sets that have been evaluated over large ranges of the nuclear chart, such as those found in References [45, 46]. When considering direct reactions, which are peripheral reactions involving only a few nucleons, $W(r)$ is often chosen so that it is large only near the surface. A spin-orbit component of the potential, V_{SO}, is usually added which is also large only near the surface.

In the simple plane-wave calculations, an assumption is that transfer can only occur for $r > R$, and the actual radial distribution of the transferred particle is not considered. The distorted wave Born approximation (DWBA) addresses these issues and considers the incoming and outgoing waves to be distorted plane waves. However, the DWBA theory still assumes that the reaction proceeds via a one-step process, and the calculations are valid only when elastic scattering is the dominant exit channel.

In the present work, the computer program DWUCK4 [47] was used to perform DWBA calculations for the ^{152,154}Sm(p,t) reactions. The optical model parameters used are listed in Table 2.1. The proton parameters were obtained from reference [48]. The triton and neutron parameters are from reference [49]. The notation

follows that of reference [48], where the potential is given by

$$U(r) = V_c(r) - V_r(r) f(x_r) + \left(\frac{\hbar}{m_\pi c}\right)^2 V_{SO}(s\cdot l)\frac{1}{r}\frac{d}{dr} f(x_{so}) - iW_o f(x_{iv}) + iW'\frac{d}{dr_{is}} f(x_{is}) \tag{2.10}$$

where

$$f(x_n) = 1/(1 + e^{x_n}) \tag{2.11}$$

and

$$x_n = (r - r_n A^{1/3})/a_n \tag{2.12}$$

The parameters R_r, R_{is}, R_{iv} and R_{so} are related to the reduced radius of the real potential, imaginary surface potential, imaginary volume potential and spin orbit potential, respectively. a_r, a_{is}, a_{iv} and a_{so} are the corresponding diffuseness parameters, and nlc is the nonlocality parameter.

For the (p,t) reaction, the angular distribution of the outgoing tritons is characteristic of the L transfer. Additionally, for reactions on an even-even nucleus $L = J$, and so by comparing the experimental distributions to calculated curves, the spin of a level may be determined.

Table 2.1: The optical model parameters used in the DWBA calculations. The proton parameters were taken from Reference [48]. The triton and neutron parameters are from Reference [49]. *nlc* is the nonlocality parameter.

	V_r (MeV)	W' (MeV)	W_0 (MeV)	V_{so} (MeV)	R_r (fm)	R_{is} (fm)	R_{iv} (fm)	R_{so} (fm)	a_r (fm)	a_{is} (fm)	a_{iv} (fm)	a_{so} (fm)	R_c (fm)	*nlc*
p	57.5	29.6	3	5.65	1.200	1.150	1.259	1.010	0.670	0.779	0.76	0.75	1.25	0.85
t	160.03		17.83		1.200		1.400		0.720		0.84		1.30	0.25
n				λ=25	1.17				0.75					

2.2.4 The (p,t) Reaction

In the (p,t) reaction, two neutrons are transferred from the target nucleus to the incident proton. At the 25-MeV beam energy used in the present work, the process is a direct reaction. A useful feature of this reaction with an even-even target is that $L = J$. Therefore, as stated in the previous section, the spin of a level may be determined by comparing experimental angular distributions to calculated DWBA curves. Cross sections from the (p,t) reaction can provide information about the correlation (spatial and momentum) of the neutron pairs in the ground state of the target nucleus [50]. In the following section, the selection rules of the (p,t) reaction, discussed in detail in reference [50], are outlined.

Selection Rules of the (p,t) Reaction

In the (p,t) reaction, an exact selection rule exists such that

$$|J_i - J_f| \leq J \leq (J_i + J_f) \tag{2.13}$$

where J_i and J_f are the initial and final total nuclear angular momentum, and the pair of transferred neutrons is coupled to angular momentum J. Additionally,

$$\Delta\pi = (-1)^{l_1+l_2} = (-1)^{\Lambda+\lambda} \tag{2.14}$$

where l_1 and l_2 are the individual orbital angular momentum of the transferred neutrons in the target nucleus, Λ is the angular momentum of the centre of mass of the transferred pair and λ is the relative angular momentum of the pair. If the pair of transferred neutrons is coupled to $S = 0$ in the triton, where S is the total

spin angular momentum of the pair, then $L = J$. For the case of $\lambda = 0$,

$$\Delta\pi = (-1)^L = (-1)^J \tag{2.15}$$

i.e, only states of natural parity may be populated.

Since the isospin of the transferred neutron pair is 1, it follows that

$$|T_i - T_f| \leq 1 \leq (T_i + T_f) \tag{2.16}$$

where T_i and T_f are the initial and final total isospins of the nucleus.

2.2.5 γ-ray Transition Selection Rules

Excited nuclear states may decay to a lower lying level via the emission of a high energy photon in the process known as γ decay. A level may decay either directly to the ground state of the nucleus, or via intermediate states resulting in a cascade of γ rays. Measuring the γ ray energies allows us to determine the energies of the excited states, with a typical accuracy of approximately 0.2 keV when measured with a high purity germanium (HPGe) detector. The γ-ray intensities, angular distributions and correlations also provide valuable information about the nature of the levels.

This decay process must follow certain transition rules. Since angular momentum must be conserved, it follows that

$$\mathbf{I_i} = \mathbf{L} + \mathbf{I_f} \tag{2.17}$$

where I_i and I_f are the initial and final nuclear angular momentum, and L is the angular momentum carried away by the outgoing photon. Since these are vector quantities, the allowed values of L are

$$|I_i - I_f| \leq L \leq (I_i + I_f) \tag{2.18}$$

where L is an integer. A γ-ray transition may be labelled as either electric, E, or magnetic, M, followed by the number of units of angular momentum. For example, the label $E2$ refers to an electric quadrupole transition, that carries two units of angular momentum. The change in parity, or lack thereof, between the excited states determines whether even-L or odd-L electric or magnetic transitions are allowed. If there is no change in parity then L must be even for electric transitions and odd for magnetic transitions. If there is a change in parity, then L must be odd for electric transitions and even for magnetic transitions. For example, for a transition between an excited 4^+ state and a 2^+ state, the allowed transitions are $E2$, $M3$, $E4$, $M5$ and $E6$. However, the lower multipole transitions have much higher transition rates and dominate the decay process. Additionally, an electric transition is more probable than a magnetic transition of the same L.

2.3 Detector Theory

In the present work, HPGe clover detectors and Si detectors are utilised in order to detect γ rays and light charged particles respectively. Here, some principles behind both charged particle and γ-ray detection are outlined.

2.3.1 Semiconductor Detectors

Semiconductor detectors are based on electron-hole collection and provide excellent energy resolution due to the very large number of charge carriers generated in an event [51]. The Si detectors in the ΔE-E telescope and the HPGe detectors used in the present work are semiconductor detectors.

In semiconductors, a band gap exists between a valence band and a conduction band. The energy of this gap, E_g, is typically of the order of 1 eV. At a temperature of 300 K, E_g=0.665 eV for Ge and E_g=1.115 eV for Si [51]. The higher band gap for Si allows this material to be used in room temperature detectors. An electron has a probability of crossing the band gap and forming an electron-hole pair given by

$$p = CT^{3/2} exp\left(-\frac{E_g}{2kT}\right) \tag{2.19}$$

where T is the absolute temperature, k is the Boltzmann constant, and C is a constant dependent on the semiconductor material. If an external electric field is applied, the electrons in the conduction band and holes in the valence band will move, in opposite directions, at different drift velocities, v_d. If the strength of the electric field is increased then v_d will increase until a saturation velocity is reached. In room temperature Si, the saturation for electrons occurs at approximately $2 \cdot 10^4$ V cm^{-1} and results in an electron drift velocity of approximately 10^7 cm s^{-1} [51]. In Ge cooled to a temperature of 80 K, the saturation occurs at a field strength of approximately $2 \cdot 10^3$ V cm^{-1} and v_d is approximately 10^7 cm s^{-1}.

An intrinsic semiconductor can be doped with impurities to form n-type and p-type semiconductors. In an n-type semiconductor, the impurity results in donor levels near the top the band gap. These levels lie very close to the conduction

band and so the electrons are easily excited, resulting in more electrons in the conduction band than holes in the valence band. In a p-type semiconductor the impurity creates acceptor levels near the bottom of the band gap, which results in holes in the valence band.

When n-type and p-type semiconductor material are placed in contact with each other diffusion of the free electrons and holes will occur. This diffusion creates immobile positive charge in the n-type region and immobile negative charge in the p-type region, creating an electric field which inhibits further migration and a depletion region is formed. The size of the depletion region can be increased by applying a negative voltage to the p-type material and a positive votage to the n-type material; this is known as reverse-biasing. Within the depletion region, charge carriers can be easily collected and this region is known as the 'active volume' of the detector. A large active volume is desirable since it allows for the detection of radiation that may penetrate deep in to the material. The size of the depletion region may be increased by lowering the concentration of impurities, such as in the high-purity germanium detectors (HPGe) used in the present work.

2.3.2 Interactions of Charged Particles with Matter

Charged particles interact with detector material via the Coulomb interaction. The key interactions are those that occur between the incident particle and the negatively-charged atomic electrons in the detector material. Interactions with the positively-charged nuclei of the detector material are also possible but have negligible effect on the response of the detector [51]. Due to conservation of energy and momentum, only a small amount of energy can be imparted to an electron in

a single collision. Therefore, many interactions between the incident particle and the electrons occur before the full energy of the particle is deposited in the detector material. Each interaction may either cause an electron to be excited to a higher lying shell or, if the transferred energy is large enough, removed from the parent atom in the process known as ionisation. The ionised electrons can then be swept out of the material in the form of an electronic pulse by applying a voltage across the detector. The amplitude, shape and timing of this pulse provides information about the energy and type of particle that entered the detector.

An important quantity to consider is the range of a particle in the detector material. In the present work, a silicon ΔE-E telescope is used and the particles of interest must be able to pass through the ΔE detector and then fully stop in the E detector. If the particle cannot pass through the ΔE detector then the trigger condition for the data acquisition will not be met. The rate of energy loss of a charged particle in matter is given by the Bethe formula [51]

$$-\frac{dE}{dx} = \frac{4\pi e^4 z^2}{m_e v^2} NZ \left[\ln \frac{2m_e v^2}{I} - \ln\left(1 - \frac{v^2}{c^2}\right) - \frac{v^2}{c^2} \right], \tag{2.20}$$

where v is the velocity of the particle, z is the charge number and m_e is the electron rest mass. I, N and Z are the ionization potential, number density and atomic number of the detector material respectively. From this equation, it can be seen that incident particles with a greater charge will lose their energy at a greater rate, and that the rate of energy loss increases for slower particles (i.e particles that have less kinetic energy). It must be noted however that Equation 2.20 breaks down at low energies where the particle may gain electrons from the detector material and therefore decrease it's net charge.

2.3.3 Interactions of γ Rays with Matter

A γ ray may interact with detector material via one of several competing processes: mainly photo-electric absorption, Compton scattering or pair production. For low-energy γ rays, less than approximately 200 keV in germanium [34], photoelectric absorption is most likely to occur. In this process, an atom in the detector material absorbs the γ ray and subsequently ejects an electron. The probability of this process occurring is approximately proportional to Z^4 [34], where Z is the atomic number of the absorbing material. Therefore, it is desirable that the detector material has a large Z in order to increase the detection efficiency. The probability for photo-electric absorption decreases as a function of γ-ray energy except for sharp enhancements where the ionisation of electrons in the next shell becomes available.

At intermediate γ-ray energies, between approximately 200 keV and 8 MeV in germanium, Compton scattering is dominant. In this process, an incident γ ray scatters from an atomic electron, transferring some of its energy and momentum. The energy of the scattered photon as a function of scattering angle is given by

$$E'_\gamma = \frac{E_\gamma}{1 + (E_\gamma/mc^2)(1 - \cos\theta)} \tag{2.21}$$

and is plotted in Figure 2.3 for incident γ-ray energies of 200 keV, 500 keV and 2000 keV. The Klein-Nishina formula, given by [34]

$$\frac{d\sigma}{d\Omega} = \frac{e^2}{4\pi\epsilon_0 mc^2}\left[\frac{1}{1+\alpha(1-\cos\theta)}\right]^2\left[\frac{1+\cos^2\theta}{2}\right] \times\left[1+\frac{\alpha^2(1-\cos\theta)^2}{(1+\cos^2\theta)\left[1+\alpha(1-\cos\theta)\right]}\right] \tag{2.22}$$

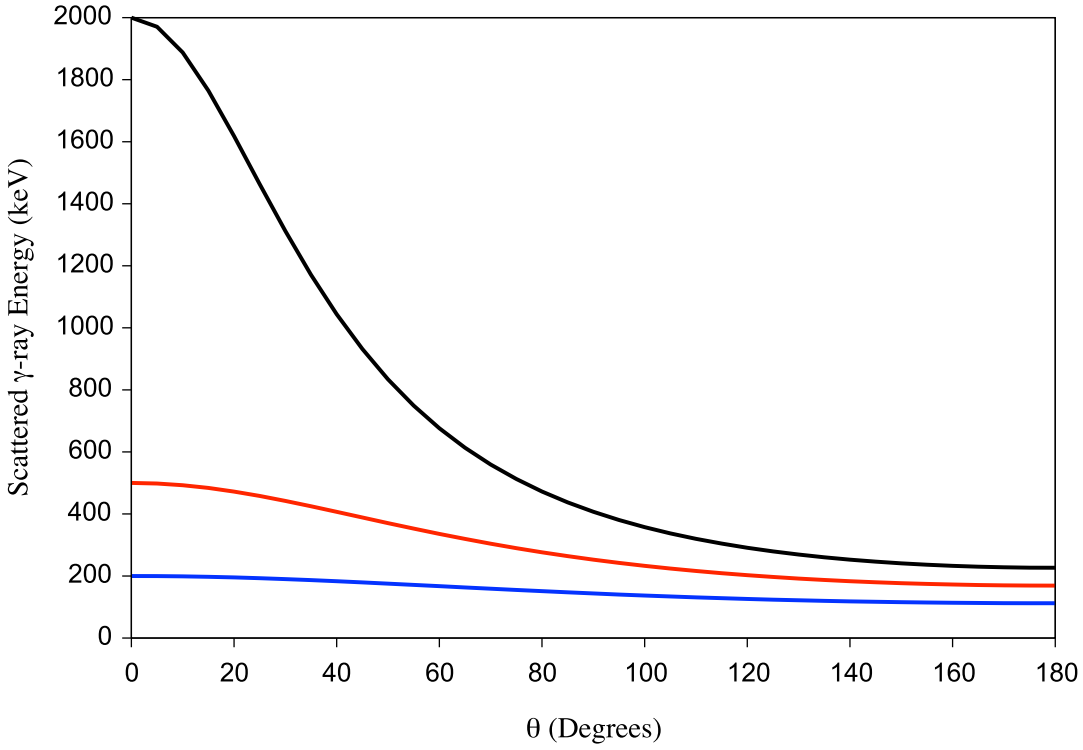

Figure 2.3: Compton scattered γ-ray energy as a function of scattering angle for initial γ-ray energies of 200 keV (blue), 500 keV (red) and 2000 keV (black), calculated using equation 2.21.

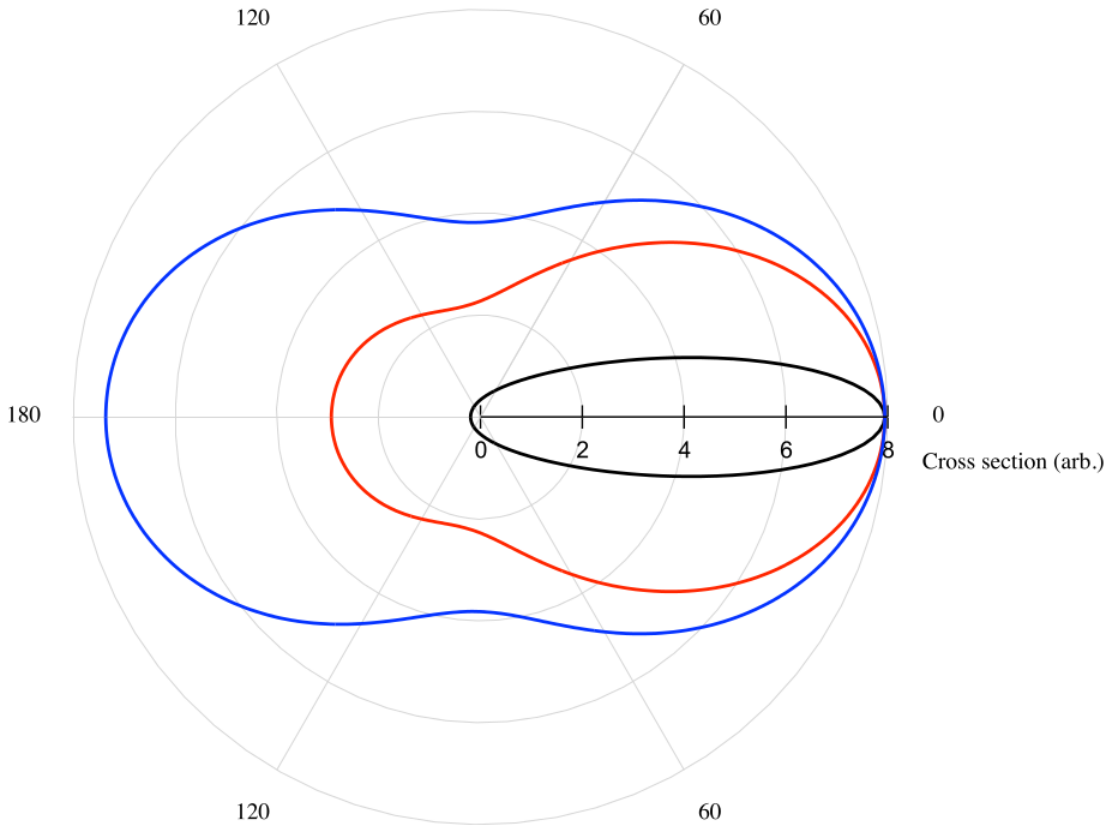

Figure 2.4: A polar plot (degrees) of the cross section for Compton scattering, calculated using equation 2.22, for incident photon energies of 10 keV (blue), 200 keV (red) and 5000 keV (black).

provides the differential cross section for Compton scattering as a function of scattering angle, where θ is the scattering angle and α is the incident γ-ray energy in units of the electron rest energy. This function is plotted in polar form in Figure 2.4 for incident γ-ray energies of 10 keV, 200 keV and 5000 keV.

In a HPGe detector, events in which a γ ray interacts via Compton scattering but leaves the detector material before depositing its full energy lead to a Compton continuum in the γ-ray energy spectrum. This background can be reduced by surrounding the HPGe detector with additional high-efficiency detector material.

When the outgoing Compton scattered γ ray is detected in the high-efficiency material, the signal from the HPGe detector is rejected. Bismuth-Germante (BGO) is commonly used for this purpose, as in the present work.

At high γ-ray energies pair production is the dominant process. This is the process in which an electron-positron pair is created. The energy threshold for this process is 1.022 MeV since at least twice the rest mass energy of the electron is required. The residual energy is shared equally as kinetic energy between the electron and positron. Both the electron and positron are unlikely to escape the detector material as they will have already lost most of their kinetic energy after a few millimetres [51]. Once stopped, the positron will annihilate with an electron from the detector material producing two 511-keV γ rays. If the energy of both of these γ rays is fully absorbed by the detector material, the full energy of the original incident γ ray will have been deposited. If one, or both, of the 511 keV γ rays escape the detector material without depositing their energy then single- and double-escape peaks, at 511 keV and 1022 keV below the photopeak, will be observed in the spectrum.

Chapter 3

Experimental Arrangement

Isotopically-enriched ^{152}Sm and ^{154}Sm targets, of 98% and 99% purity respectively, were bombarded with 25-MeV protons from the K-150 cyclotron at the Cyclotron Institute of Texas A&M University. The thickness of the targets was approximately 1 mg/cm^2. The ^{152}Sm target was bombarded for 42 hours and the ^{154}Sm target for 35 hours with average beam currents of 1.4 nA and 1.2 nA respectively. The live time was 68% for the ^{152}Sm target runs and 66% for the ^{154}Sm target runs. The outgoing light ions and γ rays were detected using the STARLiTeR array, as described in the following sections.

3.1 The STARLiTeR Array

The STARLiTeR array was utilised at the Cyclotron Institute of Texas A&M University and consists of STARS (Silicon Telescope Array for Reaction Studies) and LiTeR (Livermore Texas Richmond). LiTeR is an array of six Compton suppressed HPGe clover detectors. A schematic diagram of the experimental arrangement is

shown in Figure 3.1. An aluminium target chamber housed STARS and the target wheel as shown in the photograph in Figure 3.2. The side of the chamber was 4 mm thick and the diameter of the chamber was 25.1 cm. The dimensions of the chamber are described in detail in reference [52]. An aluminium δ-shield was positioned between the target position and STARS in order to shield the silicon from secondary electrons. An aluminium tube passed through the center of STARS in order to shield the inner rings of the telescope from scattered beam particles. The six BGO shielded HPGe clover detectors were positioned in pairs at angles of 47°, 90° and 133° with respect to the incident proton beam at a distance of 13 cm from the target position.

3.2 STARS

STARS is a highly segmented silicon telescope for the detection of charged particles which can be assembled in a ΔE-E1 or ΔE-E1-E2 configuration. In the present work, the ΔE-E1 configuration was used. The distance between the target and the ΔE detector was 18 mm and the distance between the ΔE detector and the E1 detector was 5 mm. The S2 detectors manufactured by Micron were used. These are annular detectors segmented into 48 rings and 16 sectors. Each ring has a width of 0.5 mm. The distance from the centre of the detector to the inner edge of the active material was 11 mm and the distance from the centre to the outer edge of the active material was 35 mm. In the present work, the outputs of pairs adjacent of rings and sectors were combined to form 24 ring outputs and 8 sector outputs. The active area was 35 cm^2. A 0.14 mm thick ΔE detector and 1 mm thick E1 detector were used. A dead layer of 1000 Å of aluminium was on the ring

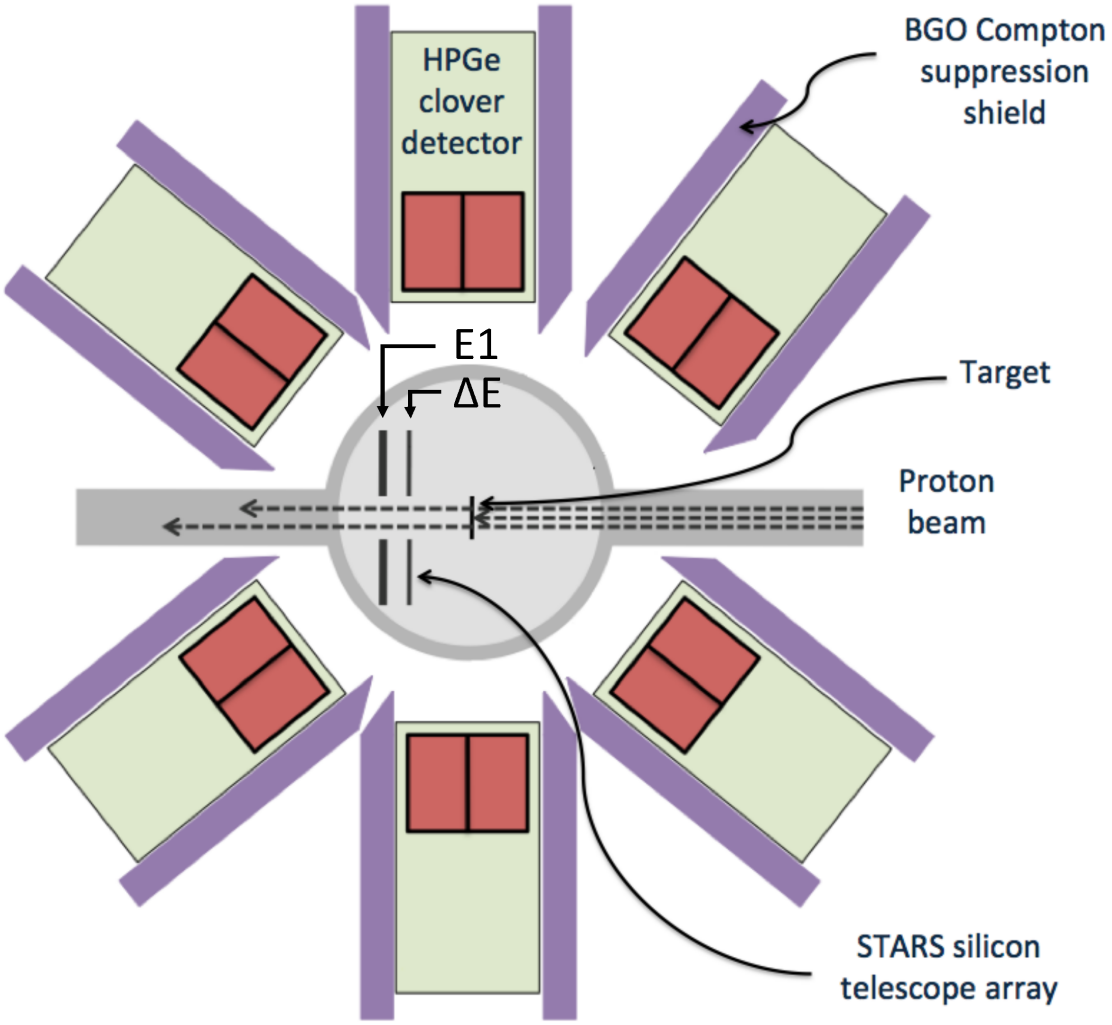

Figure 3.1: A schematic diagram of the STARLiTeR array which consists of the STARS silicon telescope and the LiTeR array of six BGO shielded HPGe clover detectors. This figure is a modified version of Fig. 1 from reference [53].

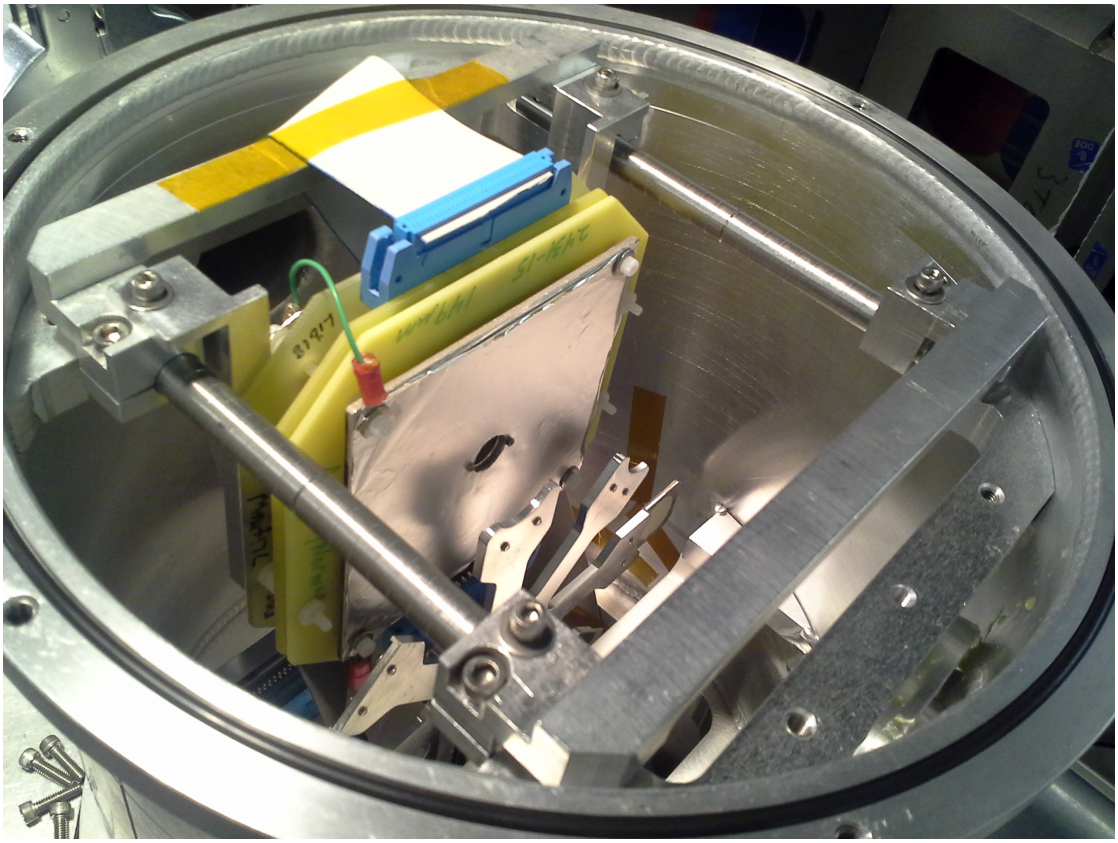

Figure 3.2: Photograph of the aluminium chamber containing the target wheel and STARS in the ΔE-E1-E2 configuration. The aluminium δ-shield positioned in front of STARS can be seen. The beam is incident from the lower right corner of the image.

side of the detector and a 3000 Å layer of gold was on the sector side. The angular coverage of the detector was from 34 to 58 degrees.

3.2.1 STARS Energy Calibration

The energy deposited in the Si detectors may be read from either the ring or sector outputs. In the present work, the energies were obtained from the ring side as this provided the best resolution. The energy deposited in adjacent rings was summed within a single detector event, and the angle for these events was calculated using the ring with the largest recorded energy. The telescope was calibrated first using a ^{226}Ra source, which provides α-particles at energies of 4601, 4784, 5304, 5490, 6002 and 7687 keV. An energy spectrum from the ΔE detector produced using the ^{226}Ra source is shown in Figure 3.3. In beam, a natural carbon target was used to produce a ^{12}C(p,p') excitation energy spectrum, shown in Figure 3.4, which provided 9 additional calibration points between 4439 and 16106 keV. Finally, well known levels at low excitation energy populated in the ^{152,154}Sm(p,d) and ^{152,154}Sm(p,t) reactions were used. The energy losses for protons, deuterons and tritons passing through the Al and Ag dead layers were calculated using the ELAST (Energy Loss And Straggling Tool) program [54]. The induced noise in neighbouring rings produced in multi-ring events was corrected for.

The excitation energy, E^*, of the residual nucleus is given by

$$E^* = E_b + Q - E_t - E_r \tag{3.1}$$

where Q is the Q-value of the reaction, E_t is the energy of the outgoing particle measured in STARS, E_b is the incident beam energy and E_r is the recoil energy.

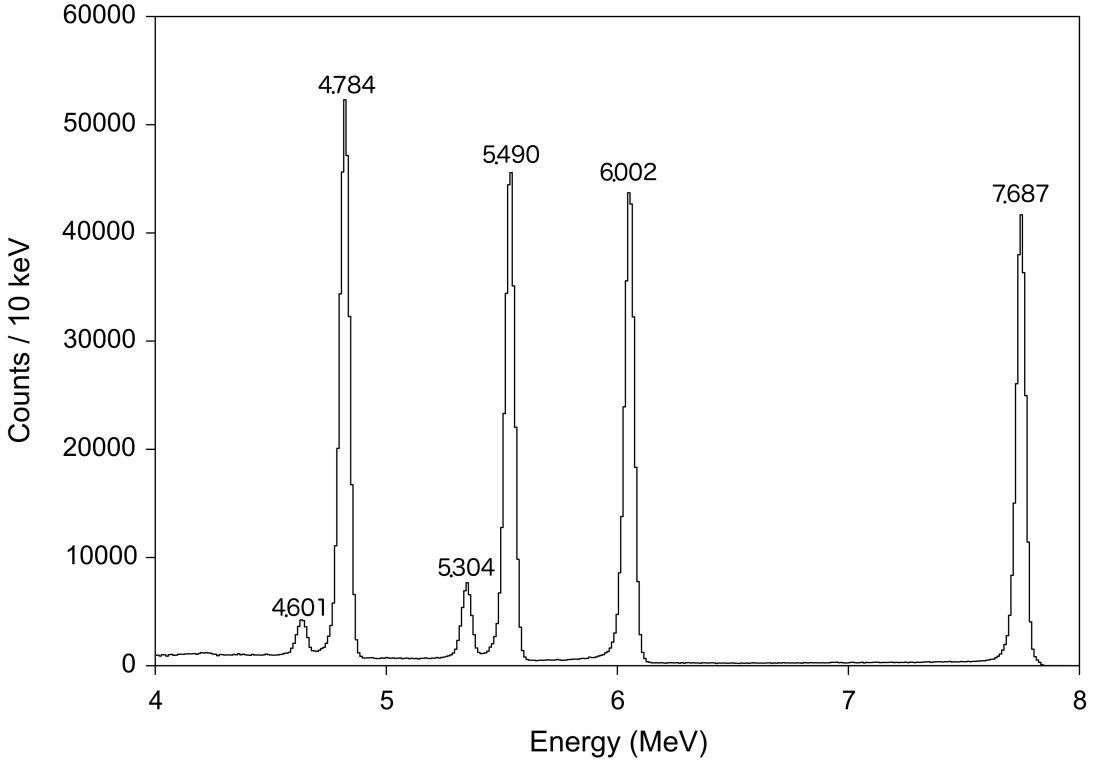

Figure 3.3: Energy spectrum of α-particles emitted from a ^{226}Ra source, measured using the ΔE detector.

The reaction Q-values from the NNDC database [35] were used. A final energy resolution (FWHM) of 130 keV was obtained for the ground state of ^{150}Sm in the ^{152}Sm(p,t) reaction.

3.2.2 Particle Identification

The outgoing light ions (protons, deuterons and tritons) were identified according to their mass and charge by plotting the energy deposited in the ΔE detector against that deposited in the E1 detector, as shown in Figure 3.5. For two particles of identical kinetic energy the heavier particle will have the lower velocity and will therefore deposit more energy in the ΔE detector according to Equation 2.20. The

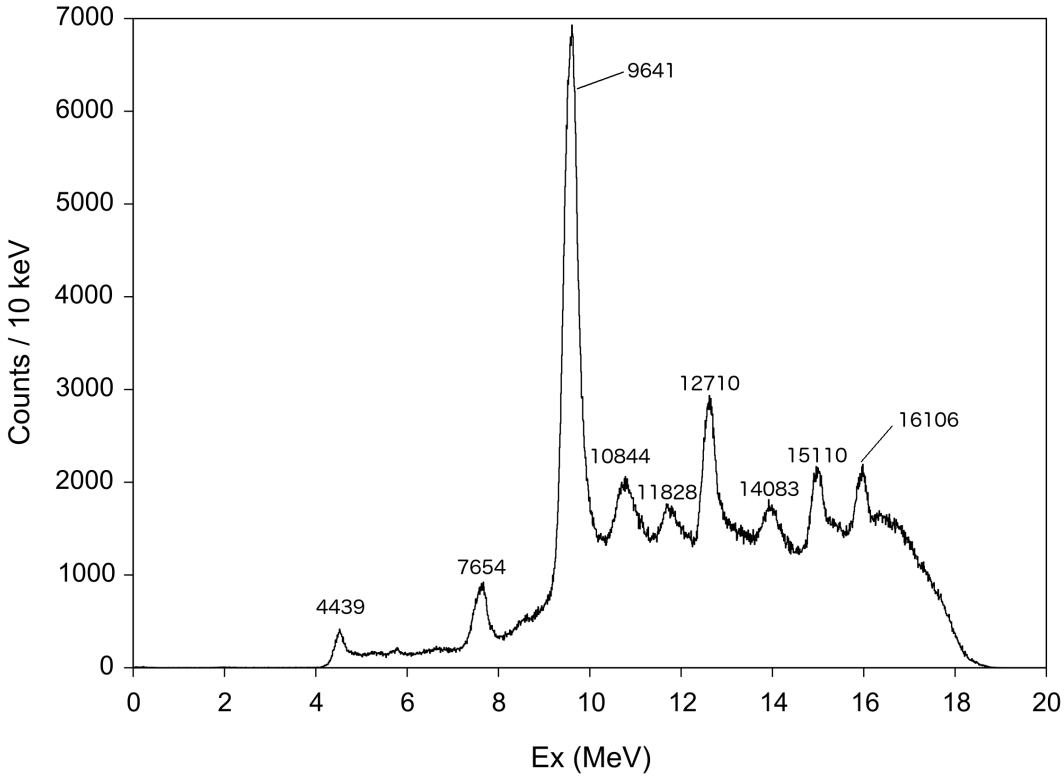

Figure 3.4: ^{12}C(p,p') excitation energy spectrum produced using a natural carbon target. Below an excitation energy of 4 MeV the spectrum is cut off due to the protons not stopping in the E1 detector (lower excitation energies correspond to higher particle energies). The peaks correspond to states of known energy in the NNDC database [35] and are labelled in keV.

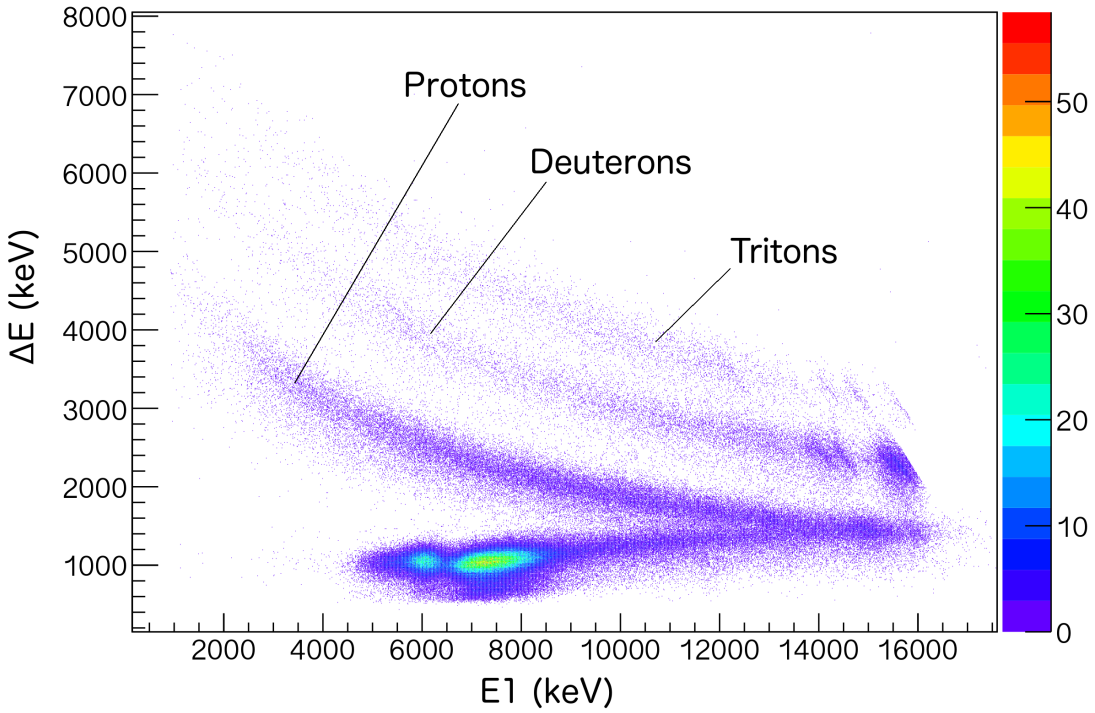

Figure 3.5: Particle identification plot produced using the STARS telescope for the ^{152}Sm(p,t) reaction. Bands corresponding to protons, deuterons and tritons are labelled. The back-bending in the proton curve is due to protons not stopping in the E1 detector.

back-bend in the proton curve is due to protons punching through the E1 detector. In this case the energy deposited in the E1 detector decreases with particle energy due to the increasing particle velocity.

3.2.3 Ray-trace

In order to reduce the background caused by scattered particles that do not originate from the target, the events in the STARS silicon telescope are ray-traced back to the target position. A plot of the intensity in the ΔE detector rings against the intensity in the E1 detector rings is shown in Figure 3.6. For each ΔE ring a

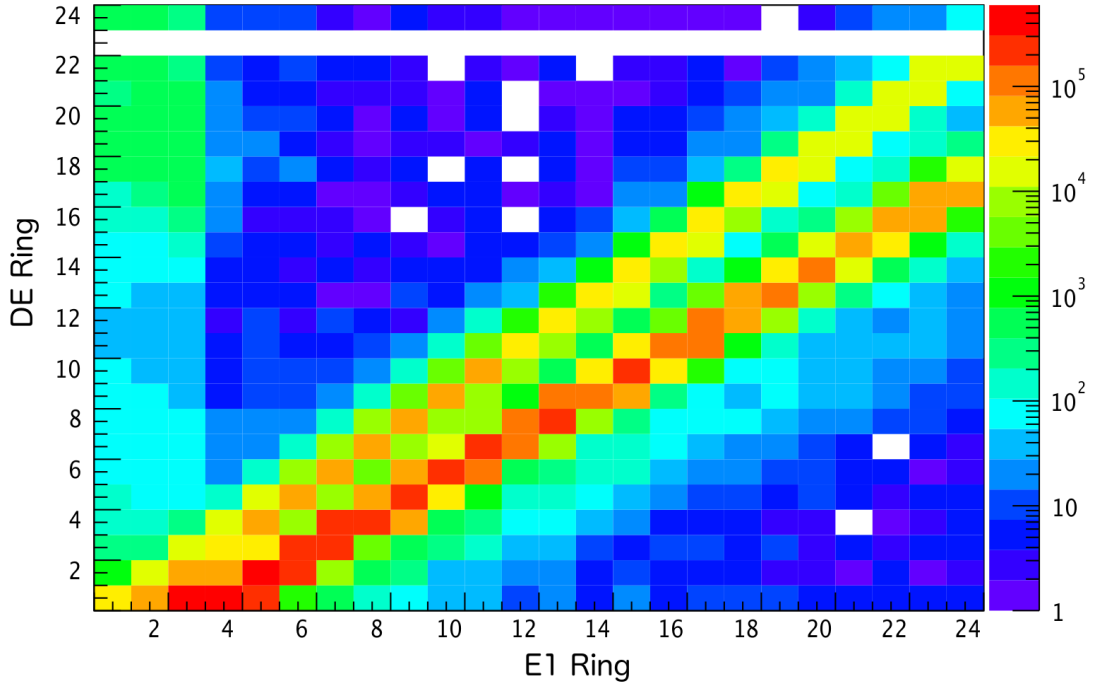

Figure 3.6: A ray-trace diagram (Log scale on the z-axis). Each ring is labelled with an integer, starting from 1 for the innermost ring and increasing to 24 for the outermost ring. The most intense line in the figure corresponds to particles that originated from the target position. The weaker line with a steeper gradient corresponds to particles scattered from an upstream collimator. Ring 23 of the ΔE detector was not used as event times from this ring were not available.

range of rings in the E1 detector is specified for which events are accepted. The most intense line with the shallower gradient in Figure 3.6 is consistent with the measured ΔE-E1 distance of 5 mm and the target-ΔE distance of 18 mm. A gate was placed on these events. The second most intense line corresponds to particles travelling almost parallel to the beam line and is partly due to scattering from an upstream collimator.

3.2.4 Off-Centred beam

A two-dimensional plot of the intensity of the outgoing light ions observed in the ΔE detector rings and sectors is shown in Figure 3.7. The non-uniform distribution of counts in the sectors shows that the beam spot was off-centre with respect to the telescope. This was accounted for when measuring the angular distributions of the outgoing light ions and determining the energy losses in the dead layers. The displacement of the beam spot from the centre was determined by matching ring-sector pixels of the same intensity. Perpendicular bisectors can then be drawn between each pair and the point at which the lines intersect provides an estimate of the beam spot position. Using this method, the beam spot was calculated to be 1.2(3) mm displaced from the centre in the direction of Sector 7.

3.3 LiTeR

The γ-ray detection array LiTeR consists of six BGO-shielded HPGe clover detectors. Each detector consists of four high-purity germanium crystals arranged in the shape of a four-leaf clover. The energy deposited in adjacent crystals was summed in the process known as add-back. The detectors were positioned in pairs at angles of 47°, 90° and 133° with respect to the incident proton beam at a distance of 13 cm from the target position.

3.3.1 LiTeR Energy Calibration

The HPGe clover detectors were calibrated using the standard γ-ray calibration sources ^{22}Na, ^{54}Mn, ^{57}Co, ^{60}Co, ^{109}Cd, ^{133}Ba, ^{137}Cs and ^{152}Eu. A final energy

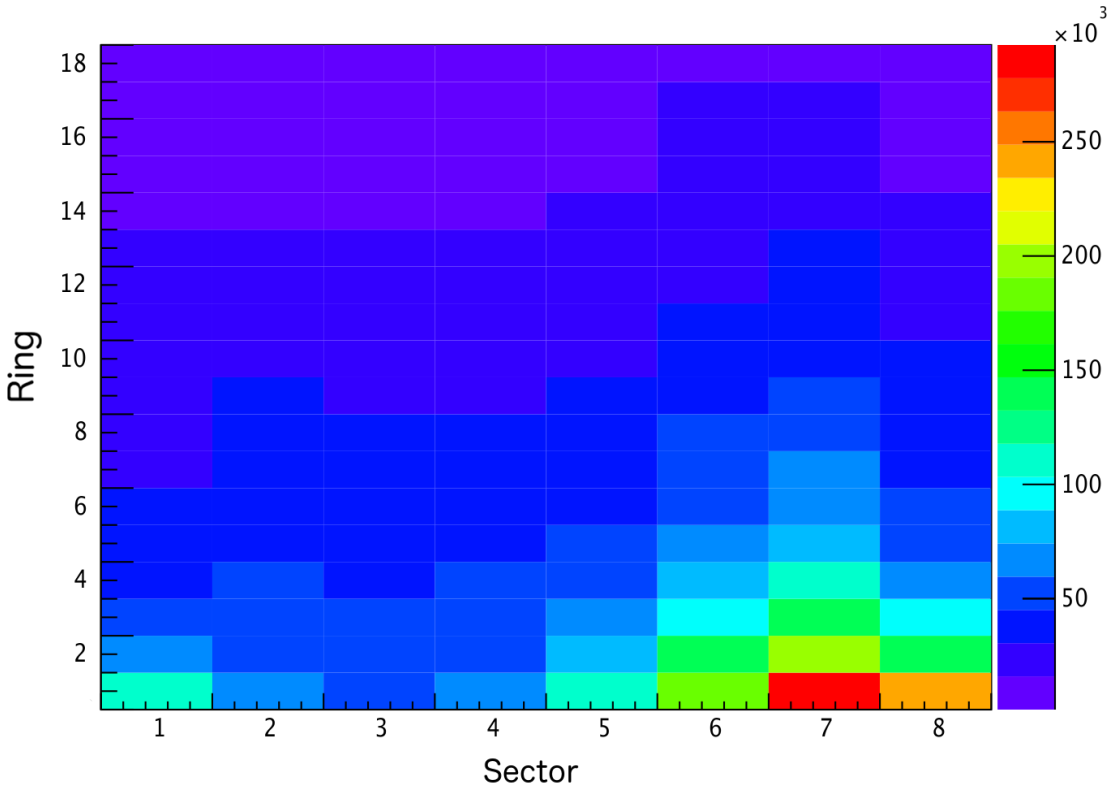

Figure 3.7: The distribution of counts in the ΔE detector rings and sectors.

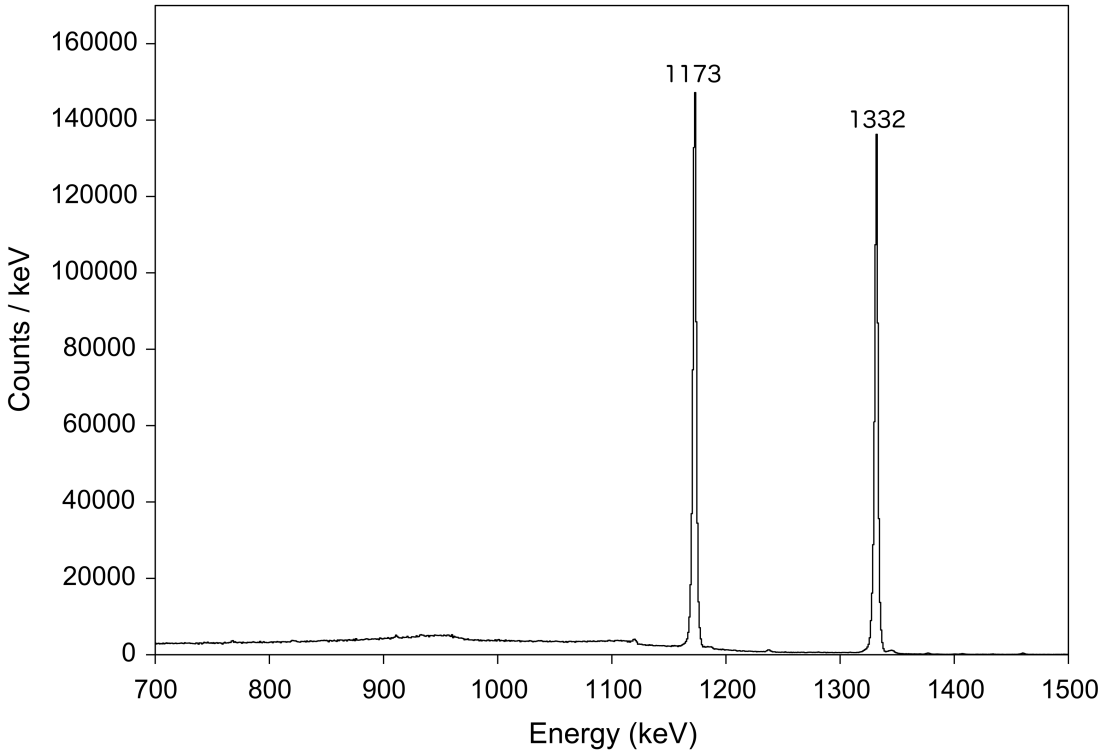

Figure 3.8: γ-ray energy spectrum produced using a ^{60}Co source.

resolution of 2.6 keV and 3.5 keV (FWHM) was obtained at 122 keV and 963 keV respectively. A γ-ray energy spectrum, Compton suppressed and with leaf add-back, produced using the ^{60}Co source is shown in Figure 3.8.

3.3.2 LiTeR Efficiency Calibration

A measurement of the γ-ray photopeak detection efficiency is required in order to extract few nucleon transfer cross-sections using the particle-γ coincidence technique. An efficiency calibration was obtained using ^{22}Na, ^{57}Co, ^{60}Co, ^{133}Ba, ^{137}Cs and ^{152}Eu γ-ray sources of known intensity. The efficiency curve for the entire array, with leaf add-back and Compton suppression, is shown in Figure 3.9. The

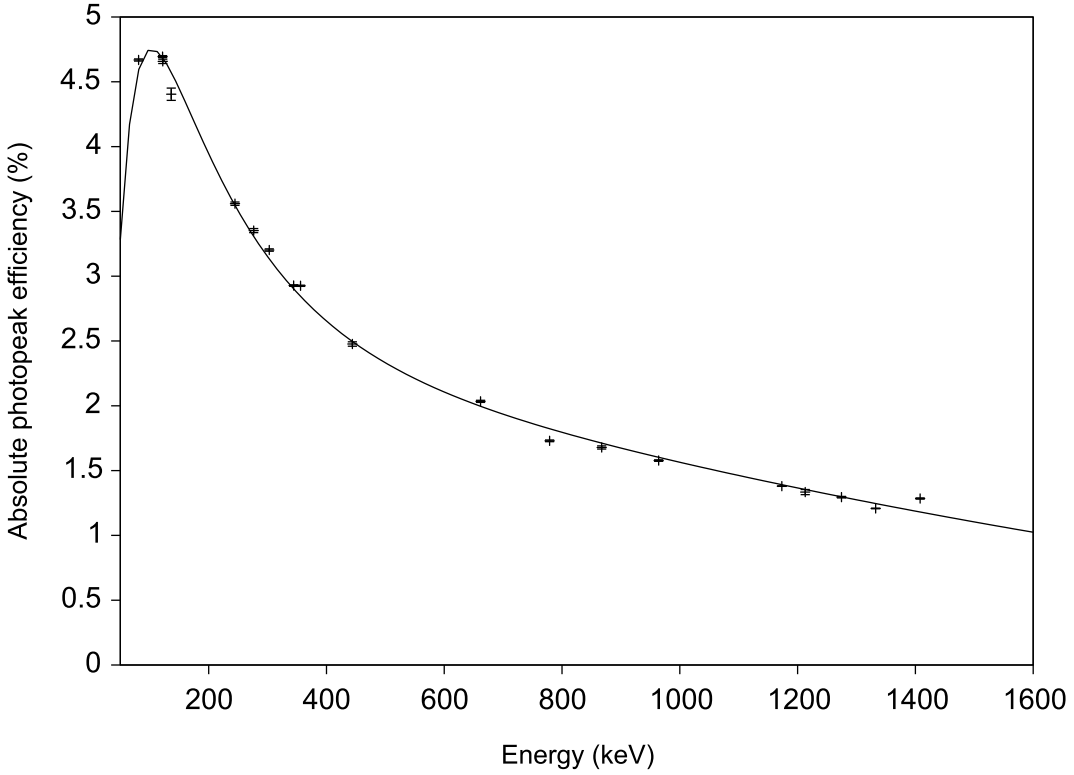

Figure 3.9: The absolute photopeak efficiency of the LiTeR array, plotted as a function of γ-ray energy, with leaf add-back and Compton suppression enabled. The line shows the function given by Equation 3.2 fitted to the data.

branching ratios were obtained from the NNDC database [35]. The dead time of each calibration run and sum-peak effects were accounted for. The function

$$\epsilon(x) = \left(Ax + \frac{B}{x}\right) \exp\left(Cx + \frac{D}{x}\right), \tag{3.2}$$

where A, B, C and D are constants, was fitted to the data and reproduces the expected decrease in efficiency at the lowest and highest γ-ray energies.

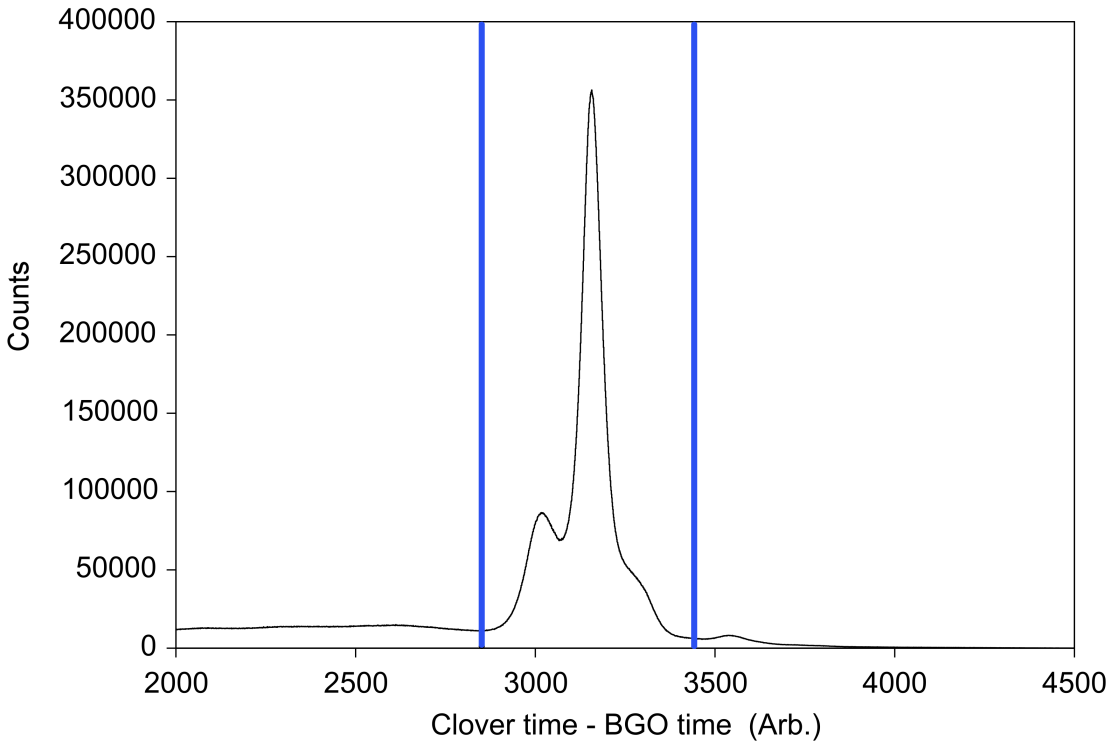

Figure 3.10: The clover-BGO time differences. The events between the two blue lines were rejected as Compton scattering events.

3.3.3 Compton Suppression

When a γ ray was detected in a BGO shield any coincident signal from the corresponding clover detector was vetoed in order to suppress Compton scattering events. The time differences between the BGO signals and the signals from the clover detectors are shown in Figure 3.10 where the gate for event rejection is indicated by the blue lines.

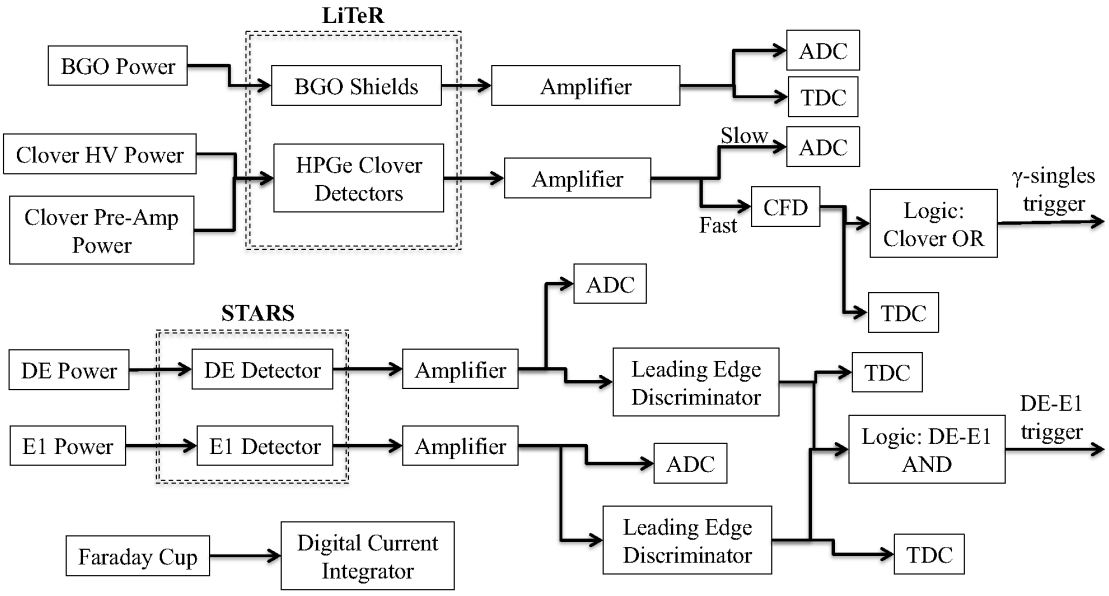

Figure 3.11: Schematic diagram of the STARLiTeR electronics used during the experiment. The DE-E1 trigger provides the start signal for the TDCs during in-beam measurements.

3.4 Electronics

A schematic diagram of the STARLiTeR electronics is shown in Figure 3.11. The γ-singles trigger was used during the γ-ray energy and efficiency calibrations, and also during out-of-beam measurements of the activated targets. The ΔE-E1 trigger was used for the in-beam data. The particle spectra obtained with the ΔE-E1 trigger, such as those shown later in Figure 4.1, are referred to as *particle singles* spectra.

3.5 Particle-γ Coincidences

Particle-γ coincidences are a powerful spectroscopic tool, see for example Reference [36] in which a similar setup to that used in the present work is used to identify

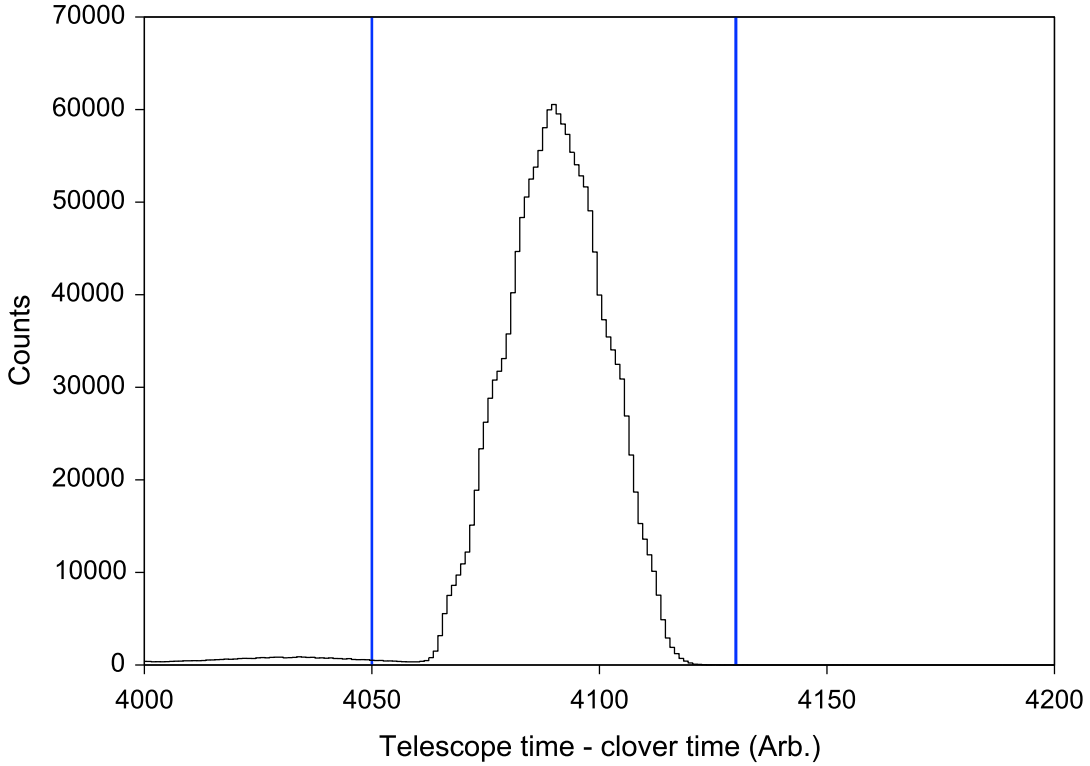

Figure 3.12: The time differences between the particle and γ-ray events. The telescope time was obtained from the ring in the ΔE detector with the highest energy. The clover time was obtained from the leaf with the highest energy. The events between the two blue lines were accepted as particle-γ coincidences.

new levels and γ-ray transitions in ^{155}Gd using the (p,d-γ) reaction. The time differences between the particle and γ-ray events are plotted in Figure 3.12 where the gate defining the particle-γ coincidence condition is indicated by the blue lines. A triton-γ matrix from the ^{152}Sm(p,t) reaction is shown in Figure 3.13. The horizontal lines in this figure correspond to γ rays from states that are strongly fed by a large number of levels spanning a wide range of excitation energies.

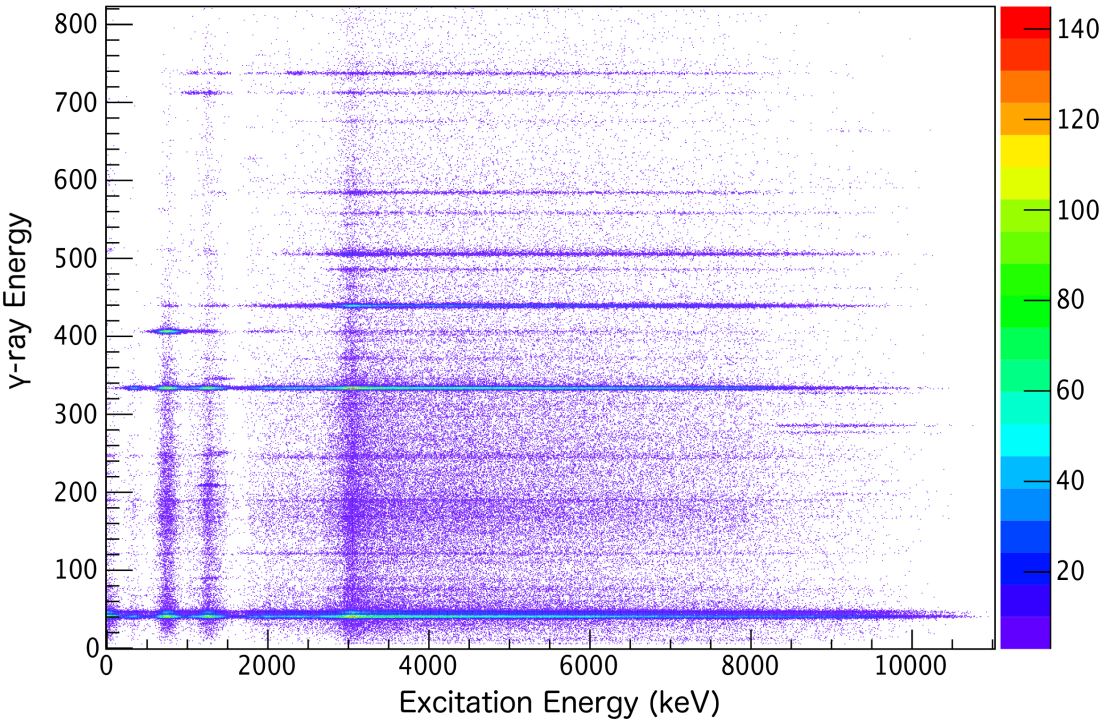

Figure 3.13: A triton-γ coincidence matrix from the ^{152}Sm(p,t) reaction. The intense horizontal line at approximately 40 keV corresponds to Sm X-rays. The line at a γ-ray energy of 334 keV is the transition from the 2_1^+ level in ^{150}Sm to the ground state.

Chapter 4

Results and Discussion

4.1 Triton singles spectra and triton-γ matrices

The triton singles spectra from the ^{152,154}Sm(p,t) reactions are shown in Figure 4.1. At low excitation energy, below approximately 2.5 MeV in ^{150}Sm and 2 MeV in ^{152}Sm, the region of strongly populated discrete states can be seen. The three largest peaks at low excitation energy in the ^{150}Sm spectrum correspond to the population of the ground state and the first two excited 0^+ states. At approximately 3 MeV in ^{150}Sm and 2.3 MeV in ^{152}Sm the peak-like structure (PLS) can be observed, immediately prior to the smooth continuum region at higher excitation energy. In Figure 4.2 the triton projections from the t-γ matrices from the ^{152,154}Sm(p,t) and the ^{154,156,158}Gd(p,t) reactions are shown. The Gd data is from the studies by Ross *et al.* [28] and Allmond *et al.* [29]. The dashed lines indicate the single neutron separation energies. The data from Ross and Allmond were obtained using a similar experimental arrangement to that used in the present work. It can be seen that the resolution of the tritons is much improved for the

Sm data. The triton energy resolution (FWHM) was 380 keV for the ^{156}Gd(p,t) reaction, which compares to the value of 130 keV obtained in the present work. It can be seen in the figure that the PLS is also present in all three Gd nuclei.

The method for identifying discrete states is provided in Section 4.2, and comments on the observed levels and γ-ray transition are provided in Sections 4.4 and 4.5. The angular distributions for the observed discrete states and the PLS are presented in Section 4.6 and the measured relative partial cross sections are discussed in Section 4.7. The PLS is discussed in detail in Section 4.8. The levels and γ-ray transitions identified in the present work have been published in Physical Review C [55], where the PLS is also discussed. A measurement of isomeric lifetimes in ^{152}Eu, produced via the $(p, 3n)$ reaction, obtained by measuring the activated target out-of-beam is discussed in Section 4.9 and has been published in Physical Review C [56].

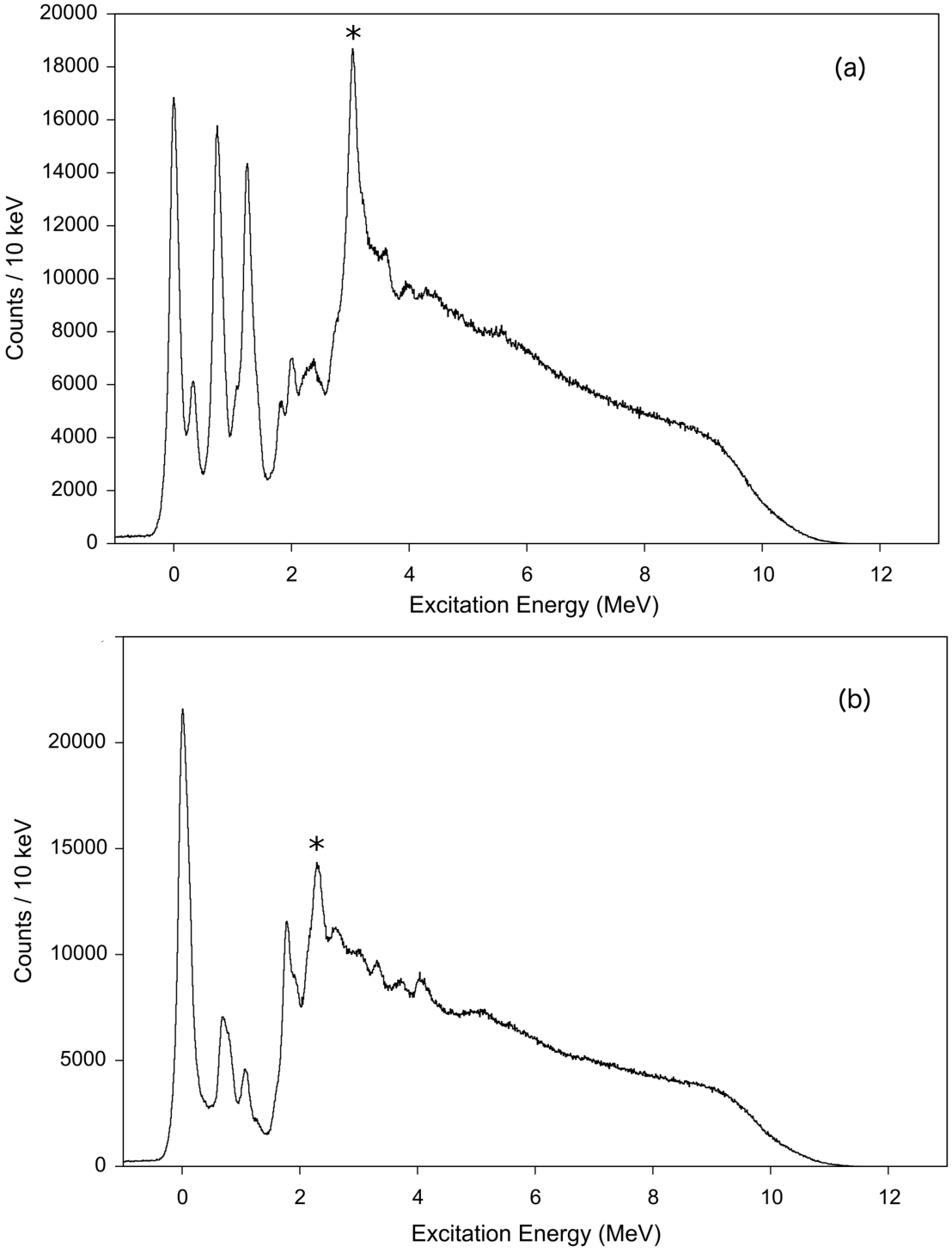

Figure 4.1: The triton singles spectra from the (a) ^{152}Sm(p,t) and (b) ^{154}Sm(p,t) reactions. The discrete states at low excitation energy and the high energy continuum region can be seen. The PLS is indicated by an asterisk.

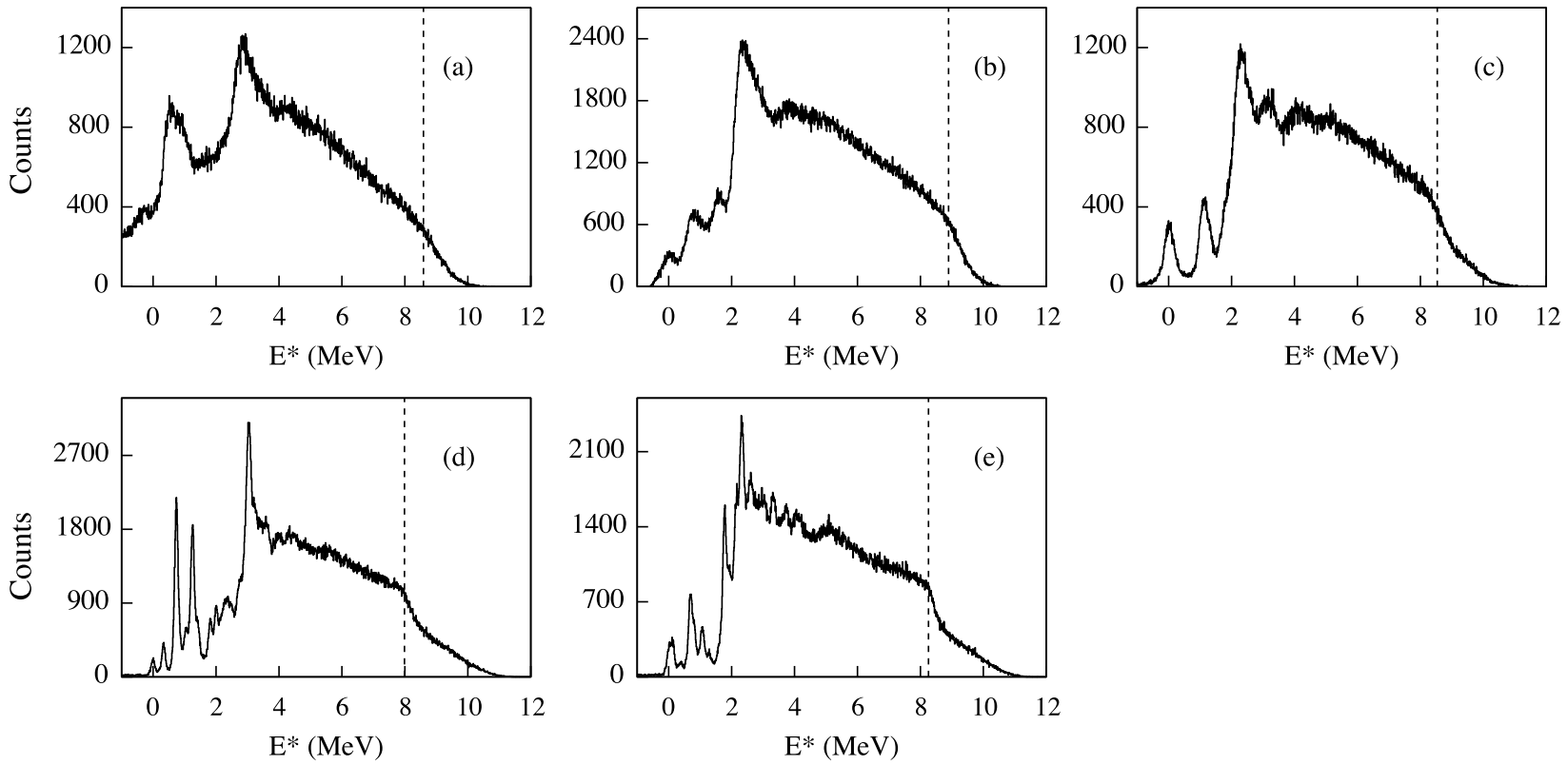

Figure 4.2: Triton projections of the (t-γ) matrices from the (a) ^{154}Gd(p,t), (b) ^{156}Gd(p,t), (c) ^{158}Gd(p,t), (d) ^{152}Sm(p,t) and (e) ^{154}Sm(p,t) reactions. The dashed lines indicate the single neutron separation energies. The Gd data is from the studies by Ross *et al.* [28] and Allmond *et al.* [29].

4.2 Method for identifying discrete states

In this section, the method used to identify discrete states in ^{150,152}Sm using the triton-γ coincidence technique is outlined. In the present work, assignments cannot be made solely using the triton singles spectra due to the relatively low energy resolution and the rapidly increasing level density above approximately 2 MeV in excitation energy. Triton-γ coincidences provide a powerful tool with which to identify new levels and γ-ray transitions. Firstly, a gate is placed on the excitation energy range of interest on the triton projection from the t-γ coincidence matrix. The triton projections are shown in Panels (d) and (e) of Figure 4.2 for the ^{152,154}Sm(p,t) reactions. The resultant γ-ray energy spectrum contains only γ rays that are emitted from levels at or below the energy of the gate. This process often reveals low intensity transitions that are obscured in the total γ-ray projection. Back-gating on a γ ray of interest yields a triton energy spectrum that typically consists of a narrow peak at low excitation energy, corresponding to the direct population of the γ-ray emitting level, and counts at higher excitation energy which correspond to states feeding that level. By fitting the energy of the triton peak corresponding to direct population the approximate excitation energy of the level can be determined, with a typical uncertainty of approximately 10 keV. The energy of the γ ray may then be subtracted from the triton peak energy and often reveals the level that is being fed by the transition. However, the transition may only be placed unambiguously when either there are multiple observed γ rays depopulating the level, when the placement can be confirmed using γ-γ coincidences, or when there is only one possible level that may be fed within the experimental uncertainty. By summing the γ-ray energy with the well-known

energy of the level that is being fed, the precise energy of the γ-ray emitting level may be determined with a typical uncertainty of 0.2 keV.

As an example, the level at 3037.8(9) keV in ^{150}Sm is considered. It can be seen in Table 4.1 that γ-ray transitions were observed at energies of 2702.9(13) keV and 3038.5(12) keV. As shown in Figure 4.3, a gate placed on the 2702.9(13) keV transition produces a triton energy spectrum with a peak corresponding to an excitation energy of 3042(8) keV. Subtracting the γ-ray energy from the triton peak energy gives a value of 339(8) keV for the energy of the level that is being fed. If the transition is a primary γ ray from the level at 3042(8) keV, then there is only one possible final level within the experimental uncertainty, the 2^+ state at 334 keV. The γ-ray energy from the present work may then be summed with the precise energy level energy of 334.955(10) keV from the NNDC database [35] resulting in a level energy of 3036.9(13) keV. Similarly, the 3038.5(12) keV transition may be subtracted from the energy of the coincident triton peak of 3060(18) keV, resulting in an energy of 22(18) keV for the final state. It is clear that this is a transition to the ground state, and so the energy of the level is simply the energy of the γ-ray transition. The final level energy of 3037.8(9) keV is the weighted average of the level energies of 3036.9(13) keV and 3038.5(12) keV determined from the individual γ-rays. The NNDC database lists a level at 3038.2(4) keV with γ-ray transitions at 2704.6(7) keV and 3037.8(keV), which are consistent with the energies measured in the present work. The relative γ-ray branching intensities measured in the present work are also consistent with the NNDC values, within the experimental uncertainty.

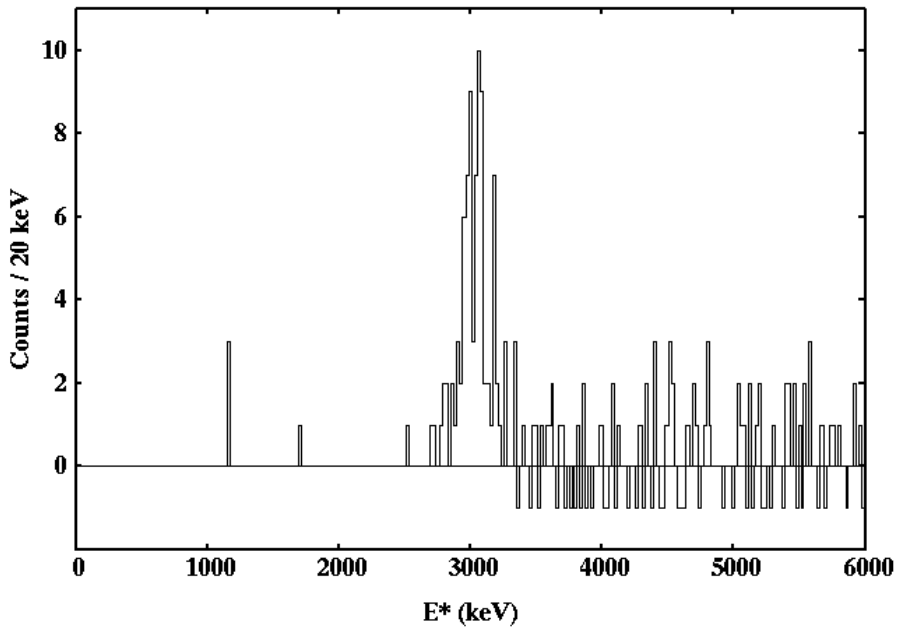

Figure 4.3: Triton energy spectrum in coincidence with the 2702.9(13) keV transition from the level at 3037.8(9) keV in ^{150}Sm.

4.3 Individual Levels and γ-ray transitions

In the following sections the individual levels in ^{150}Sm and ^{152}Sm, observed in the ^{152}Sm(p,t) and ^{154}Sm(p,t) reactions respectively, are discussed. The full list of observed levels is given in Tables 4.1 and 4.2. In the first column, the energy of the level evaluated in the present work is given. In the second and third columns, the γ-ray energy and relative γ-ray branching is listed. The γ-ray branching intensities are given relative to the strongest transition from each level and the strongest transition has been scaled to 100. In the fourth column, the energy of the triton peak corresponding to the direct population of the level in coincidence with the γ ray from the same row is listed. In the fifth column, the γ-ray energy is subtracted from the triton peak energy which can be compared to the NNDC level energy in the sixth column. The energies in the fifth and sixth columns must be consistent

within the experimental uncertainty. A dash in columns 4 and 5 indicates that the triton peak corresponding to the direct population of the level was not measured in coincidence with the γ ray in the same row. This can occur when a level is strongly fed by higher-lying states. In the seventh column, the γ-ray energy from the present work is summed with the NNDC energy of the level that is being fed in order to determine the precise level energy. In the following four columns the NNDC spin and parity, level energy, γ-ray energy and relative γ-ray branching intensities are listed in order to compare to those obtained in the present work. In the final column, the relative partial cross section, angle averaged over the angular range of the telescope of 34°-58°, is given. The cross sections are relative to that of the 2_1^+ state in the same nucleus, which has been scaled to 100. These relative cross sections are discussed in detail in Section 4.7. In Sections 4.4 and 4.5, only states for which additional comments are required in order to fully interpret the data in the Tables 4.1 and 4.2 are discussed.

In Figures 4.4 and 4.5, excitation energy is plotted against spin for levels observed to be directly populated in the present work. Newly-observed levels are plotted in red, and the horizontal bars show the possible range of spins for a level. This range of spins was taken from the literature where available, or estimated by using the observed γ-ray decays by assuming that the spin of a level was within two units of angular momentum from the levels it was observed to feed. It can be seen in these figures that the majority of the directly populated levels lie between 0-6$\hbar$ units of angular momentum. The selectivity of the reaction to states of relatively low angular momentum at relatively high excitation energy is clearly apparent.

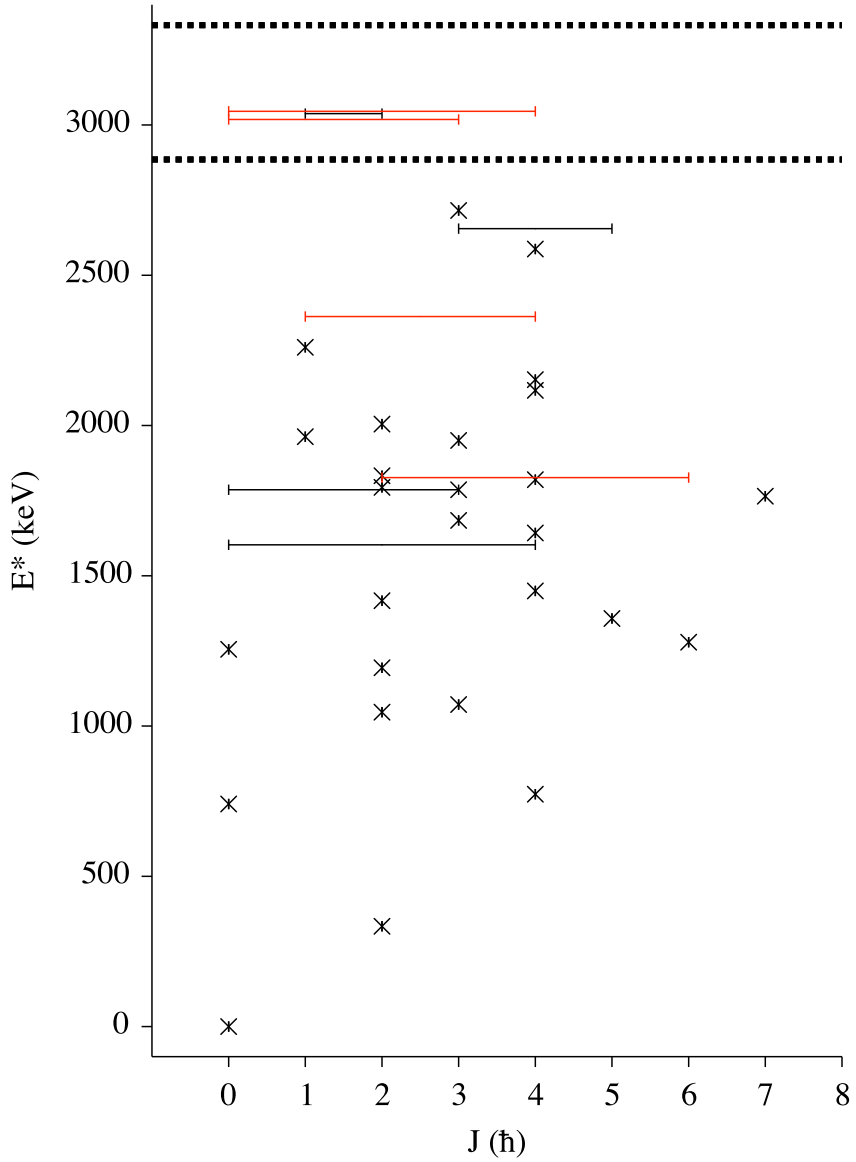

Figure 4.4: Excitation energy plotted against spin for levels observed to be directly populated in ^{150}Sm. The dashed lines indicate the region of the PLS. The black crosses correspond to states for which the spin was previously known. The black horizontal lines correspond to states that had been previously observed but for which the spin was unknown or uncertain. The length of the line corresponds to the possible range of spins for that level, which was either obtained from the literature, or estimated by assuming that the spin of a level was within two units of angular momentum of the states it was observed to feed. The red horizontal lines are the same as the black horizontal lines, except that they correspond to levels newly observed in the present work.

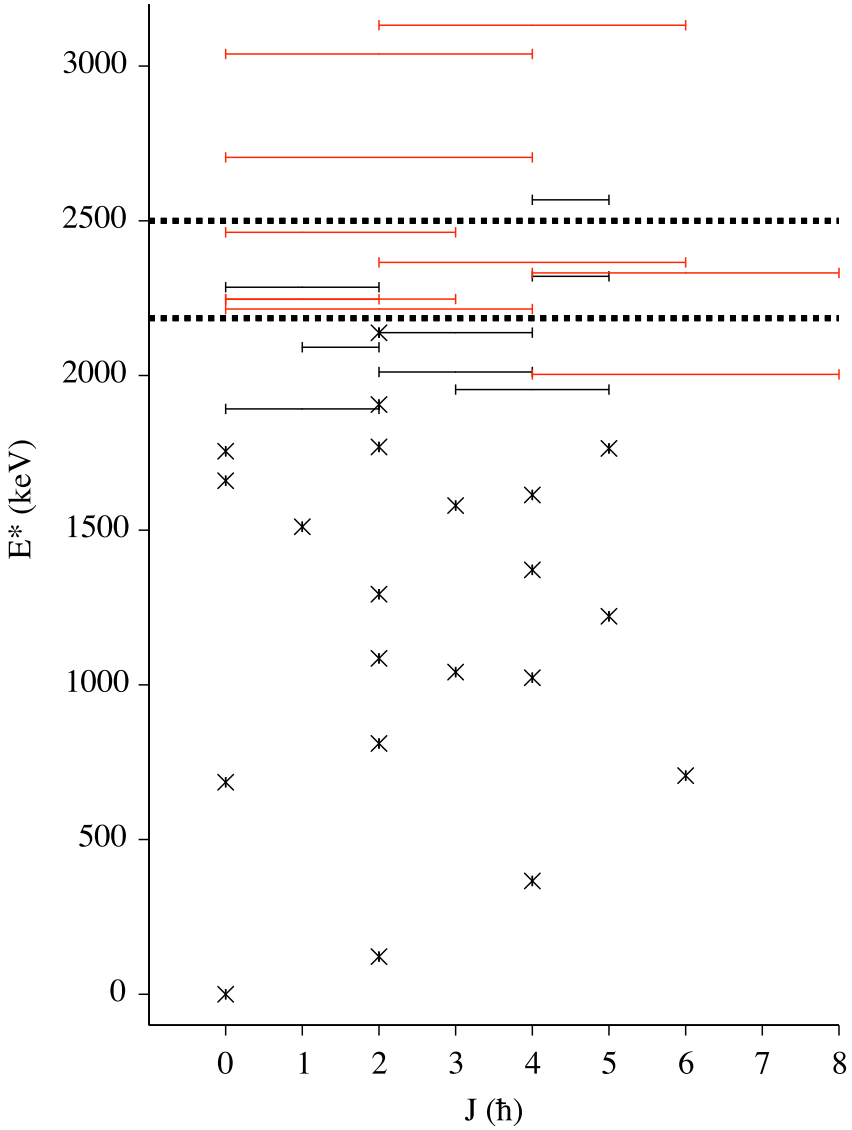

Figure 4.5: Same as Figure 4.4 but for levels populated in ^{152}Sm.

Table 4.1: Levels and γ rays observed in the ^{152}Sm(p,t) reaction. Refer to the text for a full description of each column. The uncertainties are indicated by the superscript. Newly-identified levels and γ rays are shown in bold.

E_x (keV)	E_γ (keV)	I_γ	E_x^t (keV)	E_x^t-E_γ (keV)	E_f^{ND}	E_γ+E_f^{ND} (keV)	$J^{\pi,ND}$	E_x^{ND}	E_γ^{ND}	I_γ^{ND}	$\sigma_{(34°-58°)}$ (% of 2_1^+)
333.7^{2}	333.7^{2}	100	341^{14}	7^{14}	0	333.7^{2}	2^+	333.955^{10}	333.961^{11}	100^{3}	100^{2}
740.6^{2}	406.6^{2}	100	741^{4}	334^{4}	333.96	740.6^{2}	0^+	740.464^{19}	406.508^{22}	100	282^{6}
773.3^{3}	439.3^{3}	100	780^{5}	341^{5}	333.96	773.3^{3}	4^+	773.374^{12}	439.400^{14}	100	9.7^{8}
1046.3^{2}	712.4^{3}	100	1054^{11}	342^{11}	333.96	1046.4^{3}	2^+	1046.148^{13}	712.207^{14}	100^{6}	32^{2}
	1046.2^{2}	6^{2}	1031^{13}	-15^{13}	0	1046.2^{2}			1046.16^{14}	8.1^{9}	
1071.7^{2}	297.5^{5}	8^{2}	-	-	773.37	1070.9^{5}	3^-	1071.406^{12}	298.060^{13}	6.70^{23}	22^{2}
	737.7^{2}	100	1070^{5}	332^{5}	333.96	1071.7^{2}			737.457^{15}	100.0^{19}	
1165.6^{2}	831.6^{3}	84^{5}	-	-	333.96	1165.6^{3}	1^-	1165.791^{17}	831.83^{5}	75^{3}	-
	1165.5^{3}	100	-	-	0	1165.5^{3}			1165.74^{3}	100^{4}	
1193.9^{2}	860.0^{3}	67^{5}	1193^{5}	332^{5}	333.96	1194.0^{3}	2^+	1193.843^{12}	859.88^{3}	73.3^{16}	38^{2}
	1193.8^{2}	100	1194^{4}	0^{4}	0	1193.8^{2}			1193.830^{22}	100^{3}	
1255.4^{1}	209.2^{2}	11^{1}	1258^{4}	1049^{4}	1046.15	1255.3^{2}	0^+	1255.512^{20}	209.364^{19}	8.9^{16}	186^{4}
	921.5^{2}	100	1259^{4}	338^{4}	333.96	1255.5^{2}			921.55^{13}	100^{7}	
1278.9^{2}	505.5^{2}	100	1271^{7}	766^{7}	773.37	1278.9^{2}	6^+	1278.922^{14}	505.508^{23}	100	5.5^{6}

Table 4.1 Continued:

E_x (keV)	E_γ (keV)	I_γ	E_x^t (keV)	E_x^t-E_γ (keV)	E_f^{ND}	E_γ+E_f^{ND} (keV)	$J^{\pi,ND}$	E_x^{ND}	E_γ^{ND}	I_γ^{ND}	$\sigma_{(34°-58°)}$ (% of 2_1^+)
1357.9^{4}	584.5^{4}	100	1365^{7}	781^{7}	773.37	1357.9^{4}	5^-	1357.710^{13}	584.274^{12}	100^{3}	6^{1}
1417.2^{2}	251.2^{4}	48^{5}	1418^{5}	1167^{5}	1165.74	1417.0^{4}	2^+	1417.346^{13}	251.582^{19}	43.7^{18}	30^{2}
	345.8^{3}	100	1417^{4}	1071^{4}	1071.41	1417.2^{3}			345.950^{17}	100^{10}	
	1083.3^{3}	30^{5}	1427^{10}	344^{10}	333.96	1417.3^{3}			1083.34^{4}	70^{8}	
1449.7^{4}	676.3^{4}	100	1454^{12}	778^{12}	773.37	1449.7^{4}	4^+	1449.182^{13}	675.853^{24}	100^{2}	2.3^{6}
1505.2^{6}	1171.2^{6}	100	-	-	333.96	1505.2^{6}	3^+	1504.572^{13}	1170.589^{24}	100.0^{14}	-
1603.1^{7}	**1269.1^{7}**	100	1610^{40}	341^{40}	333.96	1603.1^{7}		1603^{4}			1.1^{4}
1642.6^{7}	869.2^{7}	100	1638^{22}	769^{22}	773.37	1642.6^{7}	4^+	1642.611^{12}	869.256^{14}	100^{1}	2.0^{5}
1684.1^{3}	911.0^{6}	60^{7}	1715^{27}	804^{27}	773.37	1684.4^{6}	3^-	1684.162^{17}	910.88^{4}	50^{6}	3.5^{6}
	1349.9^{4}	100	1698^{20}	348^{20}	333.96	1683.9^{4}			1350.28^{10}	100^{6}	
1764.8^{3}	485.9^{3}	100	1783^{20}	1297^{20}	1278.92	1764.8^{3}	7^-	1764.89^{4}	485.8^{3}	100^{4}	1.1^{3}
1786.3^{5}	620.5^{5}	100	1778^{12}	1158^{12}	1165.79	1786.3^{5}	(≤ 3)	1786.30^{13}	620.40^{20}	95^{16}	1.8^{5}
1794.2^{2}	600.5^{4}	44^{8}	-	-	1193.84	1794.3^{4}	2^+	1794.30^{3}	600.43^{25}	15^{3}	13^{1}
	628.5^{3}	100	1796^{7}	1168^{7}	1165.79	1794.3^{3}			628.56^{14}		
	722.9^{4}	56^{10}	1802^{12}	1079^{12}	1071.41	1794.3^{4}			722.65^{18}	24^{4}	
	1459.9^{4}	42^{10}	1764^{16}	304^{16}	333.96	1793.9^{5}					
1819.9^{2}	748.5^{2}	100	1806^{12}	1058^{12}	1071.41	1819.9^{2}	4^+	1819.510^{13}	748.06^{9}	100^{2}	7.6^{9}
	1485.5^{6}	24^{8}	1828^{26}	343^{26}	333.96	1819.5^{6}			1485.50^{14}	36.7^{15}	

Table 4.1 Continued:

E_x (keV)	E_γ (keV)	I_γ	E_x^t (keV)	E_x^t-E_γ (keV)	E_f^{ND}	E_γ+E_f^{ND} (keV)	$J^{\pi,ND}$	E_x^{ND}	E_γ^{ND}	I_γ^{ND}	$\sigma_{(34°-58°)}$ (% of 2_1^+)
1826.7[3]	**1053.3**[3]	100	1824[8]	771[8]	773.37	1826.7[3]					5.3[7]
1832.8[2]	667.3[3]	48[8]	1834[10]	1167[10]	1165.79	1833.1[3]	$(2)^+$	1833.01[3]	667.05[3]	100[4]	13[1]
	1498.7[2]	100	1832[8]	333[8]	333.96	1832.7[2]			1499.35[10]	15.2[7]	
1836.9[2]	558.1[2]	100	-	-	1278.92	1836.9[2]	8^+	1837.03[10]	558.1[1]	100	-
1950.2[2]	1176.8[2]	100	1960[7]	783[7]	773.37	1950.2[2]	3^-	1952.46[3]	1176.6[13]	100[20]	8.6[9]
1962.9[7]	1222.4[7]	100	1948[28]	726[28]	740.46	1962.9[7]	$1^{(-)}$	1963.72[4]	1223.26[8]	100[7]	1.5[5]
2004.8[4]	811.2[6]	45[12]	2005[14]	1194[14]	1193.84	2005.0[6]	2^+	2005.5[8]	812.1[8]		7[1]
	2004.6[5]	100	2008[16]	3[16]	0	2004.6[5]					
2117.0[4]	1343.6[4]	100	2114[12]	770[12]	773.37	2117.0[4]	4^+	2117.030[15]	1343.78[22]	100[3]	4.9[7]
2152.7[4]	1379.3[4]	100	2157[17]	778[17]	773.37	2152.7[4]	4^+	2152.56[3]	1379.12[6]	100[12]	4.3[7]
2260.1[3]	1926.1[3]	100	2265[9]	339[9]	333.96	2260.1[3]	(1^-)	2259.94[4]	1926.04[8]	33[7]	11[1]
2362.6[2]	**1290.9**[3]	66[13]	2358[8]	1067[8]	1071.41	2362.3[3]					13[1]
	2028.9[3]	100	2373[12]	344[12]	333.96	2362.9[3]					
2587.2[4]	**1813.8**[4]	100	2602[24]	773[24]	773.37	2587.2[4]	$3^+, 4^+$	2587.3[5]			4.3[9]
2654.9[7]	**2320.9**[7]	100	2640[22]	319[22]	333.96	2654.9[6]	(3,5)	2655[7]			4.0[9]
2715.5[3]	**1521.7**[3]	100	2734[18]	1212[18]	1193.84	2715.5[3]	3^-	2715[4]			5.5[8]
3018.3[6]	**1852.5**[6]	100	3018[12]	1166[12]	1165.79	3018.3[6]					4.3[9]

Table 4.1 Continued:

E_x (keV)	E_γ (keV)	I_γ	E_x^t (keV)	E_x^t-E_γ (keV)	E_f^{ND}	E_γ+E_f^{ND} (keV)	$J^{\pi,ND}$	E_x^{ND}	E_γ^{ND}	I_γ^{ND}	$\sigma_{(34°-58°)}$ (% of 2_1^+)
3037.8^{9}	2702.9^{13} 3038.5^{12}	100 30^{8}	3042^{8} 3060^{18}	339^{8} 22^{18}	333.96 0	3036.9^{13} 3038.5^{12}	$1,2^+$	3038.2^{4}	2704.6^{7} 3037.8^{10}	100^{5} 33^{17}	40^{3}
3045.3^{15}	**2711.3**^{15}	100	3045^{9}	334^{9}	333.96	3045.3^{15}					38^{3}

Table 4.2: Levels and γ rays observed in the ^{154}Sm(p,t) reaction. Refer to the text for a full description of each column. The uncertainties are indicated by the superscript. Newly-identified levels and γ rays are shown in bold.

E_x (keV)	E_γ (keV)	I_γ	E_x^t (keV)	E_x^t-E_γ (keV)	E_f^{ND}	E_γ+E_f^{ND} (keV)	$J^{\pi,ND}$	E_x^{ND}	E_γ^{ND}	I_γ^{ND}	$\sigma_{(34°-58°)}$ (% of 2_1^+)
121.7^{2}	121.7^{2}	100	115^{8}	-7^{8}	0	121.7^{2}	2^+	121.7818^{3}	121.7817^{3}	100	100^{2}
366.2^{2}	244.4^{2}	100	364^{9}	119^{9}	121.78	366.2^{2}	4^+	366.4793^{9}	244.6974^{8}	100	8.0^{5}
685.2^{3}	563.4^{3}	100	681^{9}	118^{9}	121.78	685.2^{3}	0^+	684.751^{21}	562.98^{3}	100.0^{19}	95^{2}
706.7^{3}	340.2^{3}	100	704^{8}	364^{8}	366.48	706.7^{3}	6^+	706.928^{17}	340.45^{3}	100	6.5^{5}
810.6^{2}	443.7^{5}	36^{3}	812^{7}	368^{7}	366.48	810.2^{5}	2^+	810.453^{5}	444.00^{3}	34.8^{13}	47^{2}
	688.8^{2}	100	817^{8}	128^{8}	121.78	810.6^{3}			688.670^{5}	100.0^{6}	
	810.7^{4}	46^{4}	799^{7}	-12^{7}	0	810.7^{4}			810.451^{5}	37.0^{3}	
963.3^{3}	841.5^{2}	100	-	-	121.78	963.3^{3}	1^-	963.358^{5}	841.570^{5}	100.0^{18}	-
1023.1^{3}	656.5^{3}	100	1025^{12}	369^{12}	366.48	1023.0^{3}	4^+	1022.970^{5}	656.489^{5}	100.0^{15}	5.0^{7}
	901.6^{5}	69^{16}	1039^{14}	137^{14}	121.78	1023.4^{5}			901.19^{5}	59.2^{17}	
1041.2^{2}	674.7^{4}	27^{5}	1036^{12}	361^{12}	366.48	1041.1^{4}	3^-	1041.122^{4}	674.65^{3}	40.4^{8}	13^{1}
	919.5^{3}	100	1031^{8}	112^{8}	121.78	1041.3^{3}			919.337^{4}	100.0^{10}	
1085.6^{2}	963.7^{3}	100	1082^{8}	118^{8}	121.78	1085.5^{3}	2^+	1085.841^{5}	964.057^{5}	100.00^{24}	42^{2}
	1085.7^{3}	57^{5}	1089^{9}	3^{9}	0	1085.7^{3}			1085.837^{10}	69.71^{10}	

Table 4.2 Continued:

E_x (keV)	E_γ (keV)	I_γ	E_x^t (keV)	E_x^t-E_γ (keV)	E_f^{ND}	E_γ+E_f^{ND} (keV)	$J^{\pi,ND}$	E_x^{ND}	E_γ^{ND}	I_γ^{ND}	$\sigma_{(34°-58°)}$ (% of 2_1^+)
1125.3[3]	418.4[3]	100	-	-	706.93	1125.3[3]	8^+	1125.39[3]	418.45[3]	100	-
1221.6[3]	855.1[3]	100	1214[11]	359[11]	366.48	1221.6[3]	5^-	1221.64[3]	855.21[7]	100[3]	3.5[5]
1233.9[2]	867.9[4]	46[8]	-	-	366.48	1234.4[4]	3^+	1233.863[3]	867.380[3]	30.93[18]	-
	1112.0[2]	100	-	-	121.78	1233.8[2]			1112.076[3]	100.0[5]	
1293.0[14]	926.5[14]	100	1276[15]	350[15]	366.48	1293.0[14]	2^+	1292.773[10]	926.29[4]	100.0[12]	2.2[5]
1310.5[3]	603.6[3]	100	-	-	706.93	1310.5[3]	6^+	1310.505[22]	603.56[3]	100[4]	-
1371.7[3]	1005.2[6]	100	1393[22]	388[22]	366.48	1371.7[3]	4^+	1371.735[12]	1005.27[5]	100.0[16]	3.2[5]
1505.9[3]	799.0[3]	100	-	-	706.93	1505.9[3]	7^-	1505.77[3]	798.82[3]	100[3]	-
1510.9[4]	1389.1[4]	100	1542[20]	153[20]	121.78	1510.9[4]	1^-	1510.790[25]	1389.03[4]	100.0[21]	1.6[5]
1559.6[3]	1193.1[3]	100	-	-	366.48	1559.6[3]	5^+	1559.62[3]	1193.10[5]	100[3]	-
1579.4[2]	1212.9[2]	100	1577[9]	364[9]	366.48	1579.4[2]	3^-	1579.429[11]	1212.948[11]	100.0[4]	8[1]
	1457.4[4]	42[10]	1574[18]	117[18]	121.78	1579.2[4]			1457.643[11]	35.13[26]	
1609.0[4]	483.6[4]	100	-	-	1125.39	1609.0[4]	10^+	1609.26[4]	483.86[3]	100	-
1613.8[4]	906.9[4]	100	1618[16]	711[16]	706.93	1613.8[4]	4^+	1612.90[4]	906.06[10]	100[5]	1.4[4]
1659.8[3]	696.4[3]	100	1680[12]	984[12]	963.36	1659.8[3]	0^+	1658.80[25]	695.9[3]	100[5]	7[1]
1728.2[5]	1021.3[5]	100	-	-	706.93	1728.2[5]	6^+	1728.27[3]	1021.41[4]	100[3]	-
1755.1[2]	791.7[2]	100	1772[12]	980[12]	963.36	1755.1[2]	0^+	1754.98[4]	791.67[7]	100[5]	9.8[8]

Table 4.2 Continued:

E_x (keV)	E_γ (keV)	I_γ	E_x^t (keV)	E_x^t-E_γ (keV)	E_f^{ND}	E_γ+E_f^{ND} (keV)	$J^{\pi,ND}$	E_x^{ND}	E_γ^{ND}	I_γ^{ND}	$\sigma_{(34°-58°)}$ (% of 2_1^+)
1764.3^{3}	1057.2^{5}	68^{20}	1764^{19}	707^{19}	706.93	1764.1^{5}	5^-	1764.32^{5}	1057.36^{6}	100^{6}	3.2^{7}
	1398.0^{4}	100	1775^{18}	377^{18}	366.48	1764.5^{4}			1397.88^{7}	82^{5}	
1769.0^{1}	397.5^{5}	5^{2}	-	-	1371.74	1769.2^{5}	2^+	1769.132^{23}	397.75^{26}	1.9^{3}	141^{5}
	535.2^{3}	12^{2}	1796^{8}	1261^{8}	1233.86	1769.1^{3}			535.44^{12}	8.8^{7}	
	683.9^{8}	25^{3}	-	-	1085.84	1769.7^{8}			683.25^{9}	24.1^{14}	
	728.3^{5}	58^{6}	1773^{4}	1045^{4}	1041.12	1769.4^{5}			728.03^{4}	56.5^{19}	
	805.5^{6}	68^{6}	1760^{8}	955^{8}	963.36	1768.9^{6}			805.71^{9}	77^{3}	
	958.5^{3}	100	1777^{4}	819^{4}	810.45	1769.0^{3}			958.63^{5}	100^{6}	
	1084.5^{2}	79^{6}	-	-	684.75	1769.3^{2}			1084.36^{14}	54^{4}	
	1646.7^{3}	36^{5}	1781^{9}	134^{9}	121.78	1768.5^{3}			1647.44^{12}	36.9^{18}	
	1768.9^{2}	68^{8}	1779^{8}	10^{8}	0	1768.9^{2}			1769.09^{5}	47.3^{11}	
1879.5^{3}	754.1^{3}	100	-	-	1125.39	1879.5^{3}	9^-	1879.14^{4}	753.83^{3}	100^{3}	-
1891.9^{4}	928.5^{4}	100	1899^{5}	971^{5}	963.36	1891.9^{4}	0^+,1,2	1892.48^{5}	929.12^{5}	100^{10}	21^{1}
1906.0^{2}	821.6^{11}	27^{12}	1910^{12}	1088^{12}	1085.84	1907.4^{11}	2^+	1906.13^{3}	820.31^{7}		29^{2}
	942.4^{3}	51^{12}	1890^{10}	948^{10}	963.36	1905.8^{3}			942.85^{6}	8.5^{12}	
	1784.5^{3}	100	1923^{13}	139^{13}	121.78	1906.3^{3}			1784.27^{7}	100^{8}	
	1905.9^{3}	96^{20}	1911^{10}	5^{10}	0	1905.9^{3}			1906.14^{7}		
1954.5^{7}	913.4^{7}	100	1940^{12}	1027^{12}	1041.12	1954.5^{7}	3^-,4,5^-	1954.30^{5}	913.17^{6}	100^{5}	2.8^{5}
2003.5^{6}	**1296.6**^{6}	100	2010^{20}	713^{20}	706.93	2003.5^{6}					2.3^{5}

Table 4.2 Continued:

E_x (keV)	E_γ (keV)	I_γ	E_x^t (keV)	E_x^t-E_γ (keV)	E_f^{ND}	E_γ+E_f^{ND} (keV)	$J^{\pi,ND}$	E_x^{ND}	E_γ^{ND}	I_γ^{ND}	$\sigma_{(34°-58°)}$ (% of 2_1^+)
2011.1[3]	1644.6[3] 1889.4[6]	70[10] 100	2022[10] 2010[10]	377[10] 121[10]	366.48 121.78	2011.1[3] 2011.2[6]	2^+,3,4^+	2011.84[5]	1645.30[10] 1889.95[6]	100[9] 50[9]	19[2]
2091.1[2]	1050.1[3] 1127.6[3]	99[29] 100	2092[10] 2095[11]	1042[10] 967[11]	1041.12 963.36	2091.2[3] 2091.0[3]	1^-, 2	2091.21[4]	1050.10[5] 1127.84[5]	100[7] 82[7]	8[1]
2138.0[2]	1096.9[2]	100	2138[11]	1041[11]	1041.12	2138.0[2]	2^+	2138.17[12]	1096.96[12]	100[4]	7[2]
2138.5[8]	2016.7[8]	100	2120[40]	103[40]	121.78	2138.5[8]	(2^+,3,4^+)	2137.92[6]	2016.17[7]		2.3[7]
2214.9[8]	**2093.1**[8]	100	2202[26]	109[26]	121.78	2214.9[8]					6[1]
2246.1[2]	**1160.3**[3] **1163.3**[4] **2245.8**[8]	100 77[24] 41[12]	2249[6] 2245[8] 2234[24]	1089[6] 1082[8] -15[24]	1085.84 1082.84 0	2246.1[3] 2246.1[4] 2245.8[8]					24[2]
2247.0[2]	**1283.9**[4] **2125.1**[3]	100 95[28]	2249[8] 2262[18]	965[8] 137[18]	963.36 121.78	2247.3[4] 2246.9[3]					14[1]
2285.2[3]	1321.8[3]	100	2296[30]	974[30]	963.36	2285.2[3]	0,1,2	2284.96[20]	1321.6[2]		6.3[8]
2320.5[2]	516.9[3] 1613.2[4] 1953.8[3]	100 9[3] 29[5]	2323[9] 2288[19] 2324[10]	1806[9] 675[19] 370[10]	1803.94 706.93 366.48	2320.8[3] 2320.1[4] 2320.3[3]	4^+, 5	2320.35[23]	516.3[4] 1613.4[6] 1953.7[4]	100[10] 13[3] 30[7]	47[3]
2331.1[4]	**1624.2**[4]	100	2348[18]	724[18]	706.93	2331.1[4]					6.4[9]
2365.4[3]	**1998.9**[3]	100	2369[13]	370[13]	366.48	2365.4[3]					8[1]

Table 4.2 Continued:

E_x (keV)	E_γ (keV)	I_γ	E_x^t (keV)	E_x^t-E_γ (keV)	E_f^{ND}	E_γ+E_f^{ND} (keV)	$J^{\pi,ND}$	E_x^{ND}	E_γ^{ND}	I_γ^{ND}	$\sigma_{(34°-58°)}$ (% of 2_1^+)
2462.7[5]	**1499.3**[5]	100	2456[12]	957[12]	963.36	2462.7[5]					3.5[6]
2567.8[7]	2201.3[7]	100	2566[20]	365[20]	366.48	2567.8[7]	4^+,5	2567.06[17]	2200.7[2]	100[17]	3.1[9]
2705.0[8]	**2583.2**[8]	100	2702[11]	119[11]	121.78	2705.0[8]					5[1]
3039.1[8]	**2917.3**[8]	100	3038[18]	121[18]	121.78	3039.1[8]					7[2]
3132.0[5]	**2765.5**[5]	100	3134[12]	369[12]	366.48	3132.0[5]					9[3]

4.4 Levels and γ-ray transitions in ^{150}Sm

The level at 1603.1(7) keV

A 1269.1(7)-keV γ ray was placed between the level at 1603.1(7) keV and the first 2^+ state. It is likely that this is the level observed by Debenham [19] at an excitation energy of 1603(4) keV in the (p,t) reaction. The cross section for the direct population of this level was measured by Debenham to be 0.48% of that of the 0_2^+ level where both measurements were obtained at a laboratory angle of 25 degrees. This compares well with the value of 0.39(14)% from the present work. However, it must be noted that here we quote the relative cross section integrated across the angular range of the telescope. Additionally, Debenham utilised a lower beam energy of 19 MeV which could significantly affect the measured cross sections.

The level at 1794.2(2) keV

In the NNDC database, a level at 1794.30(3) keV is assigned four γ-ray transitions at energies of 151.64(4), 600.43(25), 722.65(18) and 1798(4) keV, where the 151.64(4) keV transition is a tentative assignment. The 1798(4)-keV γ ray was not observed in the present work, but should be seen in the spectrum if the relative intensity from the literature is correct. Therefore, it is likely that this transition does not belong to the 1794.2(2) keV level. The 151.64(4) keV γ was also not observed but would not be expected to be seen due to the low intensity. γ rays at energies of 628.5(3) keV and 1459.9(4) keV were observed in coincidence with triton peaks at energies of 1796(7) keV and 1764(16) keV respectively and can be assigned to this level. It is possible that the 628.5(3)-keV γ ray is the 628.56(14)-

keV transition previously observed in the (n,γ) reaction [57] but not placed in the level scheme. The 628.5(3) keV transition feeds the 1^- level at 1165.6(2) keV and the 1459.9(4) keV transition populates the 2_1^+ state. These new placements are consistent with the previous spin and parity assignment of 2^+ for the level.

The level at 1826.7(3) keV

A new level is placed at 1826.7(3) keV with a 1053.3(3)-keV transition to the 4_1^+ state at 773.374(12) keV. The γ ray is in prompt-coincidence with a triton peak at 1824(8) keV. If this transition is a primary γ ray from the 1824(8) keV level then there is no other possible final level other than the 4^+ state within the experimental uncertainty. However, this placement cannot be confirmed using t-γ-γ coincidences due to insufficient statistics.

The level at 1832.8(2) keV

In the NNDC database, a $(2)^+$ level at 1833.01(3) keV is listed with four γ-ray transitions at 667.05(3), 788, 1499.35(10) and 1833.30(15) keV. In the present work, only γ rays at energies of 667.3(3) and 1498.7(2) keV are observed, which are the two most intense transitions. However, the 667.3(3) transition was observed to have 48(8)% of the intensity of the 1498.7(2) keV transition in the present work, whereas in the NNDC database the 667.05(3) keV γ ray is listed as the strongest transition. This discrepancy can be explained by the fact that the 667.05(3) keV transition is multiply placed in the NNDC database and the undivided intensity is given.

The level at 1950.2(2) keV

A 1176.8(2)-keV transition was observed from the level at 1950.2(2) keV to the 4^+ state at 773.3(3) keV. This γ ray is likely to correspond to the 1176.6(13) keV transition from the level at 1952.46(3) keV in the NNDC database. However, the NNDC database also assigns a 308.05(4)-keV γ ray to this level. The level energy calculated using the 308.05(4)-keV γ ray is not consistent with the level energy measured in the present work, and therefore the 308.05(4) and 1176.6(13) keV γ rays are likely to belong to separate levels.

The level at 2004.8(4) keV

A level at 2004.8(4) keV was observed with a 811.2(6)-keV transition to the 2^+ state at 1193.9(2) keV and a new 2004.6(5) keV transition to the ground state. The 811.2(6)-keV γ ray may correspond to the 812.1(8)-keV transition previously observed in the β^- decay of ^{150}Pm [58], which was previously not placed in the level scheme.

The level at 2260.1(3) keV

A 1926.1(3)-keV transition to the 2_1^+ state was observed from a level at 2260.1(3) keV. A level at 2259.8(8) keV was previously reported by Barrette *et al.* [58] and tentatively assigned as a 1^- state. Eight γ-ray transitions were previously assigned to this level, including a transition at 1926.04(8) keV which corresponds to the γ ray measured in the present work. Based on our nonobservation of the remaining transitions, it is probable that there are multiple discrete states close to 2260 keV, of which only the level at 2260.1(3) keV is observed in the present work.

The level at 2362.6(2) keV

Two γ-ray transitions at energies of 1290.9(3) and 2028.9(3) keV are assigned to a new level at 2362.6(2) keV. In Figure 4.6, the triton energy spectra in coincidence with these two γ rays are shown. The level energy obtained by summing the γ-ray energies with the energies of the levels that are being fed is indicated by the blue dashed line.

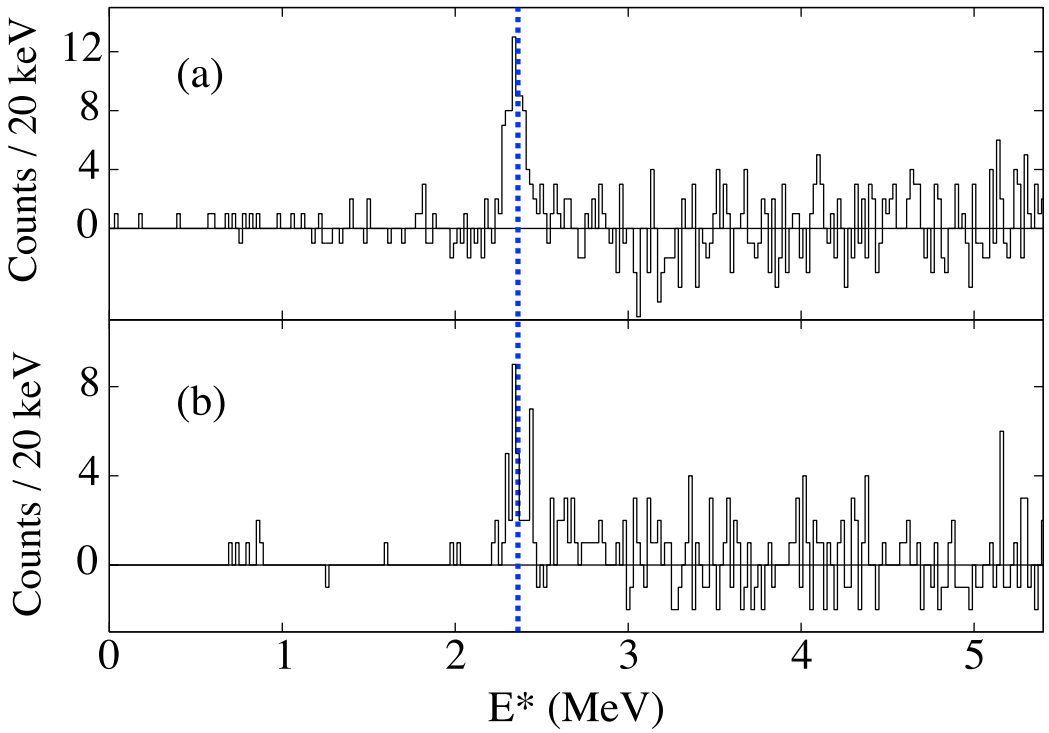

Figure 4.6: Triton energy spectra in coincidence with the (a) 1290.9(3) and (b) 2028.9(3) keV transitions from the level at 2362.6(2) keV in ^{150}Sm. The blue dashed line indicates the weighted average of 2362.6(2) keV obtained by summing the γ-ray energies with the NNDC energies of the levels that are fed.

The level at 2587.2(4) keV

A new 1813.8(4)-keV transition is placed between a level at 2587.2(4) keV and the 4_1^+ state. This level energy is consistent with the previous value of 2587.3(5) keV [59,60]. The level was previously assigned as a 3^+,4^+ state. It is therefore probable that this level is a 4^+ state based on the natural-parity selection rule of the (p,t) reaction. This is consistent with the new transition to the lower-lying 4^+ state observed in the present work.

The level at 2654.9(7) keV

A level at 2654.9(7) keV is observed with a 2320.9(7) keV γ-ray transition to the 2_1^+ state. This 2654.9(7)-keV level may be the previously reported level at 2655(7) keV [11,60–62], previously assigned as a $3^{(+)}$, $5^{(+)}$ level [62]. This suggests that the level is a 3^- state based on the natural-parity selection rule and the transition to the lower lying 2^+ state.

4.5 Levels and γ-ray transitions in ^{152}Sm

The level at 2003.5(6) keV

A 1296.6(6)-keV transition from a level at 2003.5(6) keV is observed. It is possible that this state may correspond to one of three levels from the NNDC database at energies of 2003.66(20), 2004.24(6) and 2004.29(11) keV. The level at 2004.24(6) keV has a known γ-ray transition at 1297.4(10) keV which could correspond to the 1296.6(6)-keV transition from the present work. Similarly, the 2004.29(11)-keV level has a 1297.29(13)-keV transition.

The level at 2214.9(8) keV

A level at 2214.9(8) keV is observed with a new 2093.1(8)-keV transition. A level has previously been observed at an excitation energy of 2214.98(7) keV in the ^{150}Nd(α,2nγ) reaction [63]. However, this is not the same level observed in the present work, since the 8^+ assignment is not consistent with a decay to the 2_1^+ level.

The 2246.1(2) and 2247.0(2) keV levels

Three new γ-ray transitions at 1160.3(3), 1163.3(4) and 2245.8(8) keV were observed from a level at 2246.1(2) keV. Additionally, two further new γ rays at energies of 1283.9(4) and 2125.1(3) keV were assigned to a level at 2247.0(2) keV. Separate level assignments were made since the level energies evaluated using the 1283.9(4)- and 2125.1(3)-keV transitions lie 3.0 and 2.7 standard deviations, respectively, from the level energy evaluated using the remaining three γ rays. An unpublished level at 2247.23 keV has previously been observed [64] with transitions to the first excited 0^+, 2^+ and 1^- levels.

The level at 2331.1(4) keV

A level was observed at 2331.1(4) keV with a 1624.2(4)-keV transition to the 6_1^+ state. This is likely to be the unpublished level [64] at an excitation energy of 2332.42 keV populated in the (α,2nγ) reaction with transitions to the 6_1^+ and 8_1^+ levels.

The level at 2365.4(3) keV

A 1998.9(3)-keV γ ray was placed between a new level at 2365.4(3) keV and the 4_1^+ state. A level at 2365 keV has previously been observed [64] with 994- and 753-keV transitions to lower lying 4^+ states. However, this is unlikely to be the level populated in the present work since these transitions were not observed despite the higher γ-ray detection efficiency at those energies.

The level at 2462.7(5) keV

A level was observed at an excitation energy of 2462.7(5) keV with a 1499.3(5)-keV γ ray. An unpublished level at 2463.17 keV was previously observed [64] in the (n,n'γ) reaction with a transition to the first excited 1^- state, consistent with the assignment made in the present work.

4.6 Angular Distributions

The orbital angular-momentum transfer in the (p,t) reaction may be determined by comparing the experimental angular distributions of the outgoing tritons to distributions calculated using the Distorted Wave Born Approximation (DWBA) theory. In the present work, DWBA calculations were performed using the DWUCK4 code [47]. The optical-model parameters used in the calculations are listed in Table 2.1 and the potential was that from Reference [48], which is given by Equation 2.10.

The angular coverage of the STARS telescope was from 34 to 58 degrees. The position of the beam spot with respect to the centre of the telescope was calculated

as described in Section 3.2.4. The angle and solid angle for each pixel of the telescope was corrected in order to account for this offset.

4.6.1 Discrete States

In order to measure the angular distribution for a discrete state, gates were placed on both a γ-ray transition that directly depopulates the level, as well as the coincident triton peak corresponding to the direct population of the level. The intensity observed in each ring-sector pixel of the telescope was then corrected for the solid angle of that pixel and binned in 2 degree increments. For levels with multiple observed transitions, the angular distributions obtained from gating on each γ ray were summed.

In Figure 4.7, the experimental angular distributions for some low-lying levels in ^{150}Sm are compared to the calculated DWBA curves corresponding to the NNDC value of the spin of that level. The agreement between the experimental and theoretical distributions was good, and no discrepancies were found between the spins from the literature and a comparison of the experimental angular distributions to the corresponding DWBA curves.

In Figure 4.8, the experimental angular distribution for the level at 2320.5(2) keV in ^{152}Sm is compared to the DWBA calculations for $L = 4$ (dashed blue line) and $L = 5$ (red line) transfer. This level was previously assigned as a $J^\pi = 4^+, 5$ state based on its four observed γ-ray transitions to two 4^+ states at 1022.970(5) and 366.4793(9) keV, the 5^- state at 1803.94(5) keV and the 6^+ state at 706.928(17) keV. The reduced χ^2 for the $L = 4$ DWBA curve was 2.1 and for the $L = 5$ calculation was 2.2. Therefore, the statistics in the current work do not allow for a definitive

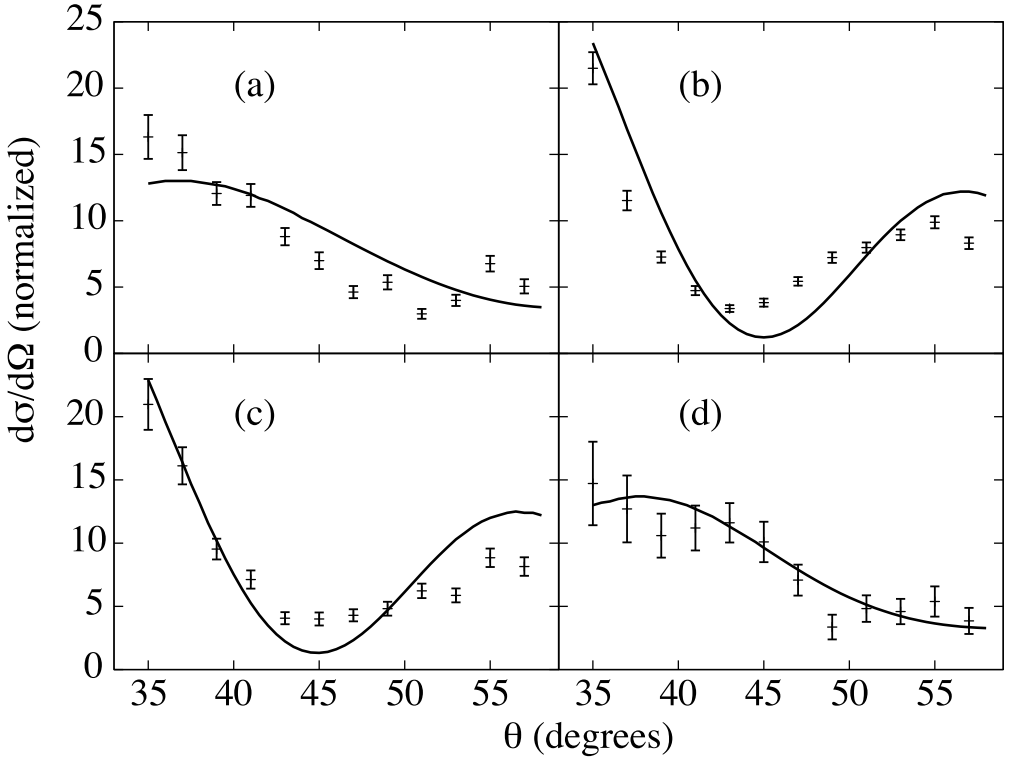

Figure 4.7: The experimental angular distributions for the levels in ^{150}Sm at (a) 334 keV, $J = 2$ (b) 740 keV, $J = 0$ (c) 1256 keV, $J = 0$ and (d) 1417 keV, $J = 2$ are compared to the DWBA calculations for the respective L transfer.

assignment of the spin.

For the levels that were newly identified in the present work, there were insufficient statistics for spin assignments by comparison to DWBA curves.

4.6.2 Peak-like Structures

The angular distributions for the peak-like structures observed at intermediate excitation energy were obtained by measuring the number of counts above a smooth continuum background for each ring-sector pixel of the Si telescope. The area assumed to belong to the PLS is indicated by the shaded blue area in Figure 4.9. The

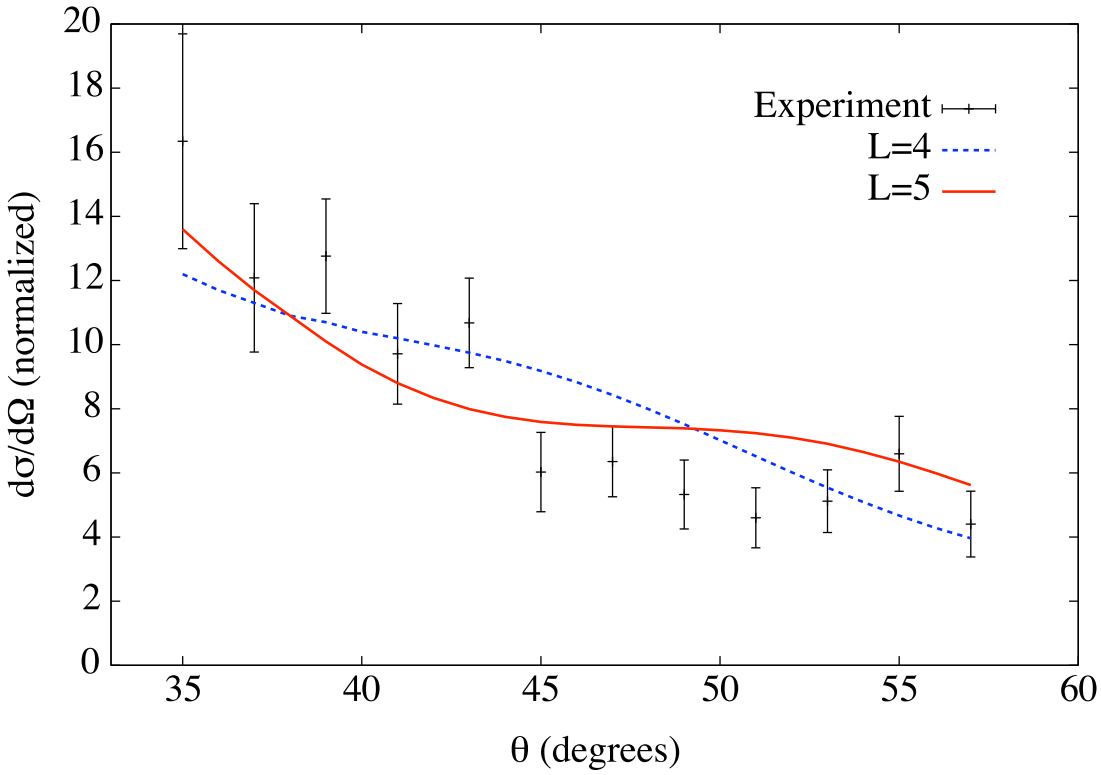

Figure 4.8: The experimental angular distribution for the level at 2320.5(2) keV in ^{152}Sm (black points) is compared to the DWBA calculations for $L = 4$ (dashed blue line) and $L = 5$ (red line) transfer.

angular distributions for the background under the PLS were obtained by measuring the number of counts below the shaded blue area for each pixel. In Panel (a) of Figure 4.10 the experimental angular distribution of the PLS in ^{150}Sm (black points) is compared to the angular distribution for the background under the PLS (red points) and to the distribution from the continuum region between 3.3 and 4.0 MeV (blue points). In Panel (b) of the figure, the angular distribution of the PLS in ^{152}Sm (black points) is compared to the distribution for the background under the PLS (red points) and the distribution from the continuum region between 2.5 and 3.0 MeV (blue points). In both reactions, the angular distributions

for the background under the PLS and the adjacent continuum region are very similar, and significantly different to the angular distribution from the PLS itself, indicating a difference in the L-transfer distribution. The similarity between the curves corresponding to the background under the PLS and the continuum region is evidence that the area chosen to correspond to the PLS, shown in Figure 4.9, is approximately correct. In Panel (c) of the figure, the angular distributions from the PLS in ^{150}Sm and ^{152}Sm are compared. It can be seen that these distributions are remarkably similar, despite the PLS in these nuclei being 700 keV apart in excitation energy. This suggests that the L-transfer distribution when populating the PLS is very similar in both reactions. In Panel (d), the angular distributions of the PLS from Panel (c) are compared to the DWBA calculations for $L = 2, 3$ and 4, the three curves most similar to the experimental data. These DWBA curves were calculated for the case of the ^{152}Sm(p,t) reaction.

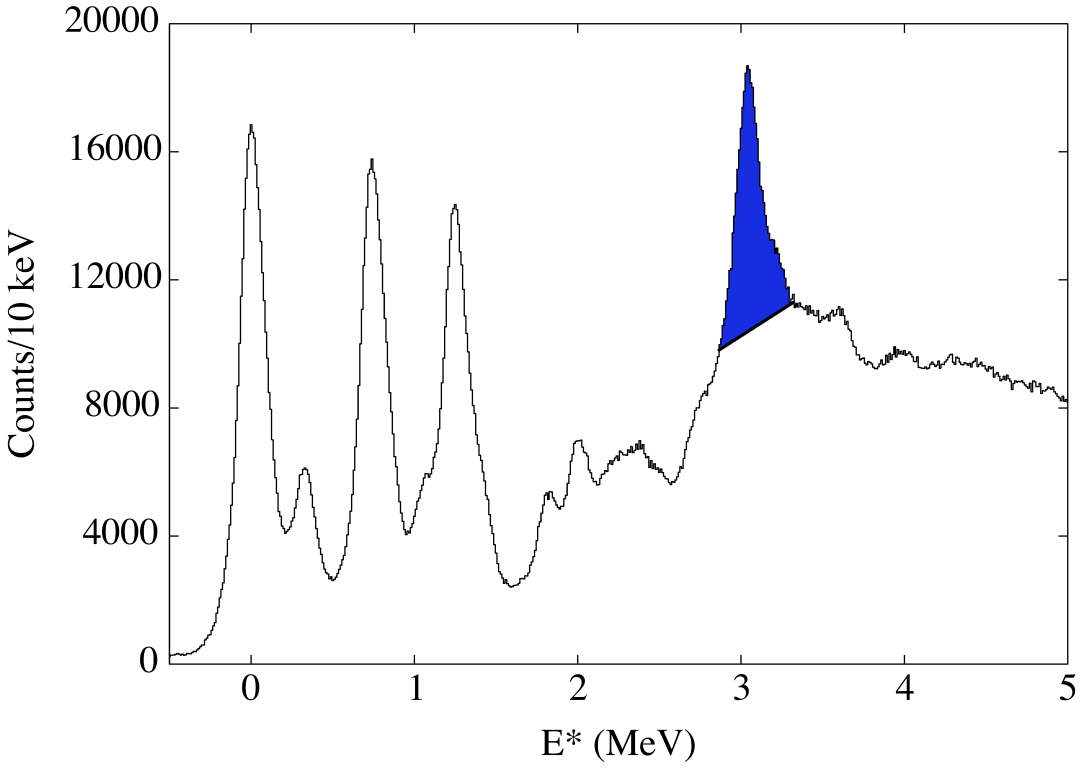

Figure 4.9: Triton singles spectrum from the ^{152}Sm(p,t) reaction where the area used to calculate the angular distribution of the PLS is shaded in blue.

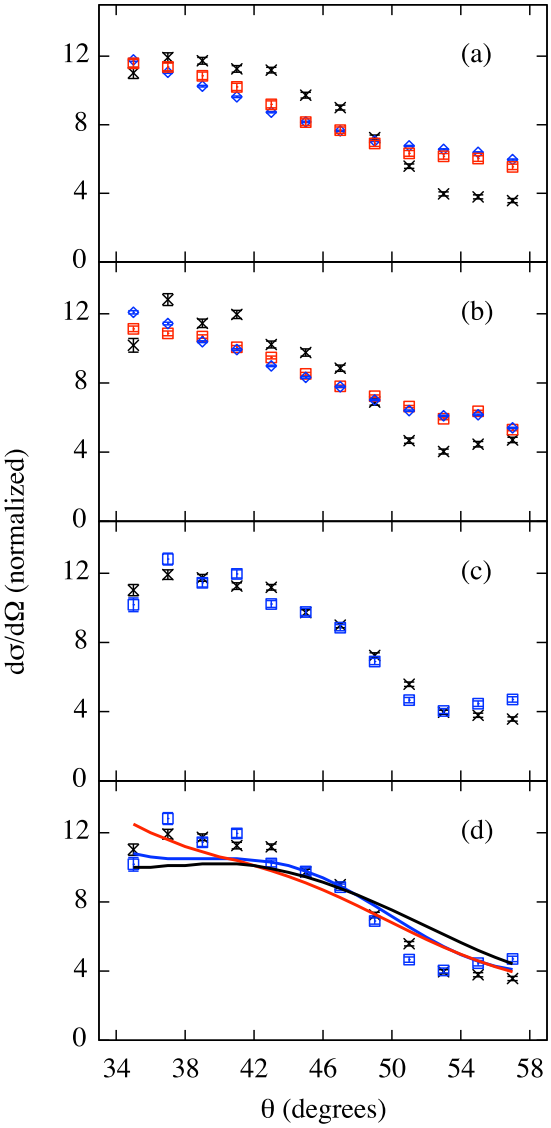

Figure 4.10: In Panel (a) the angular distribution of the PLS in ^{150}Sm (black points) is compared to the angular distribution of the background under the PLS (blue points) and the distribution from the nearby continuum region between 3.3 and 4.0 MeV (red points). In Panel (b) the same distributions but for ^{152}Sm are plotted, when the continuum region was between 2.5 and 3.0 MeV. In Panel (c) the angular distributions from the PLS in ^{150}Sm (black points) and ^{152}Sm (blue points) are compared. In panel (d) the distributions from panel (c) are compared to the DWBA curves for $L = 2$ (blue), $L = 3$ (black) and $L = 4$ (red) transfer, calculated for the ^{152}Sm(p,t) reaction.

4.7 Cross Sections

In order to measure the relative partial cross section for the direct population of a level, a primary γ ray from the level is gated on, producing a triton energy spectrum where the lowest energy peak corresponds to the direct population of the level, in the absence of any contamination. The area of the direct population peak is measured and corrected for the γ-ray detection efficiency and the internal conversion coefficient of the γ-ray transition. The internal conversion coefficients from the NNDC database [35] were used. These relative cross sections are angle averaged over the range of the telescope from 34 to 58 degrees. The missing strength due to unobserved γ-rays was not corrected for, and therefore the values listed in Tables 4.1 and 4.2 should be considered lower limits of the cross sections. In Figures 4.11 and 4.12 the relative partial cross sections from Tables 4.1 and 4.2 are compared to the triton projections from the corresponding triton-γ matrices. It can be seen in these figures that the correspondence between the two is good for both reactions. In the ^{150}Sm spectrum at approximately 3 MeV, the group of three relatively strongly populated states in the region of the PLS stand out in particular.

In Table 4.3, the relative cross sections from the present work for the ^{152}Sm(p,t) reaction are compared to those from Debenham *et al.* [19] and McLatchie *et al.* [18]. This data is provided as a general comparison only, since the cross sections quoted by Debenham are the maximum differential cross section at the listed angle, as opposed to the angle-averaged cross sections measured in the present work. The values from reference [18] are given for a laboratory angle of 22.5 degrees. In the work by Debenham, a lower incident proton energy of 19 MeV

was used. Additionally, the values obtained in the present work will be lower if there are unobserved γ-ray transitions. It can be seen from the table that the agreement between the three sets of data is good in general. Of particular note are the large cross sections for the population of the excited 0^+ states at 740.6(2) and 1255.4(1) keV, which has previously been interpreted in terms of shape coexistence [10, 26].

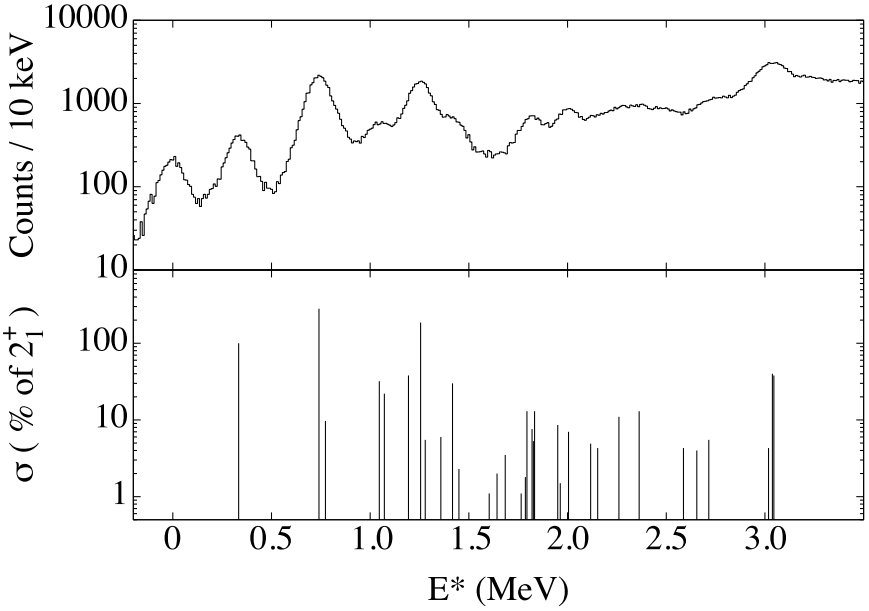

Figure 4.11: In the top half of the figure the triton projection of the triton-γ matrix from the ^{152}Sm(p,t) reaction is shown. In the bottom half of the figure the relative partial cross sections from Table 4.1 are plotted.

Table 4.3: The relative partial cross sections for states in ^{150}Sm are compared to those from Debenham [19] and McLatchie [18]. All cross sections are relative to that for the 2_1^+ level, which has been scaled to 100. The values from Debenham are the maximum differential cross sections at the angle listed in the following column, with a relative error of 6.9%.

E_x (keV)	J^π	$\sigma(34^\circ - 58^\circ)$ Present work	$\sigma(\theta)_{max}$ Reference [19]	θ (degrees)	$\sigma(22.5^\circ)$ Reference [18]
333.7(2)	2^+	100(2)	100	10	100
740.6(2)	0^+	282(6)	260	25	340
773.3(3)	4^+	9.7(8)	9.9	10	<20
1046.3(2)	2^+	32(2)	42	10	<20
1071.7(2)	3^-	22(2)	5.6	35	40
1193.9(2)	2^+	38(2)	46	10	80
1255.4(1)	0^+	186(4)	170	25	180
1357.9(4)	5^-	6(1)	1.9	20	<20
1417.2(2)	2^+	30(2)	27	10	30
1449.7(4)	4^+	2.3(6)	3.7	12.5	<20
1603.1(7)		1.1(4)	1.2	25	
1642.6(7)	4^+	2.0(5)	1.2	10	
1794.2(2)	2^+	13(1)	17	10	
1832.8(2)	$(2)^+$	7.6(9)	6.8	20	<20
1950.2(2)	3^-	8.6(9)	3.7	35	<20

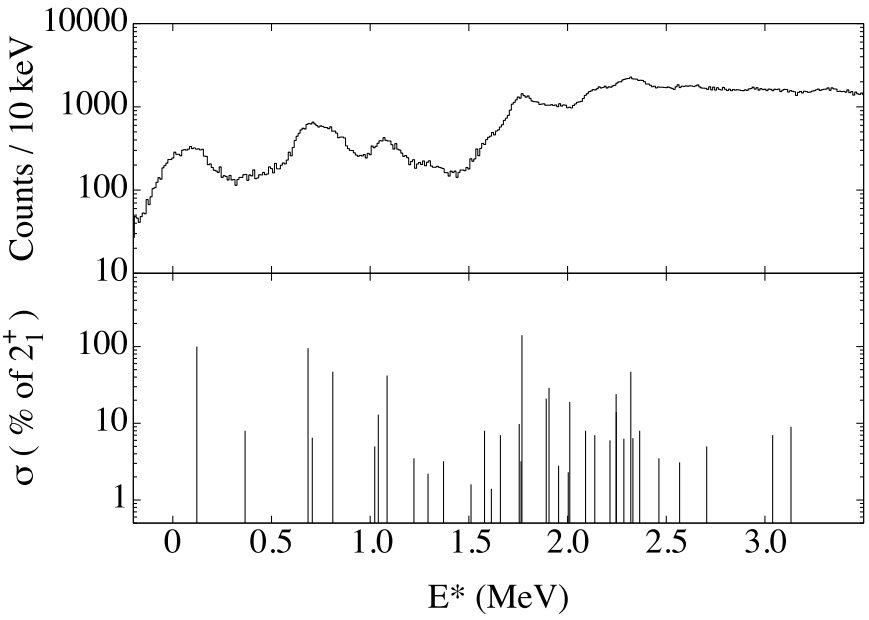

Figure 4.12: Same as Figure 4.11 but for the ^{154}Sm(p,t) reaction.

4.8 Peak-Like Structures

A prominent feature of the triton projections shown in Figure 4.2 is the narrow peak-like structure (PLS) that can be seen at intermediate excitation energy, in between the region of strongly populated discrete states at low excitation energy and the smooth continuum region at high excitation energy, in all of the reactions shown. The excitation energy of the PLS is plotted as a function of neutron number in Figure 4.13. The energy of the structure is very similar for the isotopes with the same neutron number, and appears to decrease with increasing neutron number.

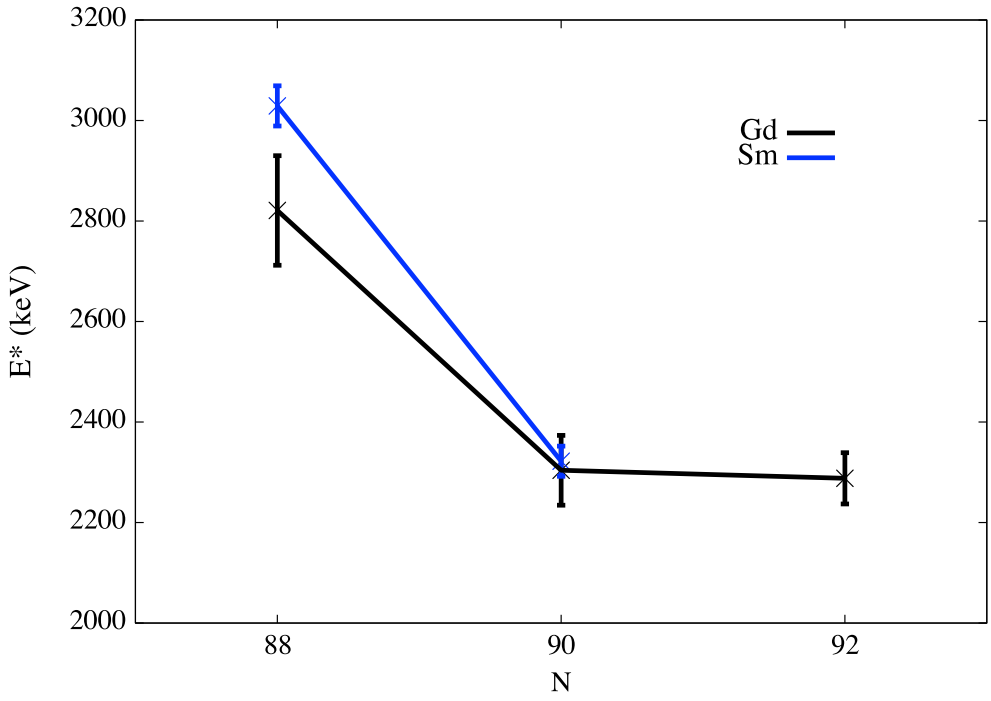

Figure 4.13: The excitation energy of the PLS as a function of neutron number for the Sm (blue) and Gd(black) isotopes.

In Figures 4.14 and 4.15 partial level schemes of ^{150}Sm and ^{152}Sm respectively are shown, where only levels directly populated in the region of the PLS are plotted.

The region of the PLS is indicated by the dashed black lines. Newly observed levels and γ-ray transitions are shown in red. It is particularly apparent from these figures that a significantly larger number of states was observed in the region of the PLS in ^{152}Sm than in ^{150}Sm. A total of eight levels were identified in the region of the PLS in ^{152}Sm, six of which are newly observed. This compares to only three levels observed in the region of the PLS in ^{150}Sm, two of which are new levels. One reason for this difference between the two nuclei is that many of the levels in the region of the PLS were identified using high energy γ-ray transitions to either the ground state, or to the first or second excited states. This is due to the fact that higher energy γ rays are easier to place in the level scheme, since it is more likely that there is only one possible final level within the experimental uncertainty. Therefore, the 700 keV difference in the energy of the PLS in the two nuclei results in a significantly better γ-ray detection efficiency for identifying levels in the region of the PLS in ^{152}Sm than for ^{150}Sm.

The cross section for the population of the PLS in ^{150}Sm, within the angular range of the telescope and measured in the triton singles spectrum, was measured to be 213(20)% of the cross section for the direct population of the first excited 2^+ state at 333.7(2) keV. The cross section for the population of the PLS in ^{152}Sm was measured to be 117(19)% of the cross section for the 2_1^+ level at 121.7(2) keV. For ^{150}Sm, 39(4)% of the strength of the PLS can be accounted for by the observed discrete states. This compares to a value of 93(15)% for ^{152}Sm, where a value greater than 100% would be possible if background chosen under the PLS is incorrect, or if not all the levels identified in the region belong to the PLS. It is useful to compare these results to those from the high-resolution (triton energy) study by Saha *et al.* [20]. The triton energy spectra from the ^{148,150,152,154}Sm(p,t) reactions

from that paper are shown in Figure 4.16. For ^{150}Sm, the PLS lies outside of the energy range measured by Saha. For the case of ^{152}Sm it can be seen that the region of the PLS is dominated by a relatively small number of strongly populated discrete states built upon a continuum background, which is consistent with the results obtained in the present work. The very strongly populated state measured at an excitation energy of 2268 keV by Saha corresponds to the levels at 2246.1(2) and 2247.0(2) keV in the present work, with cross sections of 24(2)% and 14(1)% relative to the 2_1^+ state, respectively. The difference in excitation energy between 2268 keV and the energies from the present work is due to the fact that the level energies reported by Saha are systematically too high.

In the study of the ^{148,150,152,154}Sm(p,t) reactions by Struble *et al.* [21] a large, broad enhancement of strength at approximately 6 MeV in excitation energy was observed. Additionally, a much narrower structure between 2.2 to 3.1 MeV in excitation energy was observed in the ^{152,154}Sm reactions, which corresponds to the PLS observed in the present work. In the study by Crawley *et al.* [30], broad structures were observed between 7-9 MeV excitation energy in the triton energy spectra from the ^{112,116,118,120,122,124}Sn(p,t) reactions. It was initially suggested that these structures were composed of states formed by coupling two deep-lying neutron holes from below the major shell closure [65]. The broad structure in ^{114}Sn has also been observed in the ^{116}Sn(α,^{6}He) reaction [66], and a similar structure at approximately 5 MeV excitation energy was observed in the single-neutron transfer reactions ^{112,116,118,120,122,124}Sn(d,t) [67]. In the paper by Broglia and Bes [68], pairing vibrations formed by the transfer of pairs of particles across major shells are described. However, it was shown by Nomura [31] that the energy systematics of the bumps are better described by coupling a neutron hole from

near the Fermi surface to a deep-lying neutron hole. The formation of resonance-like structures superimposed upon a continuum background by the fragmentation of single-particle hole states has been discussed in detail by Galés, Stoyanov and Vdovin [69], references [70] and [71] where two-hole states are also discussed, and by Soloviev [72].

A wide range of nuclei from ^{66}Zn to ^{230}Th were studied using the (p,t) reaction by Nakagawa *et al.* [32] where bumps at low and high excitation energy were observed. The excitation energies of those bumps are plotted in Figure 4.17, where it can be seen that the energies are smoothly varying excepted for abrupt jumps at the major shell closures. The bumps at lower excitation energy were found to be in good agreement with the excitation energy predicted by coupling a valence hole to a deep-lying hole using the pairing model. However, the bumps at higher excitation energy were found to be in poor agreement with the energy predicted by coupling two deep-lying neutron holes. It is important to note that the width (FWHM) of these structures measured by Nakagawa in the N=82 region was approximately 5 MeV. This is much larger than the width of the PLS observed in the present work. In the ^{150}Sm(p,t) reaction, the bump possibly corresponding to the deep-deep neutron hole excitation was measured at an energy of approximately 6 MeV by Nakagawa, in agreement with the measurement by Struble [21]. The bump corresponding to the valence-hole deep-hole excitation would be expected to lie at a lower excitation energy. In Figure 4.17 it can be seen that the excitation energy of the bumps decreases with increasing neutron number above $N = 82$, consistent with the energy systematics of the PLS observed in the present work.

If the PLS consists mainly of states formed by the coupling of a valence hole to a deep-lying hole, then the energy of the structure should depend on the size

of the shell gap. It was suggested by Struble [21] that the PLS is associated with two-hole strength in strongly upsloping orbitals from below the N=82 closure. If this is the case, then the energy of the structure should be strongly affected by the rapid onset of deformation in the region. It can be seen in Figure 4.13 that the energy of the PLS drops sharply with the onset of deformation between $N = 88$ and $N = 90$, and then remains relatively constant between $N = 90$ and $N = 92$.

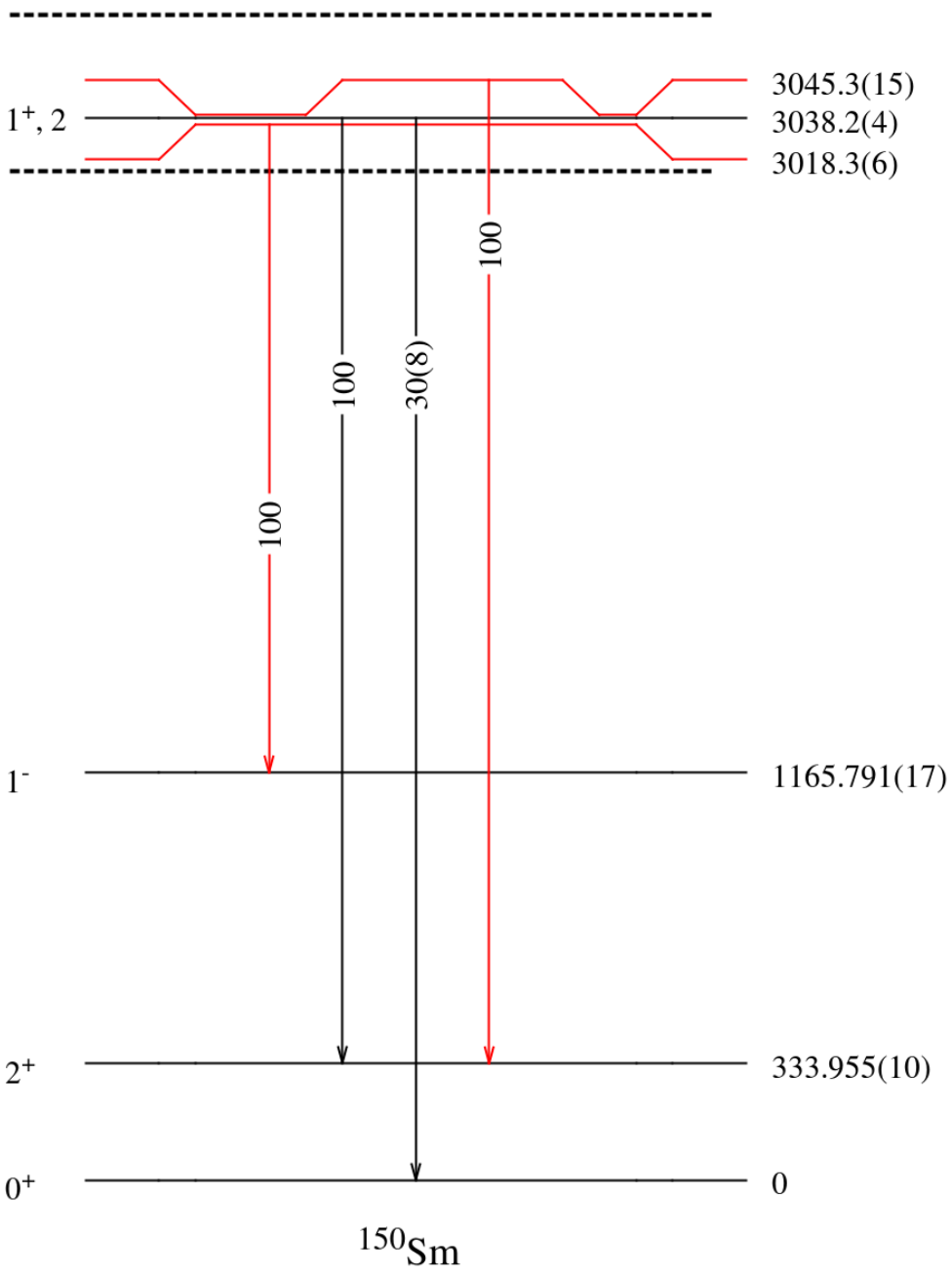

Figure 4.14: Partial level scheme of ^{150}Sm showing levels directly populated in the region of the PLS, indicated by the dashed lines. New levels and γ rays are plotted in red. The relative γ-ray branching for each level, expressed as a percentage of the strongest transition, is also indicated.

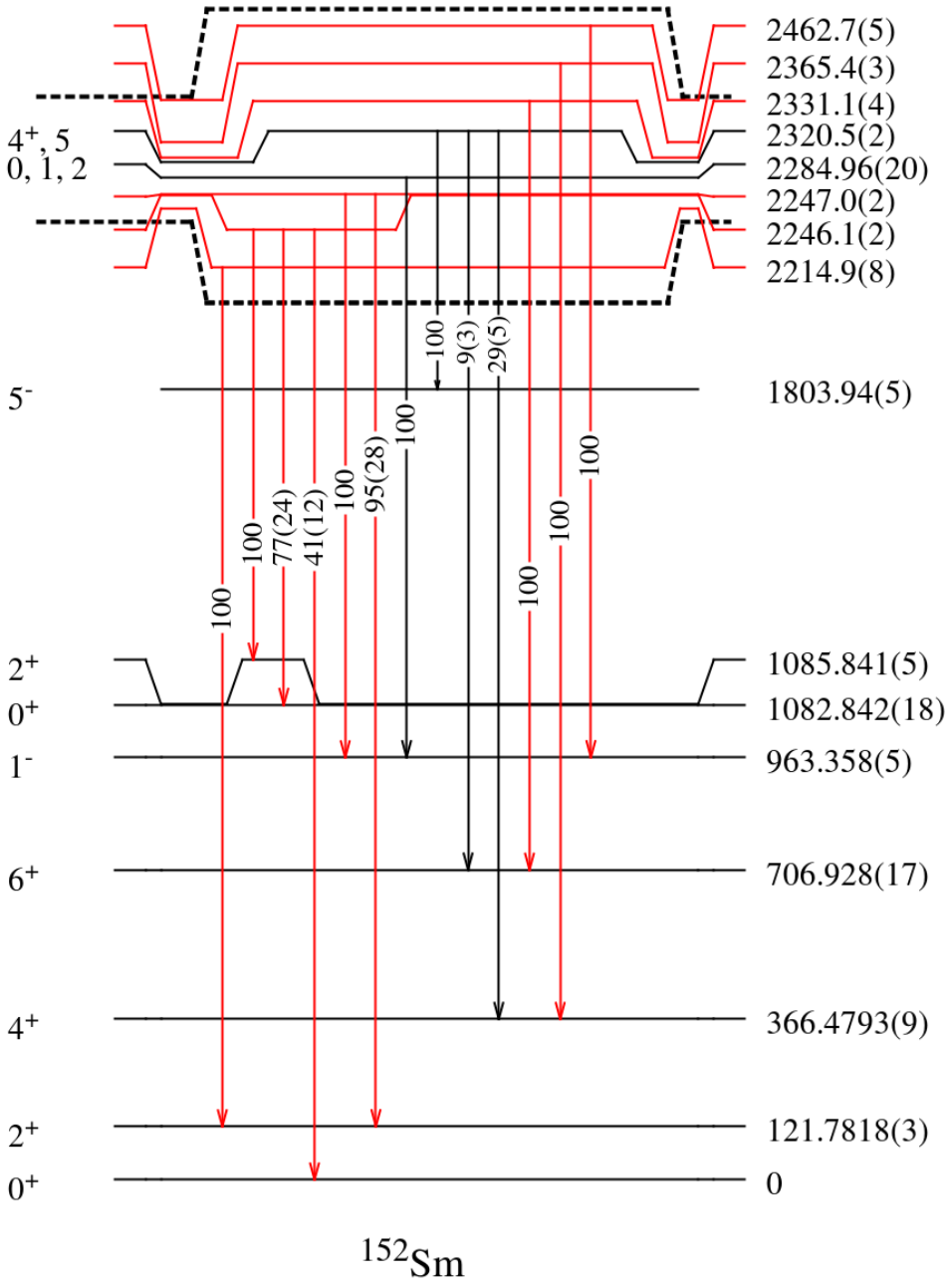

Figure 4.15: Same as Figure 4.14 but for ^{152}Sm.

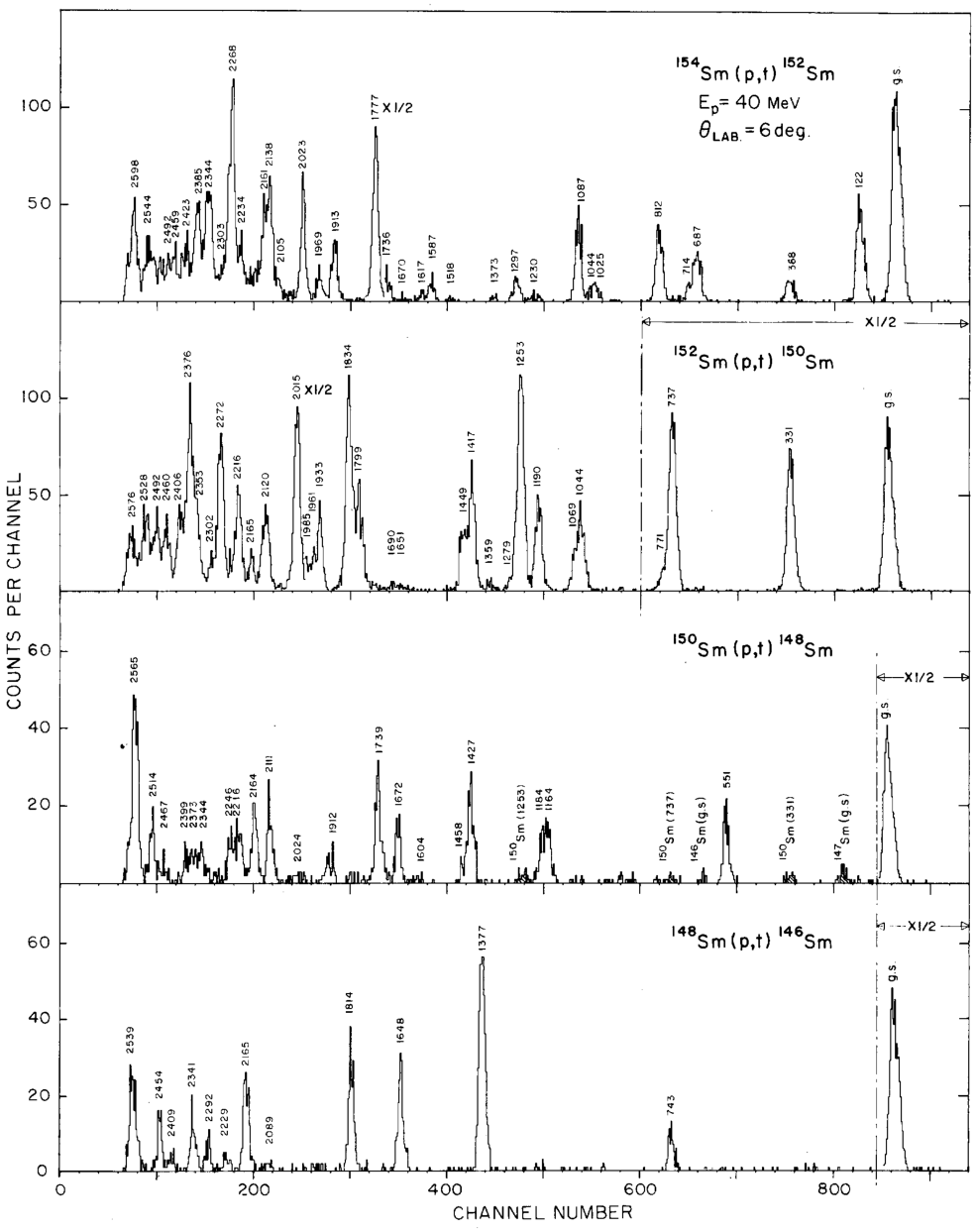

Figure 4.16: Triton energy spectra from the ^{148,150,152,154}Sm(p,t) reactions at an incident proton energy of 40 MeV. The peak energies are in keV. Reproduced with permission from Reference [20].

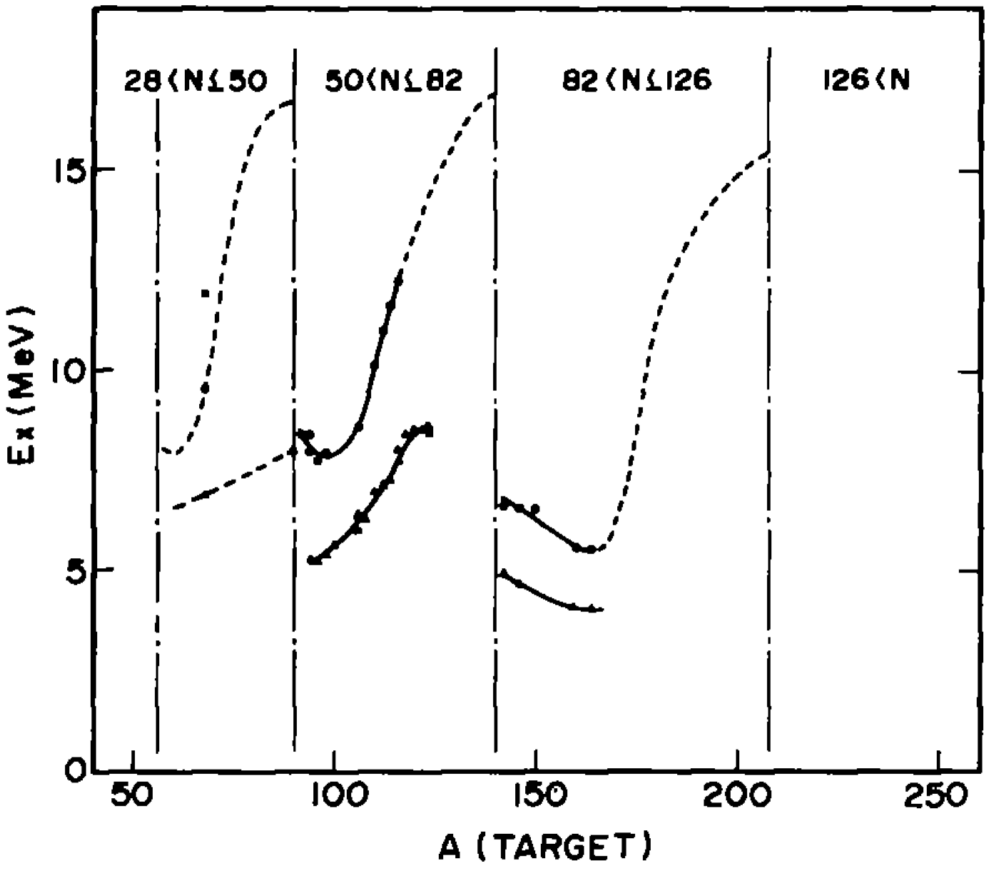

Figure 4.17: The excitation energy of the low-energy (solid triangles) and high-energy (solid circles) bumps plotted against mass number. Reproduced with permission from Reference [32], where the curves are described in full.

4.9 Isomeric Lifetimes in ^{152}Eu

The results presented in this section have been published in Physical Review C [56].

Nuclear isomers are states with lifetimes significantly longer than the typical prompt decay, from a few ns up to 10^{15} years for ^{180m}Ta. During the bombardment of the ^{154}Sm target, the (p,3n) reaction produced a significant amount of ^{152}Eu. This doubly-odd nucleus has a relatively large number of long-lived isomeric states [73], including a 9 hour $J^{\pi} = 0^{-}$ level at 46 keV and a 96 minute $J^{\pi} = 8^{-}$ level at 148 keV. A partial decay scheme of the long-lived (>1 hour) isomeric states of ^{152}Eu is shown in Figure 4.18. The half life of the 46 keV level is of interest since it is significantly populated in the astrophysical s process via the ^{151}Eu(n,γ) reaction [74].

Post irradiation, γ rays emitted from the activated target were measured using LiTeR in the γ-singles trigger mode. In Figure 4.19(a), the γ-ray energy spectrum obtained during the entire activation measurement is shown. Figure 4.19(b) shows the γ rays detected during the first hour of the measurement where the 90-keV γ ray from the decay of the 96 minute isomer can be seen. Figure 4.19(c) shows the long lived background remaining after 38 hours. In Figure 4.19(d) a two-dimensional plot of γ-ray energy against time is shown where the decay in intensity of the 90-keV and 122-keV γ rays can be seen.

By gating on the 90-keV γ ray in the matrix shown in Figure 4.19(d), a decay curve was produced and is shown in Figure 4.20. Background gates were chosen as close as possible to the peak of interest since the decay rate of the background has a strong energy dependence. This is due to the Compton scattering of multiple high-energy γ rays originating from relatively short-lived states. Choosing

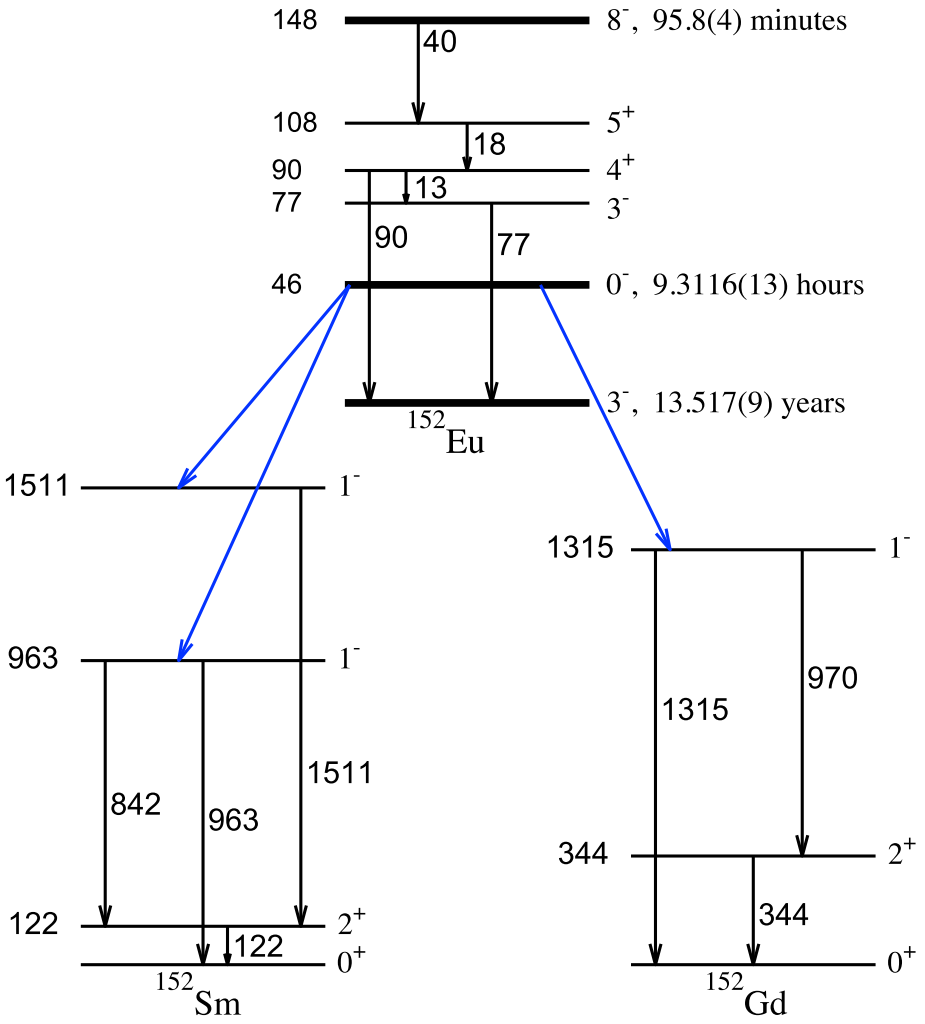

Figure 4.18: Partial decay scheme of the long lived (>1 hour) isomeric states of ^{152}Eu. The energies are in keV.

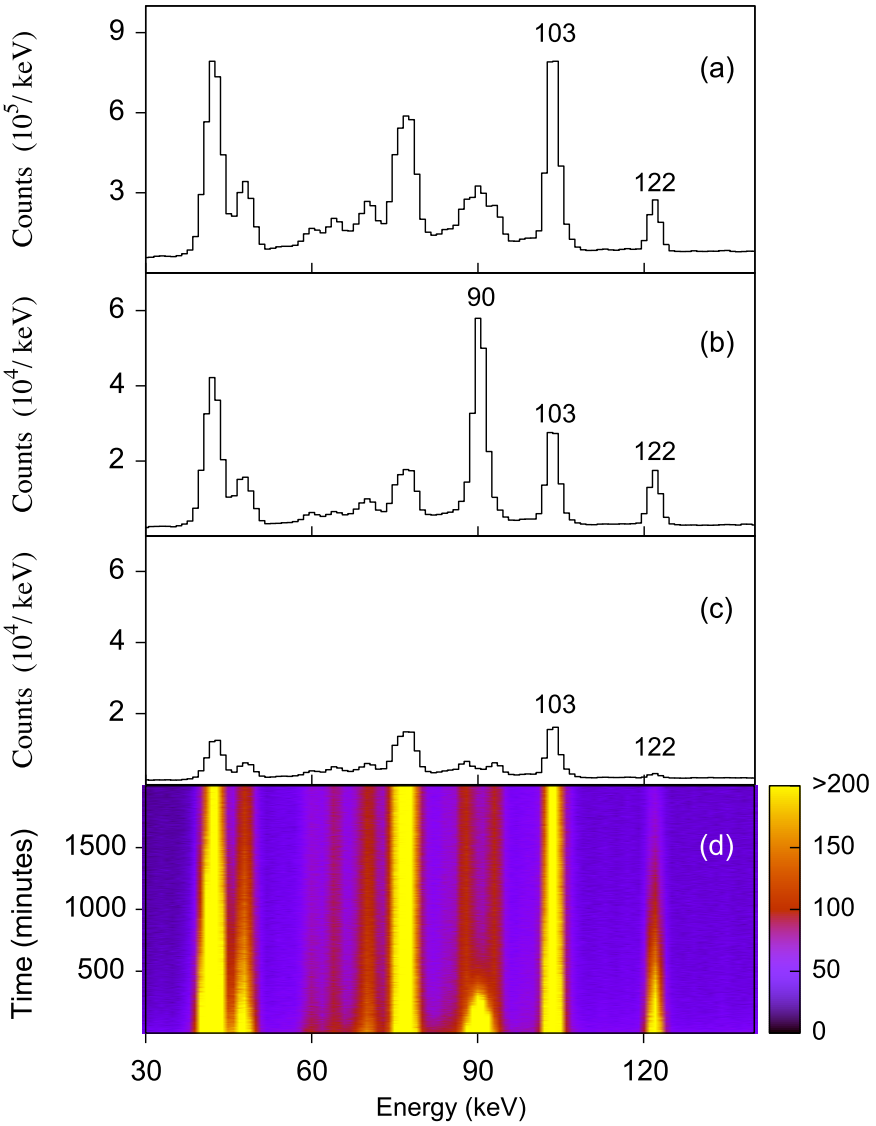

Figure 4.19: In panel (a) the low energy region of the γ-ray energy spectrum obtained during the entire activation measurement is shown. Panel (b) shows the spectrum obtained during the first hour of the activation measurement. In Panel (c) the γ rays remaining after 38 hours, also measured during a one hour period, are shown. Panel (d) shows a 2-D plot of γ-ray energy against time. Both the decay in intensity of γ rays from short lived states and the background peaks of constant intensity can be seen. Of particular note are the 90 and 122 keV γ rays which are shown in the level scheme in Figure 4.18.

background gates even a few keV from the peak of interest has a significant effect on the extracted half life. A single exponential fit to the data yielded a half life of 95.8(4) minutes for the decay of ^{152m2}Eu. This a significant reduction in uncertainty compared to the literature value of 96(1) minutes [75]. In addition to this measurement, four independent measurements of the half life of ^{152m1}Eu were made by directly measuring the decreasing photopeak areas of the 122, 334, 842 and 963 keV γ rays. The results of these measurements are shown in Figure 4.21. The grey band and blue line show the weighted mean of 9.39(7) hours and the respective uncertainty. In the inset of Figure 4.21, the value from the present work (blue point) is compared to five previous measurements [75–79] (black points). The value from the present work is in reasonable agreement with the previous measurements. The accepted literature value of 9.3116(13) hours lies slightly outside the experimental error bounds. However, there is a 12 sigma discrepancy between the two most precise previous measurements, calling into question at least one of the reported uncertainties.

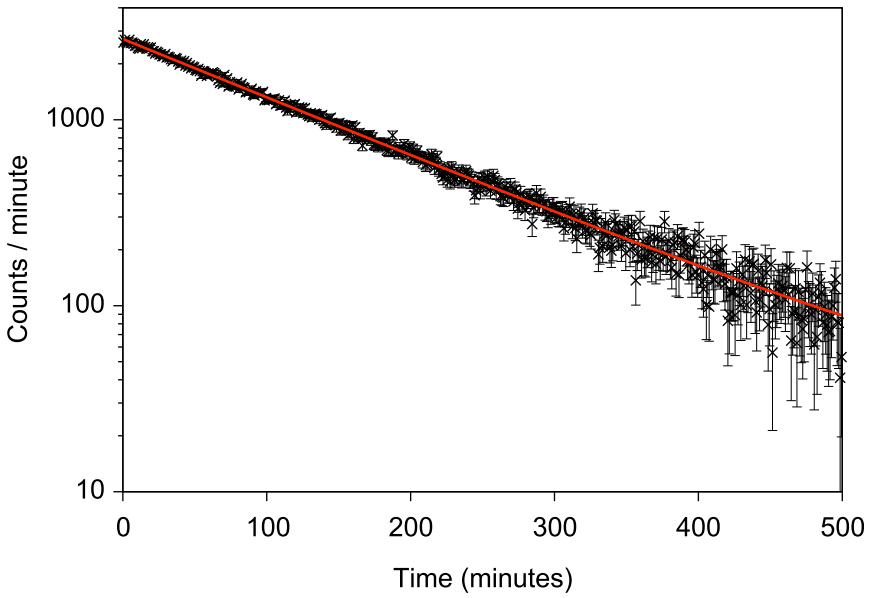

Figure 4.20: The intensity of the 90 keV γ ray from the decay of $^{152_{m2}}$Eu against time. The red line shows an exponential fit to the data

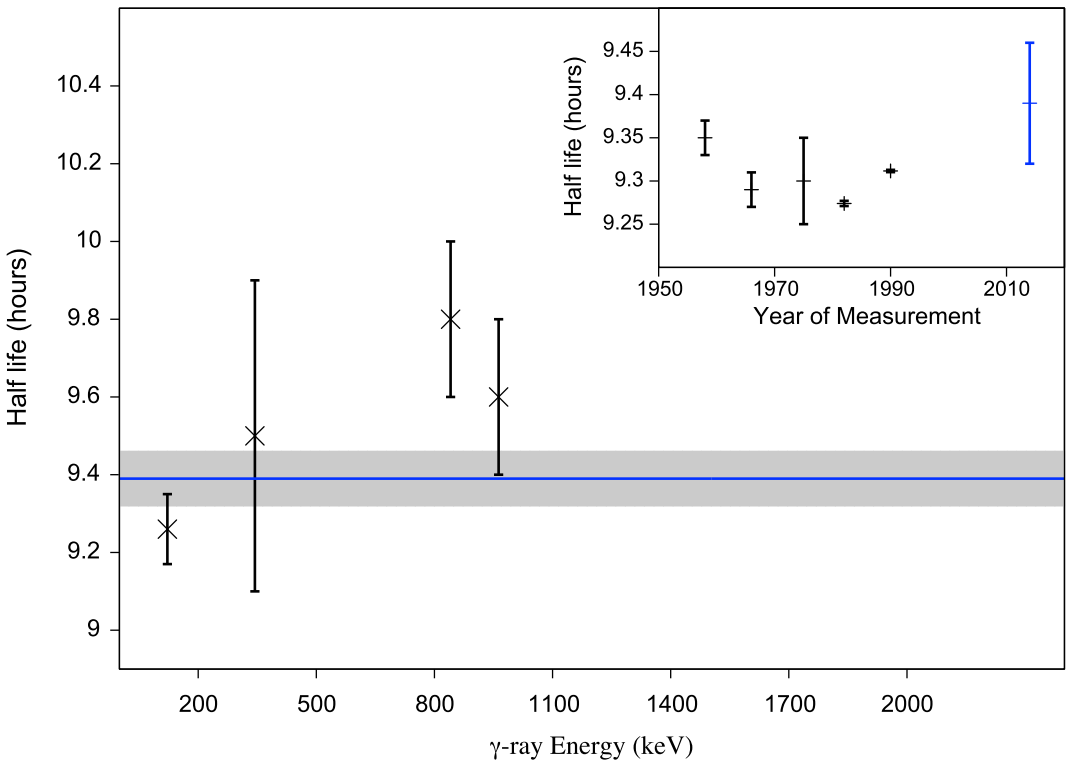

Figure 4.21: Measurements of the half-life of ^{152m1}Eu obtained by measuring the decrease in intensity of the 122, 334, 842 and 963 keV γ rays. The blue line and grey band show the weighted mean and uncertainty, respectively. In the inset, the previous measurements (black points) of the half life of ^{152m1}Eu [75–79] are compared to the value obtained in the present work (blue point).

Chapter 5

Summary

The nuclei ^{150,152}Sm have been studied using the ^{152,154}Sm(p,t) reactions and the particle-γ and particle-γ-γ coincidence techniques.

Numerous new levels and γ-ray transitions were identified, illustrating that the particle-γ coincidence technique is a powerful spectroscopic tool. The vast majority of the levels observed to be directly populated in the reaction were below $6\hbar$ in spin, highlighting the selectivity of the (p,t) reaction, and its usefulness in identifying relatively low spin states at intermediate and high excitation energies.

Relative partial cross sections were measured for the directly populated levels, angle averaged between 34°-58°. In general, the cross sections were found to be in good agreement with the previous measurements, despite the different reaction beam energies and the fact that the relative cross sections are quoted at different angles. The distribution of strength obtained for the population of discrete states is in good agreement with the shape of the triton singles spectrum in both reactions.

The angular distributions for discrete states directly populated in ^{150,152}Sm were measured over the angular range of the telescope from 34° to 58° and com-

pared to distributions calculated using the DWBA theory. No disagreements were found between the experimental angular distributions and the curves calculated by assuming the literature value for the spin of the level. For the levels newly observed in the present work, the statistics were insufficient for spin assignments.

Narrow peak-like structures between 2.2 to 3.2 MeV in excitation energy have been observed in the triton energy spectra in the ^{152,154}Sm(p,t) and ^{154,156,158}Gd(p,t) reactions. These structures lie between the region of strongly populated levels at low excitation energy and the smooth continuum region at high excitation energy. For Gd and Sm nuclei with the same neutron number, the energy of the structure is very similar, and the excitation energy of the structure decreases with increasing neutron number in the N=90 region. The large drop in the energy of the PLS between N=88 and N=90 occurs at the same point as the rapid onset of deformation in these nuclei. In ^{152}Sm, eight levels were identified in the region of the PLS and could account for 93(15)% of the PLS strength. In ^{150}Sm, three levels were identified in the region of the PLS, with a total of 39(4)% of the strength of the structure. It is therefore clear that the PLS strength is dominated by a relatively small number of discrete states, which is also supported by previous high resolution triton energy spectra for the case of ^{152}Sm.

Similar structures have been observed in (p,t) energy spectra across a wide range of nuclei from ^{66}Zn to ^{230}Th. These bumps appear to fall into high and low energy categories. The high-energy bumps may consist of levels formed by transferring both neutrons from deep below the Fermi surface below the major shell closure. The low-energy bumps may be formed by transferring one neutron from below the shell closure and one neutron from near the Fermi surface. In general, the widths of these structures are significantly wider than those observed

in the present work. If the PLS observed in the present work corresponds to the low energy bumps from the literature, then the decrease in energy of the structure between N=88 and N=90 could be explained by the rapid shape change, and the strongly up-sloping orbitals below the shell closure.

By measuring the decrease in intensity of γ rays emitted from the activated target, the half lives of isomeric states in ^{152}Eu were measured. A value of 95.8(4) min was obtained for the 8^- isomer $^{152_{m2}}$Eu, which is a factor 2.5 reduction in the uncertainty compared to the previous literature value. This result may be of some interest in the context of the astrophysical s process. A half life of 9.39(7) hours was obtained for $^{152_{m1}}$Eu, in agreement with the previous results within the experimental uncertainty.

Appendices

Appendix A

Paper Published in Physical Review C: Improved measurement of the half-life of the $J^{\pi} = 8^{-}$ nuclear isomer $^{152}{}_{m2}$Eu

Improved measurement of the half-life of the $J^\pi = 8^-$ nuclear isomer ^{152m_2}Eu

P. Humby,[1,2] A. Simon,[1,*] C. W. Beausang,[1] T. J. Ross,[3] R. O. Hughes,[4] J. T. Burke,[4] R. J. Casperson,[4] J. Koglin,[4] S. Ota,[4] J. M. Allmond,[5] M. McCleskey,[6] E. McCleskey,[6] A. Saastamoinen,[6] R. Chyzh,[6] M. Dag,[6] K. Gell,[1] T. Tarlow,[1] and G. Vyas[1]

[1]*Department of Physics, University of Richmond, Richmond, Virginia 23171, USA*
[2]*Department of Physics, University of Surrey, Surrey GU27XH, United Kingdom*
[3]*Department of Chemistry, University of Kentucky, Lexington, Kentucky 40506, USA*
[4]*Lawrence Livermore National Laboratory, Livermore, California 94551, USA*
[5]*Physics Division, Oak Ridge National Laboratory, Oak Ridge, Tennessee 37831, USA*
[6]*Cyclotron Institute, Texas A&M University, College Station, Texas 77843, USA*

(Received 12 November 2014; revised manuscript received 28 January 2015; published 23 February 2015)

The standard γ-ray energy calibration source ^{152}Eu is well known based on the 13.5 y decay of its ground state. However, in addition to this decay ^{152}Eu also has two relatively long-lived isomeric states: a 9 h $J^\pi = 0^-$ state at $E^* = 46$ keV and a 96 min $J^\pi = 8^-$ state at $E^* = 148$ keV. Here we report a new measurement of the half-lives of both of these isomeric states. Excited states in ^{152}Eu were populated following the ^{154}Sm$(p,3n)$ reaction using a 25 MeV proton beam from the K-150 cyclotron at the Cyclotron Institute of Texas A&M University. Post irradiation, γ rays from the de-excitation of the long lived isomeric states were measured using the six BGO shielded high-purity germanium (HPGe) clover detectors that are part of the STARLiTeR array. The half-life of the $J^\pi = 8^-$ isomer ^{152m_2}Eu was obtained by measuring the decrease in intensity of the 90 keV γ ray from the cascade to the ground state. The half-life of this state was measured to be 95.8(4) min which is in agreement with and significantly more precise than the previously measured value of 96(1) min. In a manner similar to the ground state the second long-lived isomer ^{151m_1}Eu, the $J^\pi = 0^-$ state at 46 keV, β decays to excited states in ^{152}Gd and ^{152}Sm. The half-life of this state was measured to be 9.39(7) h using five γ-ray transitions.

DOI: 10.1103/PhysRevC.91.024322 PACS number(s): 21.10.Tg, 23.35.+g

I. INTRODUCTION

Nuclear isomers, metastable states in atomic nuclei with lifetimes significantly longer than the typical prompt decay, occur throughout the chart of the nuclei [1]. The predominant decay mode is via γ decay although particle emission mediated either by the strong force (α decay), weak force (β decay), or fission is also possible and observed. Isomeric lifetimes range from a few ns to 10^{15} y for ^{180m}Ta, longer than the accepted lifetime of the universe. The lifetimes of these excited states probe the detailed wave functions of the underlying nuclear structure. Many isomers can be characterized as shell model states where the valence protons and neutrons couple to a higher spin state than other states at similar or lower excitation energies. The isomer decay then requires the emission of a γ ray typically of low energy that removes considerable angular momentum, resulting in long half-lives. Doubly odd ^{152}Eu lying in the heart of a region of the chart of the nuclei where the equilibrium shape is rapidly changing from spherical/vibrational to deformed rotational character has a relatively large number of long lived states with half-lives greater than 100 ns [2] including two known isomers with half-lives of the order of hours: a $J^\pi = 0^-$ state at 46 keV with a half-life of 9 h and a $J^\pi = 8^-$ state at 148 keV with a half-life of 96 min. The 46 keV isomer is significantly populated in the astrophysical s process via the ^{151}Eu(n,γ) reaction [3]. This could be important if thermal equilibrium is not achieved with the ground state, and with respect to this process the isomeric half-lives may be of some interest.

The isomer ^{152m_2}Eu, the 8^- level at 148 keV, decays via a 40 keV stretched $E3$ transition to a lower-lying 5^+ level and thence via a cascade of γ-ray transitions to the 3^- ground state, as shown in Fig. 1. The relatively short half-lives of the 5^+ and 4^+ states involved in this cascade, $\leqslant$20 ns and 384 (10) ns, respectively [2,4], allow the 90 keV transition to be used to measure the lifetime of ^{152m_2}Eu. The first measurement of this cascade dates from a 1963 article by Kirkby *et al.* [5] who identified a 92(2) keV γ ray with a half-life of 96(5) min. Numerous further measurements, for example [4,6,7], have identified this transition as belonging to the cascade of γ rays that originates from the decay of the 8^- isomer, specifically from a transition between the 4^+ state at 90 keV and the 3^- ground state, as shown in Fig. 1. The most recent measurement of the half-life of ^{152m_2}Eu was performed in 1974 by Pruys *et al.* [8] in which it was found to be 96(1) min.

The other long-lived isomer ^{152m_1}Eu, the 0^- level at 45.6 keV, β-decays to a variety of excited states in ^{152}Sm and ^{152}Gd in a manner similar to the ground state. Its half-life has previously been measured five times, most recently in 1990 by Abzouzi *et al.* [9] who obtained a very precise value of 9.3116(13) h. However this disagrees by 13 standard deviations from the previous, also very precise, measurement of Lagoutine *et al.* [10] who obtained 9.274(3) h, suggesting that for at least one of these measurements the values of the errors are underestimated.

The transition between ^{152m_1}Eu and the ground state of ^{152}Eu has a hindrance factor of $\geqslant 5 \times 10^7$ relative to the Weisskopf estimate [2]. This has been explained by

*Present address: Department of Physics, University of Notre Dame, Notre Dame, IN 46556.

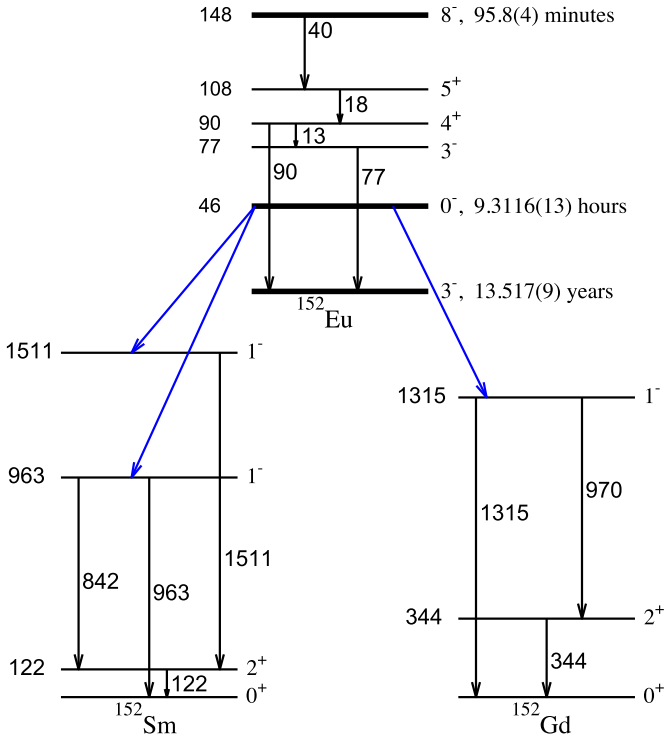

FIG. 1. (Color online) Partial decay schemes of ^{152m1}Eu and ^{152m2}Eu. γ-ray energies and excitation energies are in keV.

considering the Nilsson configurations of the proton and neutron orbitals; the ground state has been assigned main wave function components of $\pi 5/2^+[413\downarrow]$ $\nu 11/2^-[505\uparrow]$ whereas the 0^- isomer has been assigned $\pi 3/2^+[411\downarrow]$ $\nu 3/2^-[532\downarrow]$ [2]. Therefore, for the decay to occur both the neutron and proton must change orbits and the neutron transition is Ω forbidden. In this article we present new measurements of the half-lives of both of these isomeric states.

II. EXPERIMENTAL ARRANGEMENT

The experiment was conducted at the Cyclotron Institute of Texas A&M University using the STARLiTeR array. STARLiTeR consists of STARS (Silicon Telescope Array for Reaction Studies), a highly segmented ΔE-E charged particle telescope, a detailed description of which can be found in Ref. [11], and LiTeR (the Livermore Texas Richmond array), a Compton suppressed HPGe clover detector array for γ-ray detection. In the present work LiTeR consisted of six BGO shielded HPGe clover detectors positioned approximately 13 cm from the target at angles of 47°, 90°, and 133° with respect to the incident beam axis. The clover detectors were calibrated using the standard γ-ray calibration sources ^{22}Na, ^{54}Mn, ^{57}Co, ^{60}Co, ^{109}Cd, ^{133}Ba, ^{137}Cs, and ^{152}Eu. A final energy resolution of 2.6 keV and 3.5 keV (FWHM) was obtained at 122 keV and 963 keV, respectively. The absolute photopeak efficiency of the array, with addback, was measured to be 4.8% at 103 keV.

A ^{154}Sm target of thickness $\simeq$1 mg cm^{-2} and 99% enrichment was bombarded by a 25 MeV proton beam from the K-150 cyclotron with an average beam current of 1.2 nA for approximately 8 h immediately prior to the activation measurement. Unstable europium isotopes were produced via the ^{154}Sm(p, xn) reactions. Following this irradiation γ rays from the activated target were measured over a continuous period of 38 h. The energy and time for each γ-ray event was recorded for subsequent offline analysis. The time information was obtained from a 40 MHz clock pulse, digitized using a 64 bit TDC and used to generate γ-ray decay curves.

III. RESULTS

In Fig. 2(a) the low energy region of the γ-ray spectrum obtained during the entire activation measurement is shown. The spectrum obtained during the first hour of the measurement is shown in Fig. 2(b). The intense peak at 90 keV is identified as the 90 keV γ ray from the decay of ^{152m_2}Eu shown in Fig. 1. This is the only γ ray from this cascade observed in the current experiment. The 18 keV γ ray lies below the energy threshold of the experiment while the 40 keV transition is

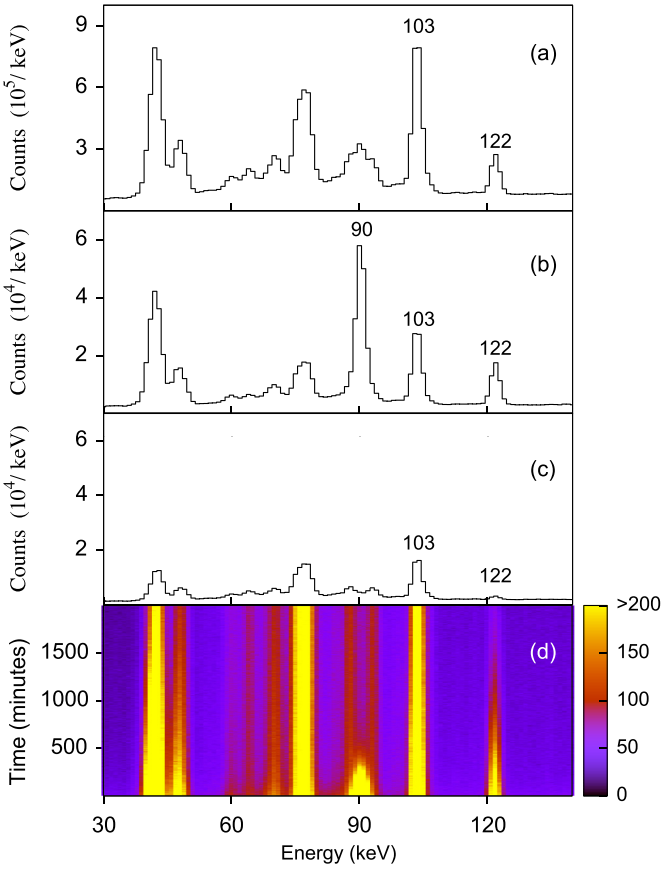

FIG. 2. (Color online) (a) The low energy region of the γ-ray spectrum obtained during the entire activation measurement. (b) The γ rays detected during the first hour of the measurement. (c) The γ rays remaining after 38 h, also measured during a 1 h period. (d) A two-dimensional plot of γ-ray energy against time showing the decrease in intensity of γ rays from the decay of relatively short-lived states as well as the near constant intensity of the long-lived background peaks. The 90 keV and 122 keV γ rays from Fig. 1 are labeled. The 103 keV γ ray is from the 46 h decay of ^{153}Sm, populated via the (p,d) reaction.

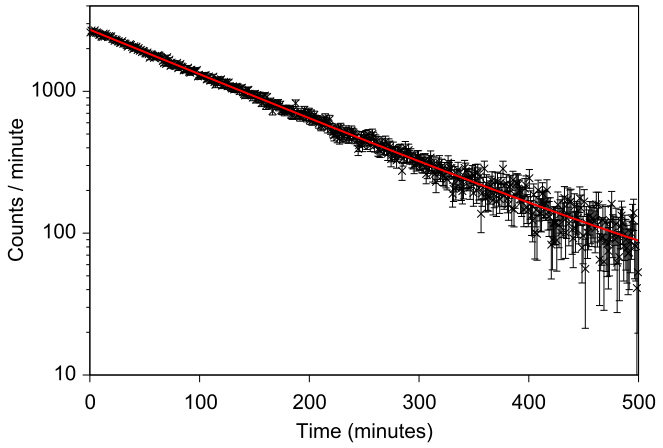

FIG. 3. (Color online) The decay in intensity of the 90 keV γ ray which originates from the decay of ^{152m_2}Eu. The red line shows an exponential fit to the data.

highly converted and was therefore also not observed. The 13 keV and 77 keV γ rays are too weak to be observed. Figure 2(c) shows the long-lived background remaining after 38 h. A γ-ray energy-time matrix is shown in Fig. 2(d) in which the long lifetimes of the two transitions bordering the 90 keV peak is apparent.

The decay rate of the background in the vicinity of the 90 kV peak has a strong energy dependence caused by Compton scattering of multiple high energy γ rays originating from relatively short-lived states. Detailed studies have shown that this can affect the extracted half-life for the 90 keV transition if background regions are chosen even a few keV away from the peak of interest, for example the potential background regions at approximately 110 keV and 125 keV that can be seen in Fig. 2(a). Therefore, two 4 keV wide background regions were chosen on both sides of and immediately adjacent to the 90 keV peak, despite the presence of two long-lived contaminant lines in this region of the spectrum. These peaks are visible in Figs. 2(a), 2(c), and 2(d), but play a relatively unimportant role for short decay times as seen in Fig. 2(b). The background spectrum was then appropriately weighted by area and subtracted from the decay curve produced by gating on the 90 keV peak. The resulting decay in intensity of the 90 keV γ rays after background subtraction is shown in Fig. 3. A single exponential fit to this data yielded a half-life of 95.8(4) min. for the decay of ^{152m_2}Eu, where the quoted uncertainty is statistical, and the reduced χ^2 of the fit is 0.74.

The γ rays at 122 keV, 334 keV, 842 keV, 963 keV, 970 keV, and 1315 keV, shown in the level scheme in Fig. 1, from the decay of ^{152m_1}Eu were observed. Independent measurements of the half-life of ^{152m_1}Eu using four of these γ rays are shown in Fig. 4. The γ rays at 970 keV and 1315 keV had insufficient statistics for a measurement. The contributions from the decay of the ground state of ^{152}Eu, which has a half-life of 13.517(9) years, were negligible due to the relatively long half-life compared to the 9 h decay of interest. The weighted mean of these measurements is 9.39(7) h, where the quoted uncertainty is again statistical.

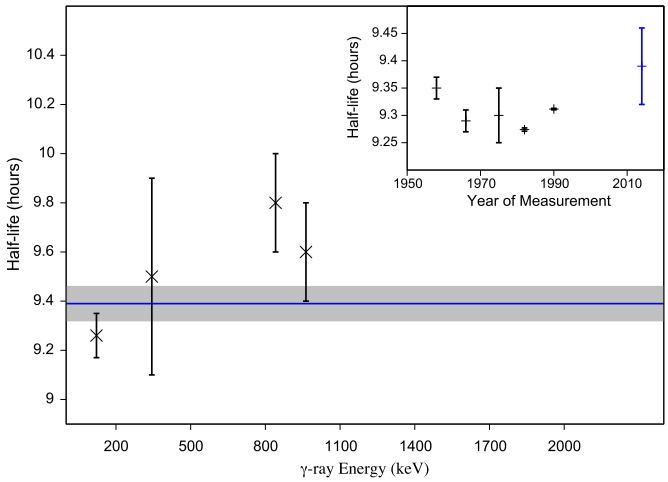

FIG. 4. (Color online) Measurements of the half-life of ^{152m_1}Eu obtained by measuring the decrease in intensity of the 122 keV, 334 keV, 842 keV, and 963 keV γ rays listed in Fig. 1. The blue line and grey band illustrate the weighted mean obtained in the present work and the associated uncertainty. Inset: Previous measurements of the half-life of ^{152m_1}Eu [8–10,14,15] (black points) compared to the value obtained in the present work (blue point).

The inset in Fig. 4 compares the value obtained in the present work to five previous measurements. We note that there is a 13 σ discrepancy between the two recent most precise measurements [9,10], calling into question at least one of the quoted uncertainties. In such cases the Particle Data Group [12] recommends a procedure for scaling the uncertainty. If we apply this procedure in this case the weighted average of all six measurements is 9.306(14) h. This is to be compared to the current NNDC value of 9.3116(13) h [13].

IV. SUMMARY AND CONCLUSIONS

In conclusion, by measuring the intensity of the 90 keV γ ray originating from the decay of the $J^\pi = 8^-$ isomer ^{152m_2}Eu the half-life of this state was measured to be 95.8(4) min, a factor of 2.5 reduction in uncertainty compared to previous measurement of 96(1) min. Using the 122, 334, 842, and 963 keV γ rays, four independent measurements of the half-life of ^{152m_2}Eu were made. The weighted mean of these was 9.39(7) h which is in reasonable agreement with the previous two most precise literature values of 9.3116(13) h and 9.274(3) h, values which disagree with each other by 13 σ. Using the procedure recommended by the Particle Data Group we find the weighted average of our value and the five previous measurements of ^{152m_2}Eu to be 9.306(14) h.

ACKNOWLEDGMENTS

This material is partly based upon work supported by the U.S. Department of Energy, Office of Science, Office of Nuclear Physics under Grant Nos. DE-FG02-05ER41379 and DE-FG02-93ER40773, by the U.S. Department of Energy, National Nuclear Security Administration under Grant Nos. DE-NA0001801 and DE-FG52-09NA29467, by the National Science Foundation under Contract No. PHY-130581, and by

the U.S. Department of Energy NNSA Office of Defense Nuclear Nonproliferation Research & Development under Contract No. DE-AC52-07NA27344 (Lawrence Livermore National Laboratory). The authors are grateful to the operators of the cyclotron at Texas A&M University for the excellent beam conditions.

[1] P. Walker and G. Dracoulis, Nature **399**, 35 (1999).
[2] T. von Egidy *et al.*, Z. Phys. A **286**, 341 (1978).
[3] H. Beer, F. Käppeler, K. Yokoi, and K. Takahashi, Astrophys. J. **278**, 388 (1984).
[4] K. Takahashi, M. McKeown, and G. Scharff-Goldhaber, Phys. Rev. **137**, B763 (1965).
[5] P. Kirkby and T. Kavanagh, Nucl. Phys. **49**, 300 (1963).
[6] J. Reierson, G. Nelson, and E. Hatch, Nucl. Phys. A **153**, 109 (1970).
[7] J. Simi, S. Koiki, and M. Radojevi-Stojanovi, in *Neutron Capture Gamma-Ray Spectroscopy*, edited by R. Chrien and W. Kane (Springer, New York, 1979), pp. 751–753.
[8] H. Pruys, E. Hermes, and H. V. Gunten, J. Inorg. Nucl. Chem. **37**, 1587 (1975).
[9] A. Abzouzi, M. Antony, V. Ndocko Ndongué, and D. Oster, J. Radioanal. Nucl. Chem. **145**, 361 (1990).
[10] F. Lagoutine and J. Legrand, Int. J. Appl. Radiat. Isot. **33**, 711 (1982).
[11] S. Lesher *et al.*, Nucl. Instrum. Methods . Phys. Res. A **621**, 286 (2010).
[12] K. Nakamura, J. Phys. G: Nucl. Part. Phys. **37**, 075021 (2010).
[13] Evaluated Nuclear Structure Data File (ENSDF) - National Nuclear Data Center (NNDC), Brookhaven National Laboratory, 2014.
[14] J. Corless, Isotopic Abundance Studies by Neutron Activation Analysis, Annual Report, April 15, 1964–April 14, 1966.
[15] G. Gueben and J. Govaerts, Inst. Interuniv. Sci. Nucleaires (Bruxelles), Monographie No. 2 (1958).

Appendix B

Paper Published in Physical Review C: Investigation of discrete states and quasi-discrete structures observed in ^{150}Sm and ^{152}Sm using the (p, t-γ) reaction

Investigation of discrete states and quasidiscrete structures observed in ^{150}Sm and ^{152}Sm using the $(p,t\gamma)$ reaction

P. Humby,[1,2] A. Simon,[1,3] C. W. Beausang,[1] J. M. Allmond,[4] J. T. Burke,[5] R. J. Casperson,[5] R. Chyzh,[6] M. Dag,[6] K. Gell,[1] R. O. Hughes,[5] J. Koglin,[5] E. McCleskey,[6] M. McCleskey,[6] S. Ota,[5] T. J. Ross,[7] A. Saastamoinen,[6] T. Tarlow,[1] and G. Vyas[1]

[1]*Department of Physics, University of Richmond, Richmond, Virginia 23171, USA*
[2]*Department of Physics, University of Surrey, Surrey, GU27XH, United Kingdom*
[3]*Department of Physics, University of Notre Dame, Notre Dame, Indiana 46556*
[4]*Physics Division, Oak Ridge National Laboratory, Oak Ridge, Tennessee 37831, USA*
[5]*Lawrence Livermore National Laboratory, Livermore, California 94551, USA*
[6]*Cyclotron Institute, Texas A&M University, College Station, Texas 77843, USA*
[7]*Department of Chemistry, University of Kentucky, Lexington, Kentucky 40506, USA*

(Received 19 September 2016; published 14 December 2016)

New levels and γ-ray transitions were identified in ^{150,152}Sm utilizing the (p,t) reaction and particle-γ coincidence data. A large, peak-like structure observed between 2.3–3.0 MeV in excitation energy in the triton energy spectra was also investigated. The orbital angular-momentum transfer was probed by comparing the experimental angular distributions of the outgoing tritons to calculated distorted wave Born approximation curves. The angular distributions of the outgoing tritons populating the peak-like structure are remarkably similar in the two reactions and are significantly different from the angular distributions associated with the nearby continuum region. Relative partial cross sections for the observed levels, angle averaged between 34 and 58 degrees, were measured. In ^{150}Sm, 39(4)% of the strength of the peak-like structure could be accounted for by the observed discrete states. This compares with a value of 93(15)% for ^{152}Sm.

DOI: 10.1103/PhysRevC.94.064314

I. INTRODUCTION

The samarium ($Z = 62$) isotopes near $N = 90$ lie in a region of rapid shape change from spherical to deformed with increasing neutron number. This has led to this region of the nuclear chart being the focus of intense experimental and theoretical study; see, for example, Refs. [1–6]. In the early two-neutron-transfer experiments by Maxwell [7] and Bjerregaard [8], excited $J^\pi = 0^+$ states were observed to have large cross sections relative to the ground state in the ^{152}Sm(p,t) and ^{150}Sm(t,p) reactions. This was interpreted in terms of shape coexistence [7,8] and the rapid onset of deformation, inviting further interest in these nuclei. In general, the $N = 90$ region provides a rich testing ground for models that attempt to describe transitional and deformed nuclei.

Two-neutron-transfer reactions provide an excellent tool with which to study both the removal of pairs of correlated neutrons from valence orbitals, typically populating states at relatively low excitation energies, as well as the removal of neutrons from deep below the Fermi surface. Following the work of Maxwell [7], further Sm(p,t) experiments were performed with improved energy resolution for the outgoing tritons (see, for example, Refs. [9–12]) at various incident proton beam energies. In the 1981 study by Struble *et al.* [13] a large, broad enhancement of two-neutron-transfer strength at an excitation energy of approximately 6 MeV was observed in the ^{148,150,152,154}Sm(p,t) reactions. An additional, much narrower, peak-like structure at an excitation energy of 2.2–3.1 MeV was observed in both the ^{152,154}Sm(p,t) reactions. In the ^{158}Gd$(p,t)^{156}$Gd study by Riezebos *et al.* [14] a rapid increase in 2^+, 4^+, and 6^+ strength was observed above 2 MeV in excitation energy. An interesting lack of monopole strength was reported above this energy, providing motivation to study the L-transfer distribution at this excitation energy in nearby nuclei.

In the present work, the peak-like structure (PLS) is studied in detail and ^{150,152}Sm are studied for the first time using the $(p,t\gamma)$ coincidence technique. The coincident detection of the γ ray allows for excellent selectivity and sensitivity and allows us to identify multiple new levels and γ-ray transitions in each nucleus. Triton angular distributions, selected by specific γ-ray transitions, probe the angular-momentum transfer to both low-lying discrete states and states in the PLS and are compared with calculated distorted wave Born approximation (DWBA) curves.

II. EXPERIMENTAL ARRANGEMENT

A 25 MeV proton beam from the K-150 cyclotron at the Cyclotron Institute of Texas A&M University was incident upon isotopically enriched ^{152}Sm and ^{154}Sm targets of 98% and 99% purity, respectively, and approximately 1 mg/cm^2 thickness. The ^{152}Sm target was bombarded for 42 h and the ^{154}Sm target for 35 h with average beam currents of 1.4 and 1.2 nA, respectively.

The outgoing light ions and γ rays were detected by using the STARLiTeR array, which uses the same configuration as that described in detail in Ref. [15]. This array consisted of the Silicon Telescope Array for Reaction Studies (STARS) ΔE-E silicon telescope and the Livermore Texas Richmond (LiTeR) array of bismuth-germanate-shielded (BGO-shielded) high-purity Ge (HPGe) clover detectors providing particle-γ and particle-γ-γ coincidence capability. A total of 1.5×10^5

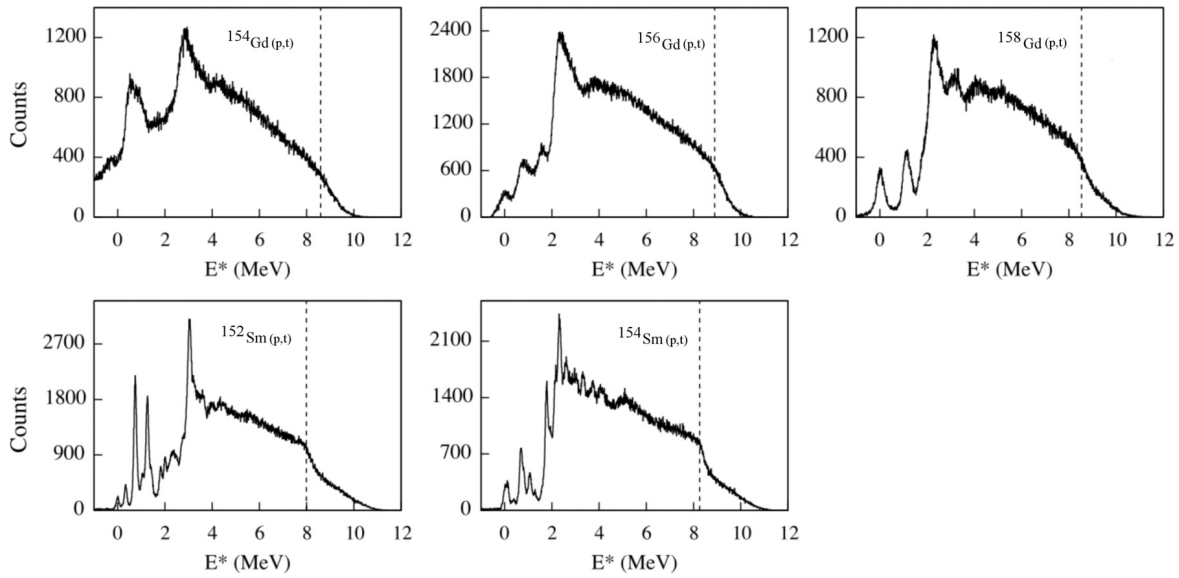

FIG. 1. Triton projections of the (t,γ) matrices produced in the ^{154,156,158}Gd(p,t) and ^{152,154}Sm(p,t) reactions. The single-neutron separation energies are indicated by the dashed lines. The Gd data are from Refs. [18,19]. It can be seen that the energy resolution is much improved in the Sm data.

t-γ-γ coincidences were observed for the ^{152}Sm(p,t) reaction and 1.4×10^5 for the ^{154}Sm(p,t) reaction, allowing t-γ-γ measurements for only the strongest transitions. STARS consisted of a 0.14-mm-thick ΔE detector and a 1-mm-thick E detector, both segmented into 24 rings (θ) and 8 sectors (ϕ). The distance between the target foil and the ΔE detector was 18 mm. The angular coverage of the telescope was 34 to 58 degrees. An aluminum δ shield was placed between the target position and STARS to shield the ΔE detector from secondary electrons. An aluminum tunnel passed through the center of the telescope to shield the inner rings from scattered beam particles. The six HPGe clover detectors were positioned in pairs at angles of 47°, 90°, and 133° with respect to the incident proton beam at a distance of 13 cm from the target position.

The Si telescope was calibrated by using a ^{226}Ra source which provides α particles at energies of 4.6, 4.8, 5.3, 5.5, 6.0, and 7.7 MeV. An additional nine calibration points between 4.4 and 16.1 MeV were obtained by using levels populated in the ^{12}C(p,p') reaction. Well-known levels at low excitation energy populated in the ^{152,154}Sm(p,t) reactions as well as the onset of the ^{152,154}Sm(p,tn) channels at the neutron separation energies of 7.9867(4) and 8.2577(6) MeV [16], respectively, were also used. Energy deposited in adjacent rings of the Si detectors was summed and induced noise in neighboring rings was corrected for. The energy losses due to the Al and Au dead layers of the Si detectors were calculated by using the Energy Loss And Straggling Tool (ELAST) program [17] and the recoil energy imparted to the target nucleus was also accounted for. A resolution (full width at half maximum, FWHM) of 130 keV was obtained for the ground state of ^{150}Sm in the ^{152}Sm(p,t) reaction.

The HPGe clover detectors were calibrated using ^{22}Na, ^{54}Mn, ^{57}Co, ^{60}Co, ^{109}Cd, ^{133}Ba, ^{137}Cs, and ^{152}Eu sources. The photopeak efficiency was 4.8% at 103 keV and an energy resolution of 2.6 and 3.5 keV (FWHM) was obtained at energies of 122 and 963 keV, respectively.

III. TRITON PROJECTIONS AND IDENTIFICATION OF DISCRETE STATES

Energy spectra for tritons in coincidence with γ rays from the recent ^{154,156,158}Gd(p,t) studies by Ross *et al.* [18] and Allmond *et al.* [19] are shown in Fig. 1 and compared with those obtained in the present work for the ^{152,154}Sm(p,t) reactions. The PLS is clearly present between 2.1–3.3 MeV excitation energy in all of these reactions. The excitation energy of the structure is plotted in Fig. 2 and appears to decrease with increasing neutron number.

Particle-γ coincidences are a powerful spectroscopic tool; see, for example, Ref. [20]. A gate placed on a triton energy of

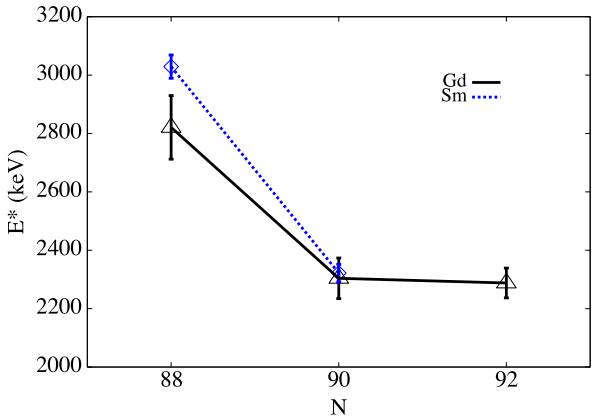

FIG. 2. The excitation energy of the PLS as a function of neutron number for the Gd (black points and solid black line) and Sm (blue points and dashed blue line) isotopes.

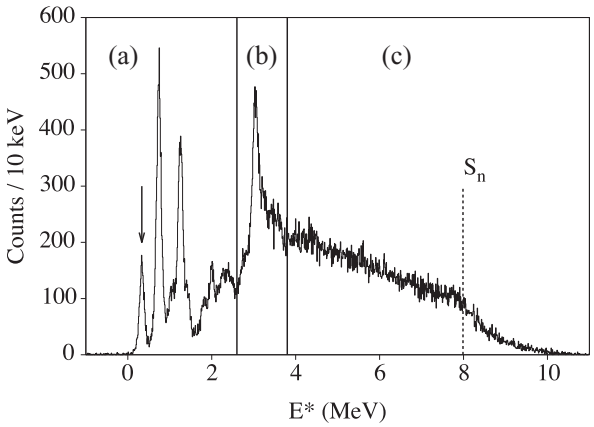

FIG. 3. Triton energy spectrum in coincidence with the 334 keV γ-ray transition between the first 2^+ state in ^{150}Sm and the ground state. The triton peak corresponding to direct population of the level is indicated by the arrow. In part (a), peaks corresponding to discrete states can be seen. In part (b), at intermediate excitation energy, the PLS is present. In part (c), the smoothly varying continuum region and the onset of the (p,tn) channel above the single-neutron separation energy can be observed.

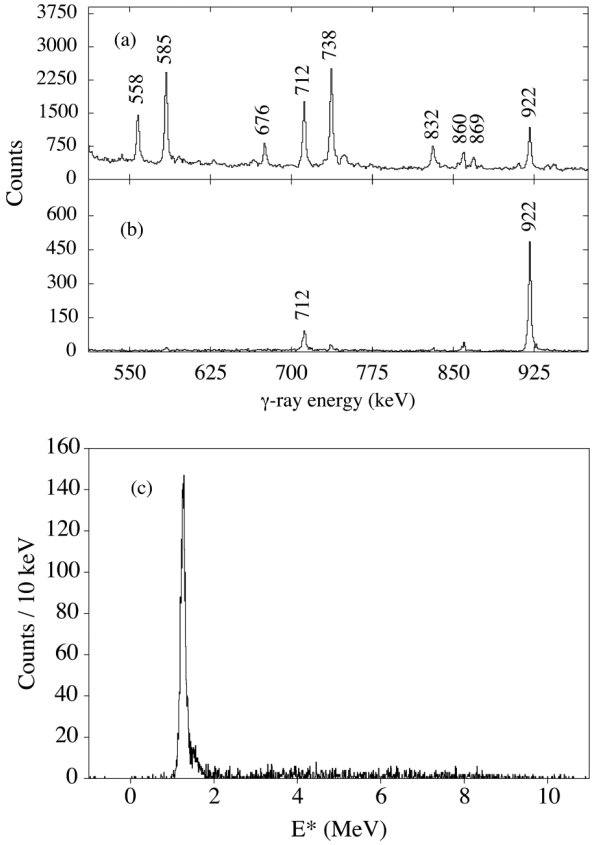

FIG. 4. (a) A γ-ray energy spectrum showing a section of the total γ-ray projection from the ^{152}Sm$(p,t\gamma)$ coincidence matrix. (b) The γ-ray energy spectrum in coincidence with tritons corresponding to an excitation energy between 1210 and 1290 keV. The 922 keV γ ray is from the level at 1255 keV in ^{150}Sm. The 712 keV γ is from the level at 1046 keV, which is fed by the 1255 keV level via a 209 keV transition not shown in the figure. (c) A triton energy spectrum in coincidence with the 922 keV γ ray. The narrow peak corresponds to direct population of the 1255 keV level. In contrast to the 2_1^+ to ground-state transition, notice that for this nonyrast level there is comparatively little feeding from higher-lying excited sates.

interest in the t-γ coincidence matrix corresponds to gating on a certain excitation energy in the residual nucleus. This gate returns a spectrum of γ rays that must be emitted from states at or below this excitation energy and often enhances low-intensity γ rays that are obscured in the total projection. On the other hand, gating on a γ ray in the t-γ matrix typically gives a triton energy spectrum with a discrete peak corresponding to the direct population of the γ-ray emitting level, as well as counts at higher excitation energy which correspond to states that feed that level, both directly and indirectly. These features can be observed in the spectrum shown in Fig. 3 obtained with a gate placed on the 334 keV γ ray from the transition between the first 2^+ state in ^{150}Sm and the ground state. The peak at 334 keV corresponds to direct population of the 2^+ level. Also visible are the plethora of other discrete states that are directly populated by the (p,t) reaction and then feed the 2^+ state as well as a smooth continuum region above approximately 3.5 MeV. A further example is shown in Fig. 4. In Fig. 4(a), a γ-ray energy spectrum showing a section of the total γ-ray projection from the ^{152}Sm$(p,t\gamma)$ coincidence matrix is shown. Figure 4(b) shows a γ-ray energy spectrum in coincidence with tritons corresponding to an excitation energy range of 1210–1290 keV in ^{150}Sm. The 922 keV γ ray is from the level at 1255 keV. The 712 keV transition is from the level at 1046 keV, which is fed by the 1255 keV level via a 209 keV transition not shown in the figure. Figure 4(c) shows a triton energy spectrum in coincidence with the 922 keV γ ray. This spectrum, typical of those observed when gating on nonyrast levels, shows the direct population peak at 1255 keV and very little feeding from higher-lying excited states.

To identify new discrete states in ^{150,152}Sm, a gate is first placed on a γ ray of interest in the t-γ matrix. The approximate excitation energy of the level (typical accuracy of ~20–30 keV) is then measured by fitting the energy of the triton peak (see Fig. 4), corresponding to direct population of the level. Subtracting the γ-ray energy from the excitation energy corresponding to the triton peak often identifies the level that is being fed by the transition. This can only be performed unambiguously either when there is just one possible final level within the experimental uncertainty, when multiple γ rays depopulate the level, or when the γ-ray placement can be confirmed by using t-γ-γ coincidences. Once the γ ray has been placed in the level scheme, the γ-ray energy can be summed with the energy of the level that is being fed, which provides a much more precise measurement (typically 0.2 keV) of the excitation energy of the state of interest; see Ref. [20] for more details.

The levels and γ rays observed in ^{150,152}Sm are listed in Tables I and II, respectively. Numerous new levels and γ-ray-emitting transitions were identified. In the first two columns the level energy and γ-ray energies are listed. The relative γ-ray branching for each level, expressed as a percentage of the strongest transition, is listed in the third

TABLE I. Levels and γ rays observed in the ^{152}Sm(p,t) reaction. Refer to the text for the full description of each column. The uncertainties are indicated by the superscript. Newly identified levels and γ rays are shown in bold. A dash in columns 4 and 5 indicates that the triton peak corresponding to the direct population of the level was not measured in coincidence with the γ ray in this row. This tends to occur for levels that are strongly fed by higher-lying states. In this case, a γ ray may still be placed if there are multiple observed transitions depopulating the level, or if it is a well-known transition from a low-lying state.

E_x (keV)	E_γ (keV)	I_γ	E_x^t (keV)	$E_x^t - E_\gamma$ (keV)	E_f^{ND} (keV)	$E_\gamma + E_f^{ND}$ (keV)	$J^{\pi,ND}$	E_x^{ND} (keV)	E_γ^{ND} (keV)	I_γ^{ND}	$\sigma_{(34°-58°)}$ (% of 2_1^+)
333.7^2	333.7^2	100	341^{14}	7^{14}	0	333.7^2	2^+	333.955^{10}	333.961^{11}	100^3	100^2
740.6^2	406.6^2	100	741^4	334^4	333.96	740.6^2	0^+	740.464^{19}	406.508^{22}	100	282^6
773.3^3	439.3^3	100	780^5	341^5	333.96	773.3^3	4^+	773.374^{12}	439.400^{14}	100	9.7^8
1046.3^2	712.4^3	100	1054^{11}	342^{11}	333.96	1046.4^3	2^+	1046.148^{13}	712.207^{14}	100^6	32^2
	1046.2^2	6^2	1031^{13}	−15^{13}	0	1046.2^2			1046.16^{14}	8.1^9	
1071.7^2	297.5^5	8^2	–	–	773.37	1070.9^5	3^-	1071.406^{12}	298.060^{13}	6.70^{23}	22^2
	737.7^2	100	1070^5	332^5	333.96	1071.7^2			737.457^{15}	100.0^{19}	
1165.6^2	831.6^3	84^5	–	–	333.96	1165.6^3	1^-	1165.791^{17}	831.83^5	75^3	–
	1165.5^3	100	–	–	0	1165.5^3			1165.74^3	100^4	
1193.9^2	860.0^3	67^5	1193^5	332^5	333.96	1194.0^3	2^+	1193.843^{12}	859.88^3	73.3^{16}	38^2
	1193.8^2	100	1194^4	0^4	0	1193.8^2			1193.830^{22}	100^3	
1255.4^1	209.2^2	11^1	1258^4	1049^4	1046.15	1255.3^2	0^+	1255.512^{20}	209.364^{19}	8.9^{16}	186^4
	921.5^2	100	1259^4	338^4	333.96	1255.5^2			921.55^{13}	100^7	
1278.9^2	505.5^2	100	1271^7	766^7	773.37	1278.9^2	6^+	1278.922^{14}	505.508^{23}	100	5.5^6
1357.9^4	584.5^4	100	1365^7	781^7	773.37	1357.9^4	5^-	1357.710^{13}	584.274^{12}	100^3	6^1
1417.2^2	251.2^4	48^5	1418^5	1167^5	1165.74	1417.0^4	2^+	1417.346^{13}	251.582^{19}	43.7^{18}	30^2
	345.8^3	100	1417^4	1071^4	1071.41	1417.2^3			345.950^{17}	100^{10}	
	1083.3^3	30^5	1427^{10}	344^{10}	333.96	1417.3^3			1083.34^4	70^8	
1449.7^4	676.3^4	100	1454^{12}	778^{12}	773.37	1449.7^4	4^+	1449.182^{13}	675.853^{24}	100^2	2.3^6
1505.2^6	1171.2^6	100	–	–	333.96	1505.2^6	3^+	1504.572^{13}	1170.589^{24}	100.0^{14}	–
1603.1^7	**1269.1^7**	100	1610^{40}	341^{40}	333.96	1603.1^7		1603^4			1.1^4
1642.6^7	869.2^7	100	1638^{22}	769^{22}	773.37	1642.6^7	4^+	1642.611^{12}	869.256^{14}	100^1	2.0^5
1684.1^3	911.0^6	60^7	1715^{27}	804^{27}	773.37	1684.4^6	3^-	1684.162^{17}	910.88^4	50^6	3.5^6
	1349.9^4	100	1698^{20}	348^{20}	333.96	1683.9^4			1350.28^{10}	100^6	
1764.8^3	485.9^3	100	1783^{20}	1297^{20}	1278.92	1764.8^3	7^-	1764.89^4	485.8^3	100^4	1.1^3
1786.3^5	620.5^5	100	1778^{12}	1158^{12}	1165.79	1786.3^5	($\leqslant$3)	1786.30^{13}	620.40^{20}	95^{16}	1.8^5
1794.2^2	600.5^4	44^8	–	–	1193.84	1794.3^4	2^+	1794.30^3	600.43^{25}	15^3	13^1
	628.5^3	100	1796^7	1168^7	1165.79	1794.3^3			628.56^{14}		
	722.9^4	56^{10}	1802^{12}	1079^{12}	1071.41	1794.3^4			722.65^{18}	24^4	
	1459.9^4	42^{10}	1764^{16}	304^{16}	333.96	1793.9^5					
1819.9^2	748.5^2	100	1806^{12}	1058^{12}	1071.41	1819.9^2	4^+	1819.510^{13}	748.06^9	100^2	7.6^9
	1485.5^6	24^8	1828^{26}	343^{26}	333.96	1819.5^6			1485.50^{14}	36.7^{15}	
1826.7^3	**1053.3^3**	100	1824^8	771^8	773.37	1826.7^3					5.3^7
1832.8^2	667.3^3	48^8	1834^{10}	1167^{10}	1165.79	1833.1^3	$(2)^+$	1833.01^3	667.05^3	100^4	13^1
	1498.7^2	100	1832^8	333^8	333.96	1832.7^2			1499.35^{10}	15.2^7	
1836.9^2	558.1^2	100	–	–	1278.92	1836.9^2	8^+	1837.03^{10}	558.1^1	100	–
1950.2^2	1176.8^2	100	1960^7	783^7	773.37	1950.2^2	3^-	1952.46^3	1176.6^{13}	100^{20}	8.6^9
1962.9^7	1222.4^7	100	1948^{28}	726^{28}	740.46	1962.9^7	$1^{(-)}$	1963.72^4	1223.26^8	100^7	1.5^5
2004.8^4	811.2^6	45^{12}	2005^{14}	1194^{14}	1193.84	2005.0^6	2^+	2005.5^8	812.1^8		7^1
	2004.6^5	100	2008^{16}	3^{16}	0	2004.6^5					
2117.0^4	1343.6^4	100	2114^{12}	770^{12}	773.37	2117.0^4	4^+	2117.030^{15}	1343.78^{22}	100^3	4.9^7
2152.7^4	1379.3^4	100	2157^{17}	778^{17}	773.37	2152.7^4	4^+	2152.56^3	1379.12^6	100^{12}	4.3^7
2260.1^3	1926.1^3	100	2265^9	339^9	333.96	2260.1^3	(1^-)	2259.94^4	1926.04^8	33^7	11^1
2362.6^2	**1290.9^3**	66^{13}	2358^8	1067^8	1071.41	2362.3^3					13^1
	2028.9^3	100	2373^{12}	344^{12}	333.96	2362.9^3					
2587.2^4	**1813.8^4**	100	2602^{24}	773^{24}	773.37	2587.2^4	$3^+,4^+$	2587.3^5			4.3^9
2654.9^7	**2320.9^7**	100	2640^{22}	319^{22}	333.96	2654.9^7	(3,5)	2655^7			4.0^9
2715.5^3	**1521.7^3**	100	2734^{18}	1212^{18}	1193.84	2715.5^3	3^-	2715^4			5.5^8
3018.3^6	**1852.5^6**	100	3018^{12}	1166^{12}	1165.79	3018.3^6					4.3^9
3037.8^9	2702.9^{13}	100	3042^8	339^8	333.96	3036.9^{13}	$1,2^+$	3038.2^4	2704.6^7	100^5	40^3
	3038.5^{12}	30^8	3060^{18}	22^{18}	0	3038.5^{12}			3037.8^{10}	33^{17}	
3045.3^{15}	**2711.3^{15}**	100	3045^9	334^9	333.96	3045.3^{15}					38^3

TABLE II. Same as Table I but for the ^{154}Sm(p,t) reaction. Refer to the text for full description of each column. The uncertainties are indicated by the superscript. Newly identified levels and γ rays are shown in bold.

E_x (keV)	E_γ (keV)	I_γ	E_x^t (keV)	$E_x^t - E_\gamma$ (keV)	E_f^{ND} (keV)	$E_\gamma + E_f^{ND}$ (keV)	$J^{\pi,ND}$	E_x^{ND} (keV)	E_γ^{ND} (keV)	I_γ^{ND}	$\sigma_{(34°-58°)}$ (% of 2_1^+)
121.7[2]	121.7[2]	100	115[8]	−7[8]	0	121.7[2]	2^+	121.7818[3]	121.7817[3]	100	100[2]
366.2[2]	244.4[2]	100	364[9]	119[9]	121.78	366.2[2]	4^+	366.4793[9]	244.6974[8]	100	8.0[5]
685.2[3]	563.4[3]	100	681[9]	118[9]	121.78	685.2[3]	0^+	684.751[21]	562.98[3]	100.0[19]	95[2]
706.7[3]	340.2[3]	100	704[8]	364[8]	366.48	706.7[3]	6^+	706.928[17]	340.45[3]	100	6.5[5]
810.6[2]	443.7[5]	36[3]	812[7]	368[7]	366.48	810.2[5]	2^+	810.453[5]	444.00[3]	34.8[13]	47[2]
	688.8[2]	100	817[8]	128[8]	121.78	810.6[3]			688.670[5]	100.0[6]	
	810.7[4]	46[4]	799[7]	−12[7]	0	810.7[4]			810.451[5]	37.0[3]	
963.3[3]	841.5[2]	100	–	–	121.78	963.3[3]	1^-	963.358[5]	841.570[5]	100.0[18]	–
1023.1[3]	656.5[3]	100	1025[12]	369[12]	366.48	1023.0[3]	4^+	1022.970[5]	656.489[5]	100.0[15]	5.0[7]
	901.6[5]	69[16]	1039[14]	137[14]	121.78	1023.4[5]			901.19[5]	59.2[17]	
1041.2[2]	674.7[4]	27[5]	1036[12]	361[12]	366.48	1041.1[4]	3^-	1041.122[4]	674.65[3]	40.4[8]	13[1]
	919.5[3]	100	1031[8]	112[8]	121.78	1041.3[3]			919.337[4]	100.0[10]	
1085.6[2]	963.7[3]	100	1082[8]	118[8]	121.78	1085.5[3]	2^+	1085.841[5]	964.057[5]	100.00[24]	42[2]
	1085.7[3]	57[5]	1089[9]	3[9]	0	1085.7[3]			1085.837[10]	69.71[10]	
1125.3[3]	418.4[3]	100	–	–	706.93	1125.3[3]	8^+	1125.39[3]	418.45[3]	100	–
1221.6[3]	855.1[3]	100	1214[11]	359[11]	366.48	1221.6[3]	5^-	1221.64[3]	855.21[7]	100[3]	3.5[5]
1233.9[2]	867.9[4]	46[8]	–	–	366.48	1234.4[4]	3^+	1233.863[3]	867.380[3]	30.93[18]	–
	1112.0[2]	100	–	–	121.78	1233.8[2]			1112.076[3]	100.0[5]	
1293.0[14]	926.5[14]	100	1276[15]	350[15]	366.48	1293.0[14]	2^+	1292.773[10]	926.29[4]	100.0[12]	2.2[5]
1310.5[3]	603.6[3]	100	–	–	706.93	1310.5[3]	6^+	1310.505[22]	603.56[3]	100[4]	–
1371.7[3]	1005.2[6]	100	1393[22]	388[22]	366.48	1371.7[3]	4^+	1371.735[12]	1005.27[5]	100.0[16]	3.2[5]
1505.9[3]	799.0[3]	100	–	–	706.93	1505.9[3]	7^-	1505.77[3]	798.82[3]	100[3]	–
1510.9[4]	1389.1[4]	100	1542[20]	153[20]	121.78	1510.9[4]	1^-	1510.790[25]	1389.03[4]	100.0[21]	1.6[5]
1559.6[3]	1193.1[3]	100	–	–	366.48	1559.6[3]	5^+	1559.62[3]	1193.10[5]	100[3]	–
1579.4[2]	1212.9[2]	100	1577[9]	364[9]	366.48	1579.4[2]	3^-	1579.429[11]	1212.948[11]	100.0[4]	8[1]
	1457.4[4]	42[10]	1574[18]	117[18]	121.78	1579.2[4]			1457.643[11]	35.13[26]	
1609.0[4]	483.6[4]	100	–	–	1125.39	1609.0[4]	10^+	1609.26[4]	483.86[3]	100	–
1613.8[4]	906.9[4]	100	1618[16]	711[16]	706.93	1613.8[4]	4^+	1612.90[4]	906.06[10]	100[5]	1.4[4]
1659.8[3]	696.4[3]	100	1680[12]	984[12]	963.36	1659.8[3]	0^+	1658.80[25]	695.9[3]	100[5]	7[1]
1728.2[5]	1021.3[5]	100	–	–	706.93	1728.2[5]	6^+	1728.27[3]	1021.41[4]	100[3]	–
1755.1[2]	791.7[2]	100	1772[12]	980[12]	963.36	1755.1[2]	0^+	1754.98[4]	791.67[7]	100[5]	9.8[8]
1764.3[3]	1057.2[5]	68[20]	1764[19]	707[19]	706.93	1764.1[5]	5^-	1764.32[5]	1057.36[6]	100[6]	3.2[7]
	1398.0[4]	100	1775[18]	377[18]	366.48	1764.5[4]			1397.88[7]	82[5]	
1769.0[1]	397.5[5]	5[2]	–	–	1371.74	1769.2[5]	2^+	1769.132[23]	397.75[26]	1.9[3]	141[5]
	535.2[3]	12[2]	1796[8]	1261[8]	1233.86	1769.1[3]			535.44[12]	8.8[7]	
	683.9[8]	25[3]	–	–	1085.84	1769.7[8]			683.25[9]	24.1[14]	
	728.3[5]	58[6]	1773[4]	1045[4]	1041.12	1769.4[5]			728.03[4]	56.5[19]	
	805.5[6]	68[6]	1760[8]	955[8]	963.36	1768.9[6]			805.71[9]	77[3]	
	958.5[3]	100	1777[4]	819[4]	810.45	1769.0[3]			958.63[5]	100[6]	
	1084.5[2]	79[6]	–	–	684.75	1769.3[2]			1084.36[14]	54[4]	
	1646.7[3]	36[5]	1781[9]	134[9]	121.78	1768.5[3]			1647.44[12]	36.9[18]	
	1768.9[2]	68[8]	1779[8]	10[8]	0	1768.9[2]			1769.09[5]	47.3[11]	
1879.5[3]	754.1[3]	100	–	–	1125.39	1879.5[3]	9^-	1879.14[4]	753.83[3]	100[3]	–
1891.9[4]	928.5[4]	100	1899[5]	971[5]	963.36	1891.9[4]	$0^+,1,2$	1892.48[5]	929.12[5]	100[10]	21[1]
1906.0[2]	821.6[11]	27[12]	1910[12]	1088[12]	1085.84	1907.4[11]	2^+	1906.13[3]	820.31[7]		29[2]
	942.4[3]	51[12]	1890[10]	948[10]	963.36	1905.8[3]			942.85[6]	8.5[12]	
	1784.5[3]	100	1923[13]	139[13]	121.78	1906.3[3]			1784.27[7]	100[8]	
	1905.9[3]	96[20]	1911[10]	5[10]	0	1905.9[3]			1906.14[7]		
1954.5[7]	913.4[7]	100	1940[12]	1027[12]	1041.12	1954.5[7]	$3^-,4,5^-$	1954.30[5]	913.17[6]	100[5]	2.8[5]
2003.5[6]	**1296.6[6]**	100	2010[20]	713[20]	706.93	2003.5[6]					2.3[5]
2011.1[3]	1644.6[3]	70[10]	2022[10]	377[10]	366.48	2011.1[3]	$2^+,3,4^+$	2011.84[5]	1645.30[10]	100[9]	19[2]
	1889.4[6]	100	2010[10]	121[10]	121.78	2011.2[6]			1889.95[6]	50[9]	
2091.1[2]	1050.1[3]	99[29]	2092[10]	1042[10]	1041.12	2091.2[3]	$1^-,2$	2091.21[4]	1050.10[5]	100[7]	8[1]
	1127.6[3]	100	2095[11]	967[11]	963.36	2091.0[3]			1127.84[5]	82[7]	
2138.0[2]	1096.9[2]	100	2138[11]	1041[11]	1041.12	2138.0[2]	2^+	2138.17[12]	1096.96[12]	100[4]	7[2]
2138.5[8]	2016.7[8]	100	2120[40]	103[40]	121.78	2138.5[8]	$(2^+,3,4^+)$	2137.92[6]	2016.17[7]		2.3[7]

TABLE II. (*Continued.*)

E_x (keV)	E_γ (keV)	I_γ	E_x^t (keV)	$E_x^t - E_\gamma$ (keV)	E_f^{ND} (keV)	$E_\gamma + E_f^{ND}$ (keV)	$J^{\pi,ND}$	E_x^{ND} (keV)	E_γ^{ND} (keV)	I_γ^{ND}	$\sigma_{(34°-58°)}$ (% of 2_1^+)
2214.9[8]	**2093.1**[8]	100	2202[26]	109[26]	121.78	2214.9[8]					6[1]
2246.1[2]	**1160.3**[3]	100	2249[6]	1089[6]	1085.84	2246.1[3]					24[2]
	1163.3[4]	77[24]	2245[8]	1082[8]	1082.84	2246.1[4]					
	2245.8[8]	41[12]	2234[24]	−15[24]	0	2245.8[8]					
2247.0[2]	**1283.9**[4]	100	2249[8]	965[8]	963.36	2247.3[4]					14[1]
	2125.1[3]	95[28]	2262[18]	137[18]	121.78	2246.9[3]					
2285.2[3]	1321.8[3]	100	2296[30]	974[30]	963.36	2285.2[3]	0,1,2	2284.96[20]	1321.6[2]		6.3[8]
2320.5[2]	516.9[3]	100	2323[9]	1806[9]	1803.94	2320.8[3]	4^+,5	2320.35[23]	516.3[4]	100[10]	47[3]
	1613.2[4]	9[3]	2288[19]	675[19]	706.93	2320.1[4]			1613.4[6]	13[3]	
	1953.8[3]	29[5]	2324[10]	370[10]	366.48	2320.3[3]			1953.7[4]	30[7]	
2331.1[4]	**1624.2**[4]	100	2348[18]	724[18]	706.93	2331.1[4]					6.4[9]
2365.4[3]	**1998.9**[3]	100	2369[13]	370[13]	366.48	2365.4[3]					8[1]
2462.7[5]	**1499.3**[5]	100	2456[12]	957[12]	963.36	2462.7[5]					3.5[6]
2567.8[7]	2201.3[7]	100	2566[20]	365[20]	366.48	2567.8[7]	4^+,5	2567.06[17]	2200.7[2]	100[17]	3.1[9]
2705.0[8]	**2583.2**[8]	100	2702[11]	119[11]	121.78	2705.0[8]					5[1]
3039.1[8]	**2917.3**[8]	100	3038[18]	121[18]	121.78	3039.1[8]					7[2]
3132.0[5]	**2765.5**[5]	100	3134[12]	369[12]	366.48	3132.0[5]					9[3]

column. In column four the triton peak energy from the present work is listed, which is obtained from fitting the peak corresponding to direct population of the level after gating on the γ ray from the same row of the table. In the fifth column the γ-ray energy is subtracted from the triton peak energy. This can be compared with the corresponding level energy from the database of the National Nuclear Data Center at Brookhaven National Laboratory (NNDC) [16] listed in the sixth column. For a definite assignment to be made, we require that these values lie within one standard deviation of each other. In the seventh column the γ-ray energy obtained in the present work is summed with the NNDC energy from column six to obtain the precise level energy. For levels which decay by multiple observed γ rays, the final level energy was obtained from a weighted average of the values in column seven.

In columns eight to eleven the spin and parity, excitation energy, γ-ray energy, and relative γ-ray branching from the NNDC database are listed for previously known levels to compare with the values obtained in the present work. The NNDC values for γ-ray energies and intensities are only listed for γ rays observed in the present work; the full set of known γ rays for each level can be found in Ref. [16].

Figures 5 and 6 show the primary γ-ray decays observed from levels directly populated in the region of the PLS for ^{150}Sm and ^{152}Sm, respectively. Newly identified levels and newly identified or newly placed γ-ray transitions are shown in red, and the region of the PLS is indicated by the dashed lines. In Figs. 7 and 8, excitation energy is plotted against spin for levels directly populated in the present work. Newly identified levels are shown in red. The horizontal lines indicate possible spin ranges for the levels based on the spins of the levels populated by their γ decay.

In the following sections the levels populated in ^{150}Sm and ^{152}Sm in the present work are discussed. Comments are provided only for levels for which new information was obtained or when required for a full understanding of the results presented in Tables I and II.

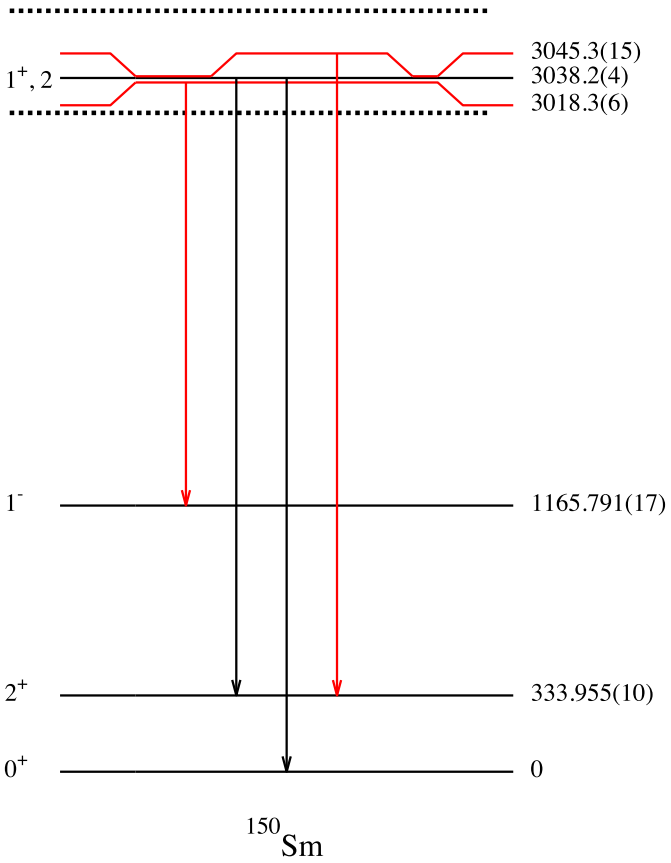

FIG. 5. Partial level scheme of ^{150}Sm showing the primary γ-ray decays from levels directly populated in the ^{152}Sm(p,t) reaction, in the region of the PLS indicated by the dashed lines. Newly identified levels and γ rays are shown in red.

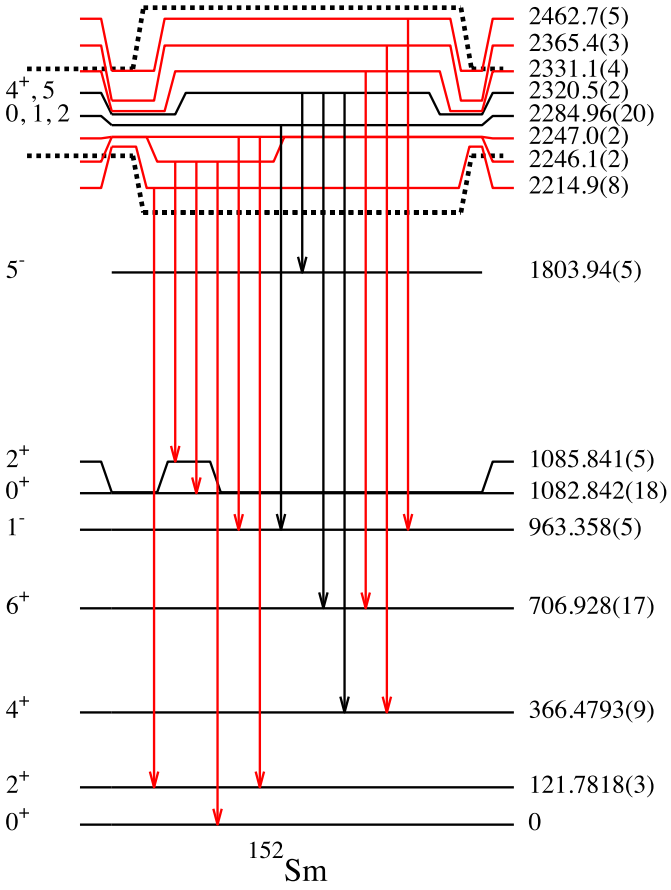

FIG. 6. Same as Fig. 5 but for ^{152}Sm from the ^{154}Sm(p,t) reaction.

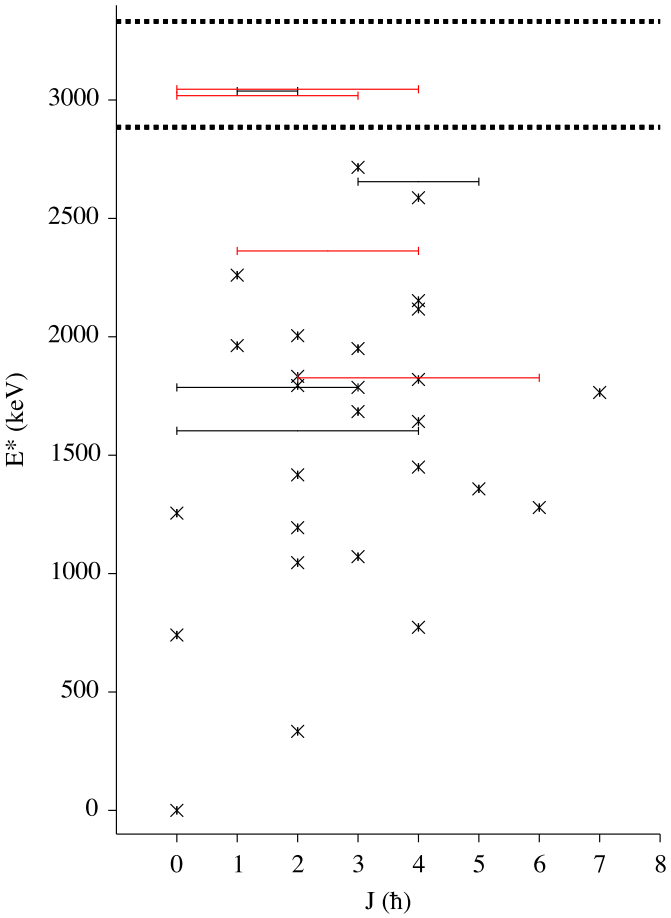

FIG. 7. A plot of excitation energy against spin for levels directly populated in ^{150}Sm. States of known spin are indicated by a black cross. Newly observed states are shown in red. States for which the spin is uncertain are plotted as horizontal lines. The range of possible spins for each level was obtained either from the literature, when available, or estimated by using the observed primary γ-ray transitions by assuming that the spin of a level was within two units of angular momentum of the states it was observed to feed. The region of the PLS is indicated by the black dashed lines.

A. Comments on levels and γ-ray transitions observed in ^{150}Sm

1. The level at 1603.1(7) keV

A 1269.1(7) keV γ-ray transition was placed between the 1603.1(7) keV and 2_1^+ levels. The cross section for the population of this level was measured by Debenham to be 0.48% of the cross section for populating the 0_2^+ level, with both measurements at a laboratory angle of 25 degrees. This is consistent with the value of 0.39(14)% obtained in the present work, integrated across the entire angular range of the telescope, and including only the strength decaying via the 1269.1(7) keV γ ray.

2. The level at 1794.2(2) keV

The NNDC database lists a 2^+ state at 1794.30(3) keV with four known γ rays at energies of 151.64(4), 600.43(25), 722.65(18), and 1798(4) keV. In the present work, the 1798(4) keV γ ray was not observed; it should be seen in the spectrum if the relative intensity from the literature is correct, and it is likely that this transition was misassigned. The 151.64(4) transition was also not observed, but would not be expected to be seen in the spectrum due to the low relative intensity. In addition, we assign to this level 628.5(3) and 1459.9(4) keV transitions.

3. The level at 1826.7(3) keV

A 1053.3(3) keV γ ray is newly observed in prompt coincidence with a state populated at 1824(8) keV in the particle data. This transition is assigned between a new level at 1826.7(3) keV and the 4^+ state at 773.374(12) keV. However, there are insufficient statistics to confirm this assignment by using t-γ-γ coincidences. Thus, the assignment of this level remains tentative.

4. The level at 1832.8(2) keV

The NNDC database lists a level at 1833.01 keV with four γ-ray transitions at energies of 667.05(3), 788, 1499.35(10), and 1833.30(15) keV. The 667.05(3) keV γ ray is listed as the strongest transition, which is in disagreement with the current work where it is observed to have 48(8)% of the strength of a 1498.7(2) keV transition. However, the 667.05(3) keV

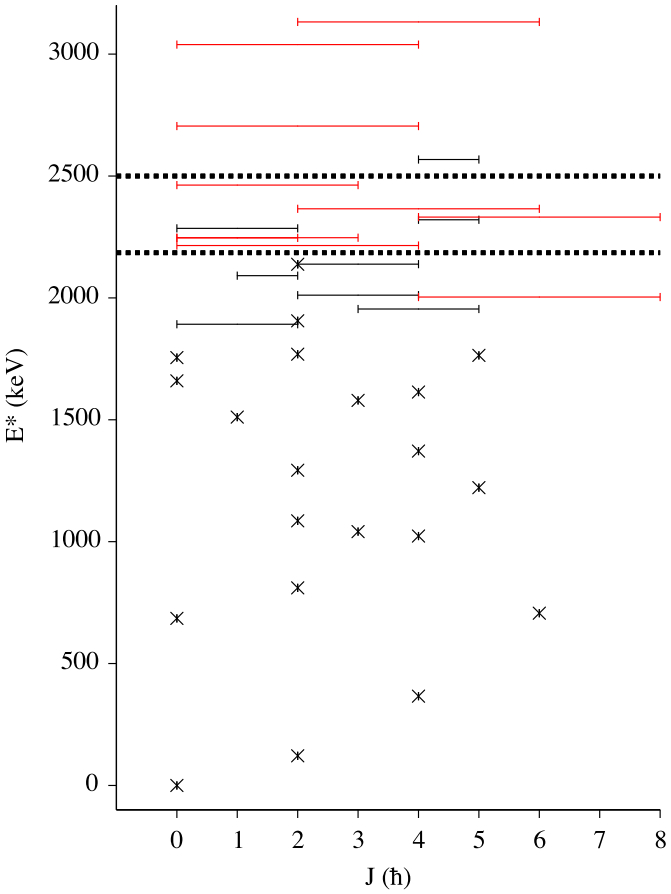

FIG. 8. Same as Fig. 7 but for ^{152}Sm.

transition is multiply placed in the NNDC database and the undivided intensity is given, which explains this discrepancy.

5. The level at 1950.2(2) keV

A 1176.8(2) keV transition is observed from the level at 1950.2(2) keV. The NNDC database makes a tentative assignment of a second γ-ray transition at 308.05(4) keV. However, energy of the state obtained in the present work is not consistent with this second transition. Therefore, we cannot confirm the assignment of the 308 keV γ ray to this level.

6. The level at 2260.1(3) keV

A level at 2260.1(3) keV is identified based upon a 1926.1(3) keV transition to the 2_1^+ level. Barrette *et al.* [21] reported a level at 2259.8 keV with eight decays, including a 1926.04(8) keV transition. Based upon our nonobservation of the other seven γ rays reported in Ref. [21], it seems likely that multiple discrete states occur near 2260 keV, of which only the 2260.1(3) keV level is observed in the present work.

7. The level at 2362.6(2) keV

A new level is observed at an excitation energy of 2362.6(2) keV with the two γ-ray transitions of 1290.9(3) and 2028.9(3) keV. The triton energy spectra gated on these two γ rays are shown in Fig. 9, where the level energy obtained by summing the γ-ray energies with the NNDC energies of the lower-lying levels is indicated by the blue dashed line.

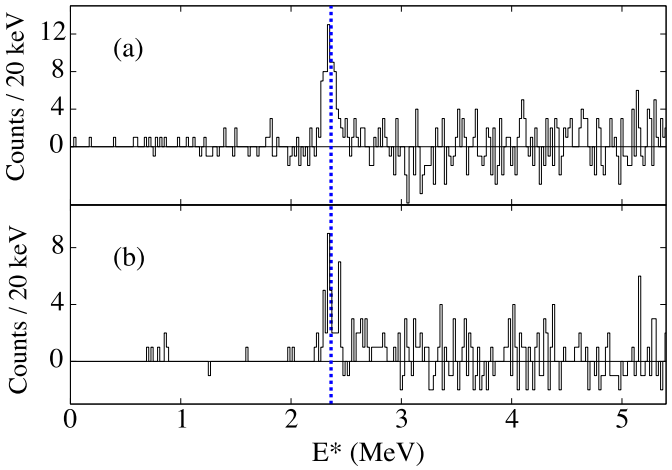

FIG. 9. Triton energy spectra obtained by gating on (a) the 1290.9(3) keV and (b) the 2028.9(3) keV γ rays, showing peaks measured at 2358(8) and 2373(12) keV, respectively. The blue dashed line indicates the excitation energy of 2362.6(2) keV obtained by summing the γ-ray energies with the NNDC energies of the lower-lying levels.

8. The level at 2587.2(4) keV

A new 1813.8(4) keV γ-ray transition is observed between the level at 2587.2(4) keV and the 4_1^+ state, consistent with the previous measurements of the energy of this level [22,23]. This level is likely to be a 4^+ state based on the previous 3^+, 4^+ assignment from Ref. [23] and the natural-parity selection rule in the (p,t) reaction.

9. The level at 2654.9(7) keV

A 2320.9(7) keV transition is observed between the level at 2654.9(7) keV and the 2_1^+ state. It is possible that this is the NNDC level at 2655(7) keV [8,22,24,25]. A spin and parity of $3^{(+)}$, $5^{(+)}$ was previously assigned to this level [25], suggesting that the level is a 3^- state based on the transition to the 2_1^+ state and the natural-parity selection rule.

B. Comments on levels and γ-ray transitions observed in ^{152}Sm

1. The level at 2003.5(6) keV

A level is observed at an excitation energy of 2003.5(6) keV with a 1296.6(6) keV γ-ray transition. This state could correspond to one of three levels from the NNDC database at excitation energies of 2003.66(20), 2004.24(6), and 2004.29(11) keV. The latter two levels have known γ rays at energies of 1297.4(10) and 1297.29(13) keV, respectively.

2. The level at 2214.9(8) keV

A new 2093.1(8) keV γ ray from the level at 2214.9(8) keV is observed. A level has previously been observed at an excitation energy of 2214.92(10) keV [26]. However, this level has been assigned as a 8^+ state which is inconsistent with the transition to the 2_1^+ state observed in the present work.

3. The levels at 2246.1(2) and 2247.0(2) keV

A level at 2246.1(2) keV is observed with three γ-ray transitions at energies of 1160.3(3), 1163.3(4), and 2245.8(8) keV. Additionally, a level at 2247.0(2) keV with two γ-ray transitions of 1283.9(4) and 2125.1(3) keV is observed. Separate level assignments are made since the level energies obtained by using the 1283.9(4) and 2125.1(3) keV transitions are 3.0 and 2.7 standard deviations, respectively, from the level energy evaluated by using the remaining three γ rays. A level at 2247.23 keV was previously observed [27] with transitions to the 0_1^+, 2_1^+, and 1_1^- levels.

4. The level at 2331.1(4) keV

A 1624.2(4) keV γ ray is observed and assigned as a transition to the 6_1^+ state from the level at 2331.1(4) keV. We note that a level at 2332.42 keV has been previously observed [27] in the $(\alpha,2n\gamma)$ reaction with transitions to the 6_1^+ and 8_1^+ levels.

5. The level at 2365.4(3) keV

A 1998.9(3) keV transition between the level at 2365.4(3) keV to the 4_1^+ level is observed. A level at 2365 keV has been previously observed [27] in the Coulomb excitation reaction with transitions to the 4^+ levels at 1371.735(12) and 1612.90(4) keV. These transitions, at 994 and 753 keV, respectively, are not observed in the present work despite the higher γ-ray detection efficiency at those energies. Therefore, it is unlikely that this is the same level.

6. The level at 2462.7(5) keV

A 1499.3(5) keV γ ray from a level at 2462.7(5) keV is observed. A 1498.7(2) keV γ ray is also observed in the ^{152}Sm(p,t) reaction, but the amount of contamination is expected to negligible. A level at 2463.17 keV was previously observed [27] in the $(n,n'\gamma)$ reaction with a transition to the 1_1^- state, which is consistent with the assignment made in the present work.

7. The level at 3132.0(5) keV

A new level is placed at an excitation energy of 3132.0(5) keV with a 2765.5(5) keV γ ray. The triton peak obtained by gating on this γ ray is shown in Fig. 10 and compared with the level energy obtained by summing the γ-ray energy with the NNDC energy of the lower-lying level.

IV. PARTIAL CROSS SECTIONS

Relative partial cross sections for the direct population of states in ^{150,152}Sm via the (p,t) reaction were obtained by gating on the γ rays listed in Tables I and II and measuring the area of the triton peak corresponding to the direct population of a level. We accounted for the γ-ray detection efficiency and, when possible, the internal conversion coefficient for the γ-ray transition. The missing strength due to unobserved γ rays and the finite angular coverage of the Si telescope were not corrected for and therefore these values should be considered as partial cross sections, averaged over the angular range of the telescope of 34 to 58 degrees. The values are given as a percentage of the cross section for direct population of the 2_1^+ level. The relative partial cross sections are listed in Tables I and II and plotted in Figs. 11 and 12 where they are compared with the triton projections of the t-γ coincidence matrices for the ^{152}Sm(p,t) and ^{154}Sm(p,t) reactions, respectively. Overall the correspondence between the two is very good.

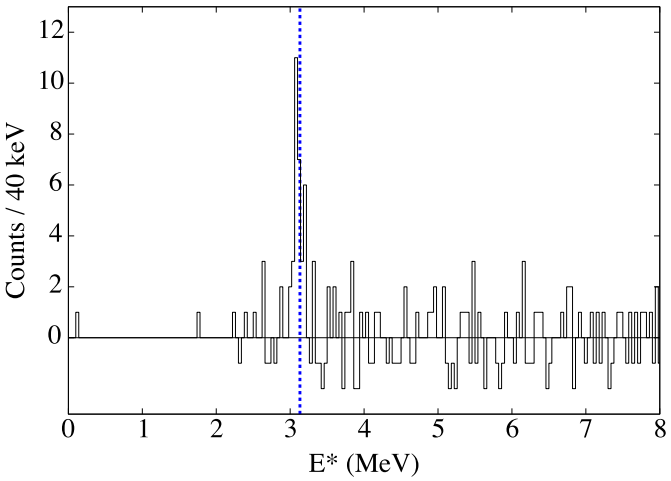

FIG. 10. Triton energy spectrum obtained by gating on the 2765.5(5) keV γ ray. The dashed blue line indicates the level energy obtained by summing the γ-ray energy with the NNDC energy of the lower-lying level that is fed.

Cross sections for populating excited states in ^{150,152}Sm via the (p,t) reaction have previously been measured in Refs. [9–12]. In Table III the relative cross sections obtained in the present work for the ^{152}Sm(p,t) reaction are compared with those obtained by Debenham *et al.* [11] and McLatchie *et al.* [10]. Since the cross sections obtained in the present work are angle averaged between 34 to 58 degrees whereas the values quoted by Debenham are the maximum differential cross sections at the listed angle, this table is provided as

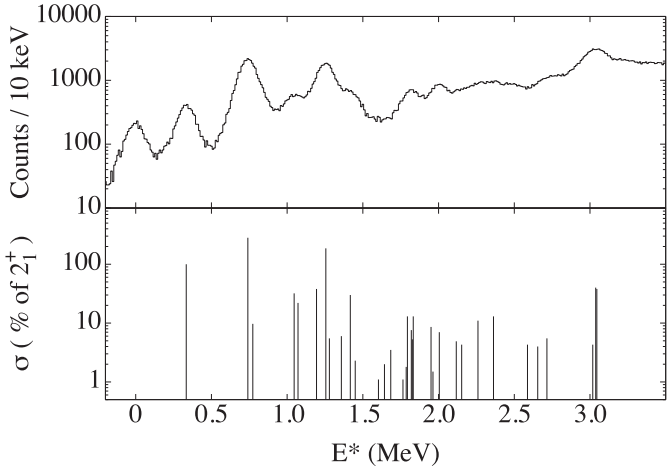

FIG. 11. (top) The triton energy projection from the ^{152}Sm(p,tγ) coincidence matrix. (bottom) The relative partial cross sections from Table I are plotted.

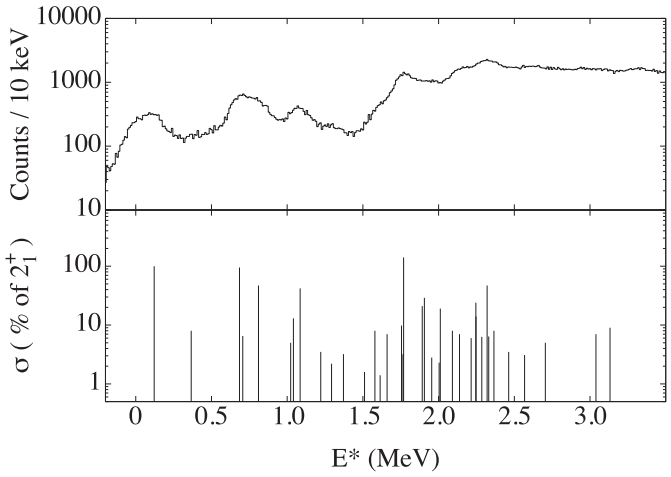

FIG. 12. Same as Fig. 11 but for the ^{154}Sm(p,t) reaction.

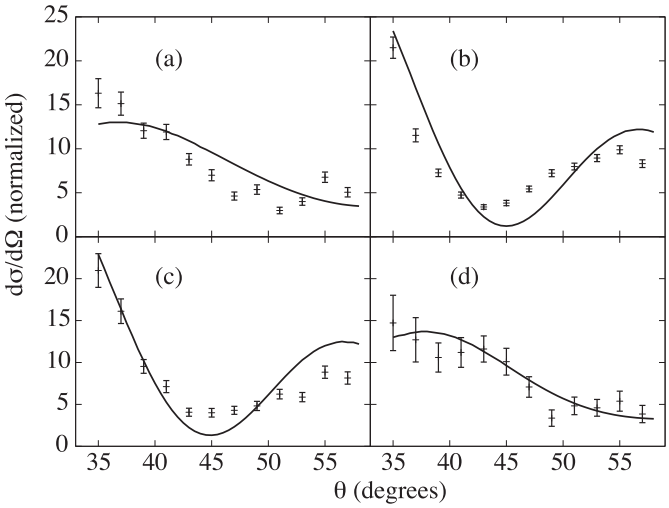

FIG. 13. Experimental angular distributions (black points with error bars) obtained by gating on primary γ rays from the levels populated in the ^{152}Sm(p,t) reaction at (a) 334 keV, $J = 2$ (b) 740 keV, $J = 0$ (c) 1256 keV, $J = 0$, and (d) 1417 keV, $J = 2$ are compared with DWBA calculations for $L = 0$ and 2 transfer (solid lines).

a general comparison only. It should be reemphasized that the values quoted in the present work are lower limits of the relative cross section if there are unobserved γ-ray decay branches. An incident proton energy of 19 MeV was used by Debenham. McLatchie quotes the differential cross section at 22.5° and used an incident proton energy of 20.6 MeV.

Overall, the agreement between the three data sets is good. It can be seen that the excited 0^+ states at 740.6(2) and 1255.4(1) keV have particularly large cross sections in all three sets of measurements. This has been interpreted in terms of shape coexistence and the rapid onset of deformation that occurs in this region [7,28].

TABLE III. The relative partial cross sections for levels in ^{150}Sm obtained in the present work are compared with the cross sections obtained by Debenham [11] and McLatchie [10]. The value reported by Debenham is the maximum differential cross section at the angle listed in the following column. All values are quoted relative to the 2_1^+ level at 333.7(2) keV, which has been scaled to 100. Debenham reports a relative error of 6.9%.

E_x (keV)	J$^\pi$	σ(34°–58°) Present work	$\sigma(\theta)_{max}$ Ref. [11]	θ (degrees)	σ(22.5°) Ref. [10]
333.7(2)	2^+	100(2)	100	10	100
740.6(2)	0^+	282(6)	260	25	340
773.3(3)	4^+	9.7(8)	9.9	10	<20
1046.3(2)	2^+	32(2)	42	10	<20
1071.7(2)	3^-	22(2)	5.6	35	40
1193.9(2)	2^+	38(2)	46	10	80
1255.4(1)	0^+	186(4)	170	25	180
1357.9(4)	5^-	6(1)	1.9	20	<20
1417.2(2)	2^+	30(2)	27	10	30
1449.7(4)	4^+	2.3(6)	3.7	12.5	<20
1603.1(7)		1.1(4)	1.2	25	
1642.6(7)	4^+	2.0(5)	1.2	10	
1794.2(2)	2^+	13(1)	17	10	
1832.8(2)	$(2)^+$	7.6(9)	6.8	20	<20
1950.2(2)	3^-	8.6(9)	3.7	35	<20

V. ANGULAR DISTRIBUTIONS

A. Discrete states

By measuring the angular distribution of the outgoing tritons, the orbital angular-momentum transfer can be determined by comparison to distributions obtained from DWBA calculations. For example, in Fig. 13 the experimental angular distributions from the population of the 334 (2^+), 740 (0^+), 1256 (0^+), and 1417 (2^+) keV levels are compared with DWBA calculations produced using the DWUCK4 code [29] for $L = 0$ and 2 transfer, respectively. The optical model potential used in the present work is defined in Ref. [30]. The proton potential from Ref. [30] was used and the triton and neutron parameters were obtained from Ref. [31]. These parameters are listed in Table IV. The experimental angular distributions were produced by gating on the primary γ-ray transitions from those levels, and measuring the angular distribution of the outgoing tritons in the Si telescope. For levels with multiple observed γ rays, the angular distributions obtained from each γ-ray gate were summed. It can be seen from Fig. 13 that the theoretical curves calculated assuming the NNDC J assignments are in good agreement with the experimental data.

The level at 2320 keV was previously assigned $J = 4^+$,5 in the NNDC database based on its γ-ray decay scheme. The angular distribution for this level is plotted in Fig. 14 where it is compared with the DWBA calculations for $L = 4$ and $L = 5$ transfer. The reduced χ^2 for the $L = 4$ and $L = 5$ curves are 2.1 and 2.2, respectively, therefore a definitive assignment cannot be made.

B. The peak-like structures

In Fig. 15(a), the angular distribution of the PLS observed in ^{150}Sm, centered at ~3 MeV, is compared with the angular distribution for the background under the PLS and with the

TABLE IV. Optical model parameters used in the DWBA calculations. The optical model potential used in the present work is defined in Ref. [30]. The proton parameters are from Ref. [30]. The triton and neutron parameters were obtained from Ref. [31].

	V_r (MeV)	W' (MeV)	W_0 (MeV)	V_{so} (MeV)	R_r (fm)	R_{is} (fm)	R_{iv} (fm)	R_{so} (fm)	a_r (fm)	a_{is} (fm)	a_{iv} (fm)	a_{so} (fm)	R_c (fm)	nlc[a]
p	57.5	29.6	3	5.65	1.200	1.150	1.259	1.010	0.670	0.779	0.76	0.75	1.25	0.85
t	160.03		17.83		1.200		1.400		0.720		0.84		1.30	0.25
n				$\lambda = 25$	1.17				0.75					

[a]Nonlocality parameter.

continuum region at higher excitation energy between 3.3 and 4 MeV. The error bars represent the statistical uncertainty only. The angular distribution for the PLS was obtained by measuring the strength built upon a smooth continuum background, illustrated in Fig. 16, for each ring-sector pixel of the Si telescope. The angular distribution for the background under the PLS was obtained from the area under the blue-shaded region, for each pixel. In Fig. 15(b) the angular distributions for the PLS and background in ^{152}Sm are similarly compared with the nearby continuum region between 2.5 and 3.0 MeV.

It can be seen in Figs. 15(a) and 15(b) that the angular distributions of the PLS are significantly different from the distributions obtained from the nearby continuum region, and that the angular distributions obtained for the background under the PLS are very similar to the distributions obtained for the continuum region. Figure 15(c) compares the angular distributions of the PLS observed in ^{150}Sm and ^{152}Sm. Despite the fact that the two PLS in the two nuclei are 700 keV apart in excitation energy, the two distributions are extremely similar. This suggests that the distributions of orbital angular-momentum transfers are similar in both reactions when populating the PLS. In Fig. 15(d) the angular distributions for the PLS are compared with the DWBA calculations which are most similar to the experimental data. The experimental distributions are most similar to the calculations for $L = 2$, 3, and 4 transfer, which are plotted as the blue, black, and red lines, respectively, calculated for the ^{152}Sm(p,t) reaction.

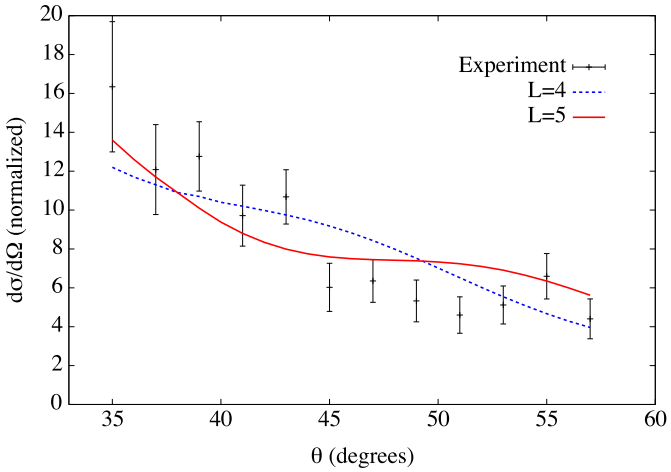

FIG. 14. The experimental angular distribution for the level at 2320.5(2) keV is compared with the DWBA calculations for $L = 4$ (dashed blue line) and $L = 5$ (solid red line) transfer.

VI. DISCUSSION AND SUMMARY OF RESULTS

Perhaps the most striking feature observed in the (p,t) spectra, Fig. 1, is the large PLS observed in all five Sm and Gd nuclei between 2–3 MeV excitation energy. There, a rapid increase in the triton intensity occurs and the smooth continuum "background" begins. Figure 2 shows that the energy of the PLS decreases with increasing neutron number, and that the structure is located at approximately the same excitation energy in Sm and Gd nuclei with the same neutron numbers. One hypothesis is that the structure is partially composed of states formed by the coupling of a neutron hole near the Fermi surface to a deep-lying neutron hole. Then, the energy of the structure is expected to decrease with increasing deformation, i.e., as one moves away from the $N = 82$ spherical shell gap. This deep-hole, valence-hole hypothesis has previously been suggested as an explanation for broad structures observed between 7–9 MeV in the ^{112,116,118,120,122,124}Sn(p,t) reactions [32]. Although it was initially suggested that these structures were formed by creating two deep-lying holes below the shell closure [33], it was found that the energy systematics were better described by the coupling of a valence hole to a deep hole [34]. It has also been shown in the review by Crawley [35] that bumps observed in two neutron-transfer reactions in the Cd isotopes are likely to correspond to a valence-hole deep-hole configuration. In the (p,t) study by Nakagawa *et al.* [36], bumps at lower and higher excitation energy, corresponding to valence-deep and deep-deep hole states, respectively, were observed across a wide range of nuclei from ^{66}Zn to ^{230}Th. This includes one isotope of samarium, ^{148}Sm, where a bump corresponding to the deep-deep configuration was observed at an excitation energy of approximately 6 MeV. The bump corresponding to the valence-deep configuration would be expected to lie at lower excitation energy. However, it must be noted that the FWHM of these structures in the $N = 82$ region is approximately 5 MeV, much larger than the narrow structures observed in the present work. A study of two-neutron hole strength in ^{142,146,148,150,152}Sm was performed by Struble *et al.* [13] where the broad structure observed by Nakagawa at 6 MeV in ^{148}Sm was also observed. The PLS observed in the present work can be seen in Fig. 4 of that paper labeled as peak e. It was suggested by Struble that these much narrower structures are associated with two-hole strength in strongly up-sloping orbitals from below the $N = 82$ shell closure.

In ^{152}Sm between 2.2 and 2.5 MeV, i.e., in the region of the PLS, a total of eight levels are found which are directly populated in the (p,t) reaction including six newly identified

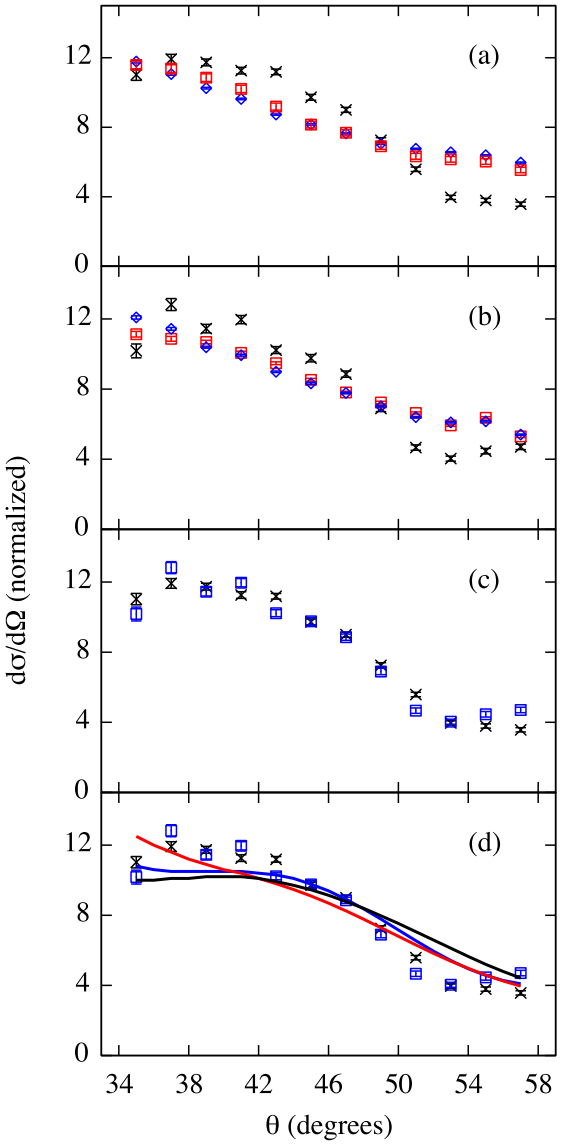

FIG. 15. (a) The angular distribution of the PLS in ^{150}Sm (black points) is compared with the angular distribution for the background under the PLS (red points) and the distribution obtained for the nearby continuum region between 3.3 and 4.0 MeV (blue points). (b) The angular distribution of the PLS in ^{152}Sm (black points) is compared with the angular distribution for the background under the PLS (red points) and the distribution obtained for the nearby continuum region between 2.5 and 3.0 MeV (blue points). (c) The angular distributions of the PLS observed in ^{150}Sm (black points) and ^{152}Sm (blue points) are compared. (d) Same as panel (c), except that the DWBA calculations for $L = 2$ (blue line), $L = 3$ (black line), and $L = 4$ (red line) transfer, calculated for the ^{152}Sm(p,t) reaction, are also plotted.

levels. The majority of likely spin values for these also range from 0 to 5$\hbar$. In ^{150}Sm the PLS is observed at a higher excitation energy, extending from 2.9 to 3.3 MeV. Only three discrete levels, including two newly identified ones, are observed in this energy region; see Fig. 5. This is due in part to the lower detection efficiency for higher-energy γ rays. Possible spin values for these levels lie in the 0–4$\hbar$ range; see Fig. 7.

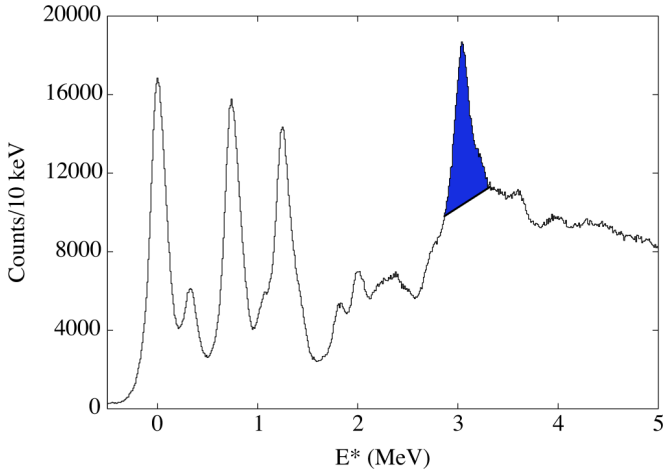

FIG. 16. The triton singles spectrum from the ^{152}Sm(p,t) reaction. The blue-shaded area corresponds to the counts considered to belong to the PLS when measuring the angular distributions shown in Fig. 15(c).

In ^{150}Sm, the relative cross section, within the angular range of the telescope, for the population of the PLS, and measured in the triton singles spectrum, is 213(20)% of the cross section for the direct population of the 2_1^+ level. Of this strength, 39(4)% can be accounted for by the discrete states observed in the present work. In ^{152}Sm, the strength of the PLS was observed to be be 117(19)% of the 2_1^+ level. Of this strength, 93(15)%, could be accounted for by the discrete states observed in the present work. This measurement is consistent with the spectrum seen in the top panel of Fig. 1 from Ref. [12]. There, it can be seen that the region of the PLS around 2.3 MeV in ^{152}Sm appears to be dominated by a relatively small number of states with large cross sections; in particular the level measured by Saha at an excitation energy of 2268 keV. This corresponds to the levels measured at 2246.1(2) and 2247.0(2) keV in the present work, because the excitation energies reported by Saha appear to be systematically too high.

The angular distributions of the PLS, shown in Fig. 15, differ significantly from that of the nearby continuum region and have a shape more characteristic of the single L-transfer curves. This suggests that the L-transfer distribution when populating the PLS is significantly different than when populating the adjacent continuum region, which supports the conclusion that the structures are dominated by a relatively low number of states of similar spins. The fact that the angular distributions of the PLS populated in the two reactions are very similar, as shown in Fig. 15(c), suggests that the L-transfer distributions are also similar.

In summary, numerous new levels and γ-ray transitions were identified in ^{150,152}Sm utilizing the t-γ coincidence technique, including in the region of the PLS observed between 2.3 and 3.0 MeV. These structures appear to be dominated by a relatively small number of discrete states, particularly in ^{152}Sm. The angular distributions of the outgoing tritons populating the PLS in the ^{152,154}Sm(p,t) reactions are very similar and significantly different from the angular distributions obtained by gating on the adjacent higher-excitation-energy continuum region.

ACKNOWLEDGMENTS

The authors are grateful to Professor J. L. Wood for information on levels and γ-ray transitions in ^{152}Sm and for helpful discussion of the data. This material is based on work supported by the U.S. Department of Energy, Office of Science, Office of Nuclear Physics under Grants No. DE-SC0014277, No. DE-FG02-05ER41379, and No. DE-FG02-93ER40773, by the U.S. Department of Energy, National Nuclear Security Administration under Grants No. DE-NA0002914, No. DE-NA0001801, and No. DE-FG52-09NA29467, by the National Science Foundation under contract PHY-130581, and by the U.S. Department of Energy NNSA Office of Defense Nuclear Nonproliferation Research & Development under Contract No. DE-AC52-07NA27344 (Lawrence Livermore National Laboratory).

[1] D. A. Meyer, V. Wood, R. F. Casten, C. R. Fitzpatrick, G. Graw, D. Bucurescu, J. Jolie, P. von Brentano, R. Hertenberger, H.-F. Wirth, N. Braun, T. Faestermann, S. Heinze, J. L. Jerke, R. Krücken, M. Mahgoub, O. Möller, D. Mücher, and C. Scholl, Phys. Rev. C **74**, 044309 (2006).
[2] N. V. Zamfir, J.-y. Zhang, and R. F. Casten, Phys. Rev. C **66**, 057303 (2002).
[3] D. Tonev, A. Dewald, T. Klug, P. Petkov, J. Jolie, A. Fitzler, O. Möller, S. Heinze, P. von Brentano, and R. F. Casten, Phys. Rev. C **69**, 034334 (2004).
[4] R. F. Casten, M. Wilhelm, E. Radermacher, N. V. Zamfir, and P. von Brentano, Phys. Rev. C **57**, R1553 (1998).
[5] F. Iachello, N. V. Zamfir, and R. F. Casten, Phys. Rev. Lett. **81**, 1191 (1998).
[6] P. E. Garrett, W. D. Kulp, J. L. Wood, D. Bandyopadhyay, S. Choudry, D. Dashdorj, S. R. Lesher, M. T. McEllistrem, M. Mynk, J. N. Orce, and S. W. Yates, Phys. Rev. Lett. **103**, 062501 (2009).
[7] J. R. Maxwell, G. M. Reynolds, and N. M. Hintz, Phys. Rev. **151**, 1000 (1966).
[8] J. H. Bjerregaard, O. Hansen, O. Nathan, and S. Hinds, Nucl. Phys. **86**, 145 (1966).
[9] W. Oelert, G. Lindström, and V. Riech, Nucl. Phys. A **233**, 237 (1974).
[10] W. McLatchie, W. Darcey, and J. E. Kitching, Nucl. Phys. A **159**, 615 (1970).
[11] P. Debenham and N. M. Hintz, Nucl. Phys. A **195**, 385 (1972).
[12] A. Saha, O. Scholten, D. C. J. M. Hageman, and H. Fortune, Phys. Lett. B **85**, 215 (1979).
[13] G. L. Struble, L. G. Mann, R. G. Lanier, W. M. Buckley, J. Kern, G. Crawley, S. Gales, D. Mueller, and F. Girshick, Phys. Rev. C **23**, 2447 (1981).
[14] H. J. Riezebos, R. De Leo, P. B. Goldhoorn, M. N. Harakeh, and L. W. Put, Phys. Lett. B **118**, 287 (1982).
[15] S. R. Lesher *et al.*, Nucl. Instrum. Methods Phys. Res., Sect. A **621**, 286 (2010).
[16] Evaluated Nuclear Structure Data File (ENSDF); National Nuclear Data Center (NNDC), Brookhaven National Laboratory (2014).
[17] Energy Loss and Straggling Tool (ELAST), adapted from the computer program ENELOSS, written by H. Ernst (1981) with stopping power routines by K. Lesko (1984).
[18] T. J. Ross, C. W. Beausang, R. O. Hughes, J. M. Allmond, C. T. Angell, M. S. Basunia, D. L. Bleuel, J. T. Burke, R. J. Casperson, J. E. Escher, P. Fallon, R. Hatarik, J. Munson, S. Paschalis, M. Petri, L. Phair, J. J. Ressler, N. D. Scielzo, and I. J. Thompson, Phys. Rev. C **85**, 051304(R) (2012).
[19] J. M. Allmond (unpublished).
[20] J. M. Allmond, C. W. Beausang, J. O. Rasmussen, T. J. Ross, M. S. Basunia, L. A. Bernstein, D. L. Bleuel, W. Brooks, N. Brown, J. T. Burke, B. K. Darakchieva, K. R. Dudziak, K. E. Evans, P. Fallon, H. B. Jeppesen, J. D. LeBlanc, S. R. Lesher, M. A. McMahan, D. A. Meyer, L. Phair, N. D. Scielzo, S. R. Stroberg, and M. Wiedeking, Phys. Rev. C **81**, 064316 (2010).
[21] J. Barrette, M. Barrette, S. Monaro, S. Santhanam, and S. Markiza, Can. J. Phys. **48**, 1161 (1970).
[22] L. V. Groshev, A. M. Demidov, V. A. Ivanov, V. N. Lutsenko, and V. I. Pelekhov, Nucl. Phys. **43**, 669 (1963).
[23] F. Bečvář, R. E. Chrien, and O. A. Wasson, Nucl. Phys. A **236**, 173 (1974).
[24] R. A. Kenefick and R. K. Sheline, Phys. Rev. **133**, B25 (1964).
[25] E. R. Reddingius and H. Postma, Nucl. Phys. A **137**, 389 (1969).
[26] J. Konijn *et al.*, Nucl. Phys. A **373**, 397 (1982).
[27] J. L Wood (private communication).
[28] T. Takemasa, M. Sakagami, and M. Sano, Phys. Lett. B **37**, 473 (1971).
[29] P. D. Kunz, DWUCK4 (University of Colorado, 1974).
[30] N. Blasi *et al.*, Nucl. Phys. A **624**, 433 (1997).
[31] H.-F. Wirth, G. Graw, S. Christen, D. Cutoiu, Y. Eisermann, C. Günther, R. Hertenberger, J. Jolie, A. I. Levon, O. Möller, G. Thiamova, P. Thirolf, D. Tonev, and N. V. Zamfir, Phys. Rev. C **69**, 044310 (2004).
[32] G. M. Crawley, W. Benenson, G. Bertsch, S. Gales, D. Weber, and B. Zwieglinski, Phys. Rev. C **23**, 589 (1981).
[33] G. M. Crawley, W. Benenson, D. Weber, and B. Zwieglinski, Phys. Rev. Lett. **39**, 1451 (1977).
[34] M. Nomura, Prog. Theor. Phys. **59**, 1771 (1978).
[35] G. M. Crawley, *Proc. 1980 RCNP International Symposium on Highly Excited States in Nuclear Reactions*, edited by H. Ikegami and M. Muraoka (Research Center for Nuclear Physics, Osaka University, Suita Osaka, Japan, 1980), p. 590.
[36] T. Nakagawa *et al.*, Nucl. Phys. A **376**, 513 (1982).

Appendix C

List of Publications

Papers

P. Humby, A. Simon, C. W. Beausang, J. M. Allmond, J. T. Burke, R. J. Casperson, R. Chyzh, M. Dag, K. Gell, R. O. Hughes, J. Koglin, E. McCleskey, M. McCleskey, S. Ota, T. J. Ross, A. Saastamoinen, T. Tarlow and G. Vyas. *Investigation of discrete states and quasidiscrete structures observed in ^{150}Sm and ^{152}Sm using the (p,tγ) reaction.* PHYSICAL REVIEW C **94**, 064314 (2016).

P. Humby, A. Simon, C. W. Beausang, T. J. Ross, R. O. Hughes, J. T. Burke, R. J. Casperson, J. Koglin, S. Ota, J. M. Allmond, M. McCleskey, E. McCleskey, A. Saastamoinen, R. Chyzh, M. Dag, K. Gell, T. Tarlow and G. Vyas. *Improved measurement of the half-life of the $J^{\pi} = 8^{-}$ nuclear isomer $^{152_{m2}}Eu$.* PHYSICAL REVIEW C **91**, 024322 (2015).

D. T. Doherty, J. M. Allmond, R. V. F. Janssens, W. Korten, S. Zhu, M. Zielińska, D. C. Radford, A. D. Ayangeakaa, B. Bucher, J. C. Batchelder, C. W. Beau-

sang, C. Campbell, M. P. Carpenter, D. Cline, H. L. Crawford, H. M. David, J. P. Delaroche, C. Dickerson, P. Fallon, A. Galindo-Uribarri, F. G. Kondev, J. L. Harker, A. B. Hayes, M. Hendricks, **P. Humby**, M. Girod, C. J. Gross, M. Klintefjord, K. Kolos, G. J. Lane, T. Lauritsen, J. Libert, A. O. Macchiavelli, P. J. Napiorkowski, E. Padilla-Rodal, R. C. Pardo, W. Reviol, D. G. Sarantites, G. Savard, D. Seweryniak, J. Srebrny, R. Varner, R. Vondrasek, A. Wiens, E. Wilson, J. L. Wood and C. Y. Wu. *Triaxiality near the ^{110}Ru ground state from Coulomb excitation.* Accepted, PHYSICS LETTERS B (2017).

B. Löher, D. Savran, T. Aumann, J. Beller, M. Bhike, N. Cooper, V. Derya, M. Duchêne, J. Endres, A. Hennig, **P. Humby**, J. Isaak, J. H. Kelley, M. Knörzer, N. Pietralla, V. Yu Ponomarev, C. Romig, M. Scheck, H. Scheit, J. Silva, A. P. Tonchev, W. Tornow, F. Wamers, H. Weller, V. Werner and A. Zilges. *The decay pattern of the Pygmy Dipole Resonance of ^{140}Ce.* PHYSICS LETTERS B **756**, 72 (2016).

A. Simon, M. Guttormsen, A. C. Larsen, C. W. Beausang, **P. Humby**, J. T. Burke, R. J. Casperson, R. O. Hughes, T. J. Ross, J. M. Allmond, R. Chyzh, M. Dag, J. Koglin, E. McCleskey, M. McCleskey, S. Ota and A. Saastamoinen. *First observation of low-energy γ-ray enhancement in the rare-earth region.* PHYSICAL REVIEW C **93**, 034303 (2016).

J. E. Escher, A. P. Tonchev, J. T. Burke, P. Bedrossian, R. J. Casperson, N. Cooper, R. O. Hughes, **P. Humby**, R. S. Ilieva, S. Ota, N. Pietralla, N. D. Scielzo and V. Werner. *Compound-nuclear reactions with unstable nuclei: Constraining theory through innovative experimental approaches.* EPJ WEB OF CONFER-

ENCES **122**, 12001 (2016).

V. Werner, N. Cooper, P. M. Goddard, **P. Humby**, R. S. Ilieva, G. Rusev, J. Beller, C. Bernards, B. P. Crider, J. Isaak, J. H. Kelley, E. Kwan, B. Löher, E. E. Peters, N. Pietralla, C. Romig, D. Savran, M. Scheck, A. P. Tonchev, W. Tornow, S. W. Yates and M. Zweidinger. *Dipole strength distributions from HIGS Experiments.* EPJ WEB OF CONFERENCES **93**, 01031 (2015).

V. Werner, N. Cooper, P. M. Goddard, **P. Humby** and R. S. Ilieva. *Impact of mesoscopy on nuclear structure phenomena.* ROMANIAN JOURNAL OF PHYSICS **60**, 819 (2015).

V. Werner, N. Cooper, P. M. Goddard, R. S. Ilieva, **P. Humby** and N. Pietralla. *Low-Lying "Pygmy" Dipole Resonances and Strength Functions* in Nuclear Physics and Gamma-Ray Sources for Nuclear Security and Nonproliferation (2014), edited by T. Hayawaka, M. Senzaki, P. Bolton, R. Hajima, M. Seya and M. Fujiwara. (World Scientific) p. 117 .

R. O. Hughes, C. W. Beausang, T. J. Ross, J. T. Burke, R. J. Casperson, N. Cooper, J. E. Escher, K. Gell, E. Good, **P. Humby**, M. McCleskey, A. Saastimoinen, T. D. Tarlow and I. J. Thompson. *^{236}Pu(n,f), ^{237}Pu(n,f), and ^{238}Pu(n,f) cross sections deduced from (p,t), (p,d) and (p,p') surrogate reactions.* PHYSICAL REVIEW C **90**, 014304 (2014).

Invited Talks

P. Humby. *Low Energy Nuclear Science at the University of Richmond.* SSAP Symposium, February 2016, Bethesda, MD.

Bibliography

[1] H. Becquerel, C. R. Acad. Sci. **122**, 420 (1896).

[2] E. Rutherford, Philos. Mag. **21**, 669 (1911).

[3] G. Scharff-Goldhaber and J. Weneser, Phys. Rev. **98**, 212 (1955).

[4] D. A. Meyer *et al.*, Phys. Rev. C **74**, 044309 (2006).

[5] N. V. Zamfir, Jing-ye Zhang, and R. F. Casten, Phys. Rev. C **66**, 057303 (2002).

[6] D. Tonev *et al.*, Phys. Rev. C **69**, 034334 (2004).

[7] R. F. Casten *et al.*, Phys. Rev. C **57**, R1553 (1998).

[8] F. Iachello, N. V. Zamfir, and R. F. Casten, Phys. Rev. Lett. **81**, 1191 (1998).

[9] P. E. Garrett *et al.*, Phys. Rev. Lett. **103**, 062501 (2009).

[10] J. R. Maxwell, G. M. Reynolds, and N. M. Hintz, Phys. Rev. **151**, 1000 (1966).

[11] J. H. Bjerregaard, O. Hansen, O. Nathan, and S. Hinds, Nucl. Phys. **86**, 145 (1966).

[12] T. J. Ross *et al.*, Phys. Rev. C. **88**, 031301(R) (2013).

[13] R. Wenz, A. Timmermann, and E. Matthias, Z. Phys. A. **303**, 87 (1981).

[14] T. Sumikama *et al.*, Phys. Rev. Lett. **106**, 202501 (2011).

[15] H. Hua *et al.*, Phys. Rev. C. **69**, 014317 (2004).

[16] C. Piller *et al.*, Phys. Rev. C. **42**, 182 (1990).

[17] W. Oelert, G. Lindström, and V. Riech, Nucl. Phys. A **233**, 237 (1974).

[18] W. McLatchie, W. Darcey, and J. E. Kitching, Nucl. Phys. A **159**, 615 (1970).

[19] P. Debenham and N. M. Hintz, Nucl. Phys. A **195**, 385 (1972).

[20] A. Saha, O. Scholten, D. C. J. M. Hageman, and H. T. Fortune, Phys. Lett. **85B**, 215 (1979).

[21] G. L. Struble *et al.*, Phys. Rev. C **23**, 2447 (1981).

[22] E. R. Flynn *et al.*, Phys. Rev. C. **28**, 97 (1983).

[23] A. M. Oros *et al.*, Nucl. Phys. A. **613**, 209 (1997).

[24] R. D. Gadsby, D. G. Burke, and J. C. Waddington, Can. J. Phys. **51**, 203 (1973).

[25] G. Pálla, H. V. von Geramb, and G. Lindström, J. Phys. G: Nucl. Phys. **8**, 1007 (1982).

[26] T. Takemasa, M. Sakagami, and M. Sano, Phys. Lett. B. **37**, 473 (1971).

[27] H. J. Riezebos *et al.*, Phys. Lett. **118B**, 287 (1982).

[28] T. J. Ross *et al.*, Phys. Rev. C **85**, 051304(R) (2012).

[29] J. M. Allmond - Unpublished data.

[30] G. M. Crawley *et al.*, Phys. Rev. C **23**, 589 (1981).

[31] M. Nomura, Prog. Theory. Phys. **59**, 1771 (1978).

[32] T. Nakagawa *et al.*, Nucl. Phys. A **376**, 513 (1982).

[33] M. Goeppert-Mayer, Phys. Rev. **75**, 1969 (1949).

[34] K. S. Krane, *Introductory Nuclear Physics*, 2 ed. (John Wiley and Sons, 1988).

[35] Data extracted using the NNDC On-Line Data Service from the ENSDF database, file revised as of 2013. S. K. Basu, A. A. Sonzogni, Nuclear Data Sheets 114, 435 (2013).

[36] J. M. Allmond *et al.*, Phys. Rev. C **81**, 064316 (2010).

[37] A. Arima and F. Iachello, Ann. Phys. **99**, 253 (1976).

[38] R. Casten, *Nuclear Structure from a Simple Perspective* (Oxford University Press, 1990).

[39] H. Paetz gen. Schieck, *Nuclear Reactions. Lecture Notes in Physics Vol. 882.* (Springer, 2014).

[40] N. Glendenning, *Direct Nuclear Reactions* (Academic Press, Inc. (Elsevier), 1983).

[41] J. D. Cramer and H. C. Britt, Nucl. Sci. Eng. **41**, 177 (1970).

[42] H. C. Britt and J. B. Wilhelmy, Nucl. Sci. Eng. **72**, 222 (1979).

[43] J. E. Escher *et al.*, Rev. Mod. Phys. **84**, 353 (2012).

[44] N. D. Scielzo *et al.*, Phys. Rev. C. **81**, 034608 (2010).

[45] F. D. Becchetti Jr. and G. W. Greenlees, Phys. Rev. **182**, 1190 (1969).

[46] C. M. Perey and F. G. Perey, At. Data Nucl. Data Tables **17**, 1 (1976).

[47] DWUCK4 - P.D. Kunz, University of Colorado (1974).

[48] N. Blasi *et al.*, Nucl. Phys. A **624**, 433 (1997).

[49] H.-F. Wirth *et al.*, Phys. Rev. C **69**, 044310 (2004).

[50] G. Bassani, N. M. Hintz, and C. D. Kavaloski, Phys. Rev. **136**, B1006 (1964).

[51] G. Knoll, *Radiation Detection and Measurement*, Third ed. (John Wiley & Sons, 2000).

[52] S. R. Lesher *et al.*, Nucl. Instrum. Methods Phys. Res., Sect. A **621**, 286 (2010).

[53] T. J. Ross *et al.*, Phys. Rev. C. **90**, 044323 (2014).

[54] Energy loss and Straggling Tool (ELAST), [Adapted from the computer program ENELOSS, written by H. Ernst (1981) with stopping power routines by K. Lesko (1984)].

[55] P. Humby *et al.*, Phys. Rev. C. **94**, 064314 (2016).

[56] P. Humby *et al.*, Phys. Rev. C. **91**, 024322 (2015).

[57] R. K. Smither, Phys. Rev. **150**, 964 (1966).

[58] J. Barrette, M. Barrette, S. Monaro, S. Santhanam, and S. Markiza, Can. J. Phys. **48**, 1161 (1970).

[59] F. Bečvář, R. E. Chrien, and O. A. Wasson, Nucl. Phys. A **236**, 173 (1974).

[60] L. V. Groshev, A. M. Demidov, V. A. Ivanov, V. N. Lutsenko, and V. I. Pelekhov, Nucl. Phys. **43**, 669 (1963).

[61] R. A. Kenefick and R. K. Sheline, Phys. Rev. **133**, B25 (1964).

[62] E. R. Reddingius and H. Postma, Nucl. Phys. A **137**, 389 (1969).

[63] Jan Konijn *et al.*, Nucl. Phys. A **373**, 397 (1982).

[64] J. L Wood - private communication.

[65] G. M. Crawley, W. Benenson, D. Weber, and B. Zwieglinski, Phys. Rev. Lett. **39**, 1451 (1977).

[66] E. Gerlic *et al.*, Phys. Lett. **117B**, 20 (1982).

[67] S. Y. van der Werf *et al.*, Phys. Rev. Lett. **33**, 712 (1974).

[68] R. A. Broglia and D. R. Bes, Phys. Lett. **69B**, 129 (1977).

[69] S. Galés, Ch. Stoyanov, and A. I. Vdovin, Phys. Rep. **166**, 125 (1988).

[70] S. Gales, Nucl. Phys. A. **354**, 193c (1981).

[71] V. V. Voronov, J. Phys. G: Nucl. Phys. **9**, L273 (1983).

[72] V. G. Soloviev, Prog. Part. Nucl. Phys. **19**, 107 (1987).

[73] T. von Egidy *et al.*, Z. Phys. A **286**, 341 (1978).

[74] H. Beer, F. Käppeler, K. Yokoi, and K. Takahashi, Astrophys. J. **278**, 388 (1984).

[75] H.S. Pruys, E.A. Hermes and H.R. von Gunten., J. Inorg. Nucl. Chem. **37**, 1587 (1975).

[76] A. Abzouzi *et al.*, J. Radioanal. Nucl. Chem. **145**, 361 (1990).

[77] F. Lagoutine and J. Legrand, Int. J. Appl. Radiat. Isot. **33**, 711 (1982).

[78] J.T. Corless, *Isotopic Abundance Studies by Neutron Activation Analysis. Annual Report, April 15, 1964-April 14, 1966* .

[79] G. Gueben and J. Govaerts, Inst. Interuniv. Sci. Nucleaires (Bruxelles), Monographie No.2 (1958).